
Doctoral Dissertations

Student Theses and Dissertations

Fall 2013

Common mode current estimation for cable bundle inside a vehicle

Dazhao Liu

Follow this and additional works at: https://scholarsmine.mst.edu/doctoral_dissertations



Part of the [Electrical and Computer Engineering Commons](#)

Department: **Electrical and Computer Engineering**

Recommended Citation

Liu, Dazhao, "Common mode current estimation for cable bundle inside a vehicle" (2013). *Doctoral Dissertations*. 1823.

https://scholarsmine.mst.edu/doctoral_dissertations/1823

This thesis is brought to you by Scholars' Mine, a service of the Missouri S&T Library and Learning Resources. This work is protected by U. S. Copyright Law. Unauthorized use including reproduction for redistribution requires the permission of the copyright holder. For more information, please contact scholarsmine@mst.edu.

COMMON MODE CURRENT ESTIMATION
FOR CABLE BUNDLE INSIDE A VEHICLE

by

DAZHAO LIU

A DISSERTATION

Presented to the Faculty of the Graduate School of the
MISSOURI UNIVERSITY OF SCIENCE AND TECHNOLOGY

In Partial Fulfillment of the Requirements for the Degree

DOCTOR OF PHILOSOPHY

in

ELECTRICAL ENGINEERING

2013

Approved by:

Dr. Jun Fan, Advisor
Dr. David Pommerenke
Dr. James L. Drewniak
Dr. Daryl Beetner
Dr. Richard Dubroff
Dr. Matthew J. O'keefe

© 2013

Dazhao Liu

All Rights Reserved

ABSTRACT

In the Section 1, it introduces a methodology to simulate the currents and fields during an air discharge ESD into a product by combining a linear description of the behavior of the DUT with a non-linear arc resistance equation. The most commonly used test standard IEC 61000-4-2 requires using contact mode discharges to metallic surfaces and air discharge mode to non-conducting surfaces. This paper proposes a method that combines the linear ESD generator full wave model and the non-linear arc model to simulate currents and fields in air discharge mode.

In Section 2, when simulating surface and thin wire structures, full wave MoM method is accurate, but time consuming. On the other hand, conventional Multiconductor Transmission Line Theory (MTL) provides a very simple model, but can only deal with Transmission Line (TL-) mode current. A proposed Multi-Scattering method by hybrid of MTL and surface MoM can be used to calculate interactions between surface and thin wire structures. After only a few scattering, the wire current value can match the result obtained by full wave MoM method.

In Section 3, a fast method to calculate the admittance matrix of Through Silicon Vias (TSVs) is proposed. The silicon dioxide layers are equivalently modeled using the positive bound charge on the conductor surfaces as well as the equal amount negative bound charge on the dielectric interface between the silicon dioxide and the silicon regions. Unknown densities of both the free and bound surface charge are expanded using the axial harmonics. Galerkin's method is then applied to obtain the capacitance and conductance matrices.

ACKNOWLEDGMENTS

I would like to express my sincere gratitude to Dr. Jun Fan, my advisor, for his teaching, instruction, warm encouragement on my research work, financial support to my study and direction for this thesis during my pursuit of the PhD's degree.

I would like to thank Dr. David Pommerenke, my advisor for my first year in Rolla, for his enlightening to my research motion and teaching me how to walk on water.

I would like to thank Dr. James Drewniak, my mentor during my transition time, the most difficult days when I got rid of my immaturity and irresponsibility, for giving me faith, trust, and encouragement.

I would like to thank Dr. Daryl Beetner, and Dr. Richard DuBroff, for their teaching in my courses, discussions related to my research and helpful suggestions on my thesis.

I would also like to express my thanks to all the other faculty members and students in the UMR/MST EMC lab for their team work and help in my research and coursework. It has been my great pleasure to work with you!

Finally, I would like to thank my family for their love and my wife Qian for her unconditional support during my five years of graduate study.

TABLE OF CONTENTS

| | Page |
|--|------|
| ABSTRACT | iii |
| ACKNOWLEDGMENTS | iv |
| LIST OF ILLUSTRATIONS | vii |
| LIST OF TABLES | xi |
| SECTION | |
| 1. FULL WAVE SIMULATION OF AN ELECTROSTATIC DISCHARGE GENERATOR DISCHARGING IN AIR DISCHARGE MODE | 1 |
| 1.1. INTRODUCTION | 1 |
| 1.2. METHODOLOGY | 2 |
| 1.3. CASE 1: ESD GENERATOR DISCHARGE TO A GROUND PLANE | 5 |
| 1.3.1. Z11 between the Tip of the ESD Generator and the Ground Plane. ... | 5 |
| 1.3.2. SPICE Simulation for the Discharge Current..... | 8 |
| 1.3.3. Re-import of Currents into CST..... | 9 |
| 1.3.4. Validation by Measurement Results..... | 9 |
| 1.4. CASE 2: ESD GENERATOR DISCHARGE INTO A PRODUCT | 11 |
| 1.4.1. Z11 between the Tip of the ESD Generator and the Ground Plane. . | 11 |
| 1.4.2. SPICE Simulation for the Discharge Current..... | 13 |
| 1.4.3. Re-import of Currents into CST..... | 14 |
| 1.4.4. Validation by Measurement Results..... | 15 |
| 1.4.4.1 Measured discharge current. | 16 |
| 1.4.4.2 Measured magnetic field..... | 19 |
| 1.5. DISSCUSSION..... | 20 |
| 1.6. CONCLUSION..... | 22 |
| 2. COMMON MODE CURRENT ESTIMATION FOR CABLE BUNDLE INSIDE A VEHICLE | 23 |
| 2.1. INTRODUCTION | 23 |
| 2.2. ENGINEER SOLUTION..... | 24 |
| 2.3. METHOD OF MOMENT..... | 32 |
| 2.3.1. EFIE with RWG Basis Functions. | 32 |

| | |
|---|-----|
| 2.3.2. Scattered Field by Induced Surface Current Density. | 37 |
| 2.3.3. Arbitrary Thin Wire (ATW) Approximation. | 38 |
| 2.3.4. Lumped Element on ATW Wire Segment. | 42 |
| 2.3.5. Discrete Voltage Source on ATW Wire Segment. | 44 |
| 2.3.6. Interaction between Surface and ATW Wire Segment. | 45 |
| 2.4. PARTIAL CIRCUIT ELEMENT EXTRACTION FROM MOM | 46 |
| 2.4.1. Surface Structure. | 46 |
| 2.4.2. Thin Wire Structure. | 50 |
| 2.4.3. Interaction between Surface and Thin Wire Structures. | 54 |
| 2.4.4. Pseudo Node Concept and Case Validation. | 56 |
| 2.5. MTL WITH INCIDENT FIELD | 60 |
| 2.5.1. Conventional Theory of TL-Mode Current Excited by External Fields. | 60 |
| 2.5.2. Exact TL-, Antenna-Mode Current on a Two Wire Transmission Line. | 63 |
| 2.5.3. Dealing with TL Terminations. | 73 |
| 2.5.4. Antenna-Mode Current on Multi-conductor Transmission Line | 75 |
| 2.6. MULTI-SCATTERING METHOD. | 75 |
| 2.6.1. Multi-Scattering by Pure MoM. | 76 |
| 2.6.2. Multi-Scattering by Hybrid of MTL and MoM. | 79 |
| 2.7. CONCLUSION. | 87 |
| 3. TSV MODELING USING MODAL BASIS FUNCTIONS | 88 |
| 3.1. INTRODUCTION | 88 |
| 3.2. FORMULATION | 89 |
| 3.3. CALCULATION OF SYSTEM MATRIX | 95 |
| 3.4. A TSV PAIR | 98 |
| 3.5. A TSV ARRAY | 101 |
| 3.6. CONCLUSION. | 103 |
| BIBLIOGRAPHY | 104 |
| VITA | 113 |

LIST OF ILLUSTRATIONS

| | Page |
|---|------|
| Figure 1.1. Definition of the Port Used for Z11 Calculation | 3 |
| Figure 1.2. Structure of the SPICE Model with the Non-linear Arc [12]..... | 5 |
| Figure 1.3. Comparison of Mag(Z11) Obtained from Different Methods..... | 6 |
| Figure 1.4. Comparison of Real(Z11) and Imag(Z11) Obtained from Different Methods | 7 |
| Figure 1.5. Equivalent Circuit of an ESD Generator [4]. Rt and Ri Represent the Current Target Resistance and Input Impedance of the Oscilloscope..... | 7 |
| Figure 1.6. Simulated Discharge Currents of an ESD Generator Discharging to a Ground Plane in Air Discharge Mode at a 5 kV Charge Voltage | 8 |
| Figure 1.7. Comparison of Currents Discharging to Ground Plane for a 0.3 mm Arc Length and Measured Current for a Fast Approach Speed | 9 |
| Figure 1.8. Comparison of Currents Discharging to Ground Plane for a 0.7 mm Arc Length and Measured Current for a Medium Approach Speed | 10 |
| Figure 1.9. Comparison of Currents Discharging to Ground Plane for a 1.1 mm Arc Length and Measured Current for a Slow Approach Speed..... | 10 |
| Figure 1.10. Full Wave Model of the ESD Generator and MP3 Player | 11 |
| Figure 1.11. Location of the Z11 Port..... | 12 |
| Figure 1.12. Simulated Z11 of the ESD Generator Discharging to a Small Product .. | 12 |
| Figure 1.13. Simulated Discharge Current of the ESD Generator Discharging into the MP3 in the Air Discharge Mode at a 5 kV Charge Voltage..... | 13 |
| Figure 1.14. Comparison of the Port Voltage in SPICE and CST Model of Case I.... | 14 |
| Figure 1.15. Measurement Setup. The F-65 Current Clamp was Placed around the Discharge Tip and above the Product..... | 15 |
| Figure 1.16. Measurement Setup. The Foam Prevents Direct Contact of the Current Probe with the MP3 Player or the ESD Generator. The H-field Probe was Placed about 5 cm away from the Discharge Point.... | 16 |
| Figure 1.17. Measured Discharge Current of Short Ground Strap | 17 |
| Figure 1.18. Simulated Discharge Current for a 0.3 mm Arc Length and Measured Current for a Fast Approach Speed | 18 |
| Figure 1.19. The Comparison of Simulated Discharge Current for a 0.7 mm Arc Length and Measured Current for a Medium Approach Speed | 18 |
| Figure 1.20. Simulated Discharge Current for a 1.1 mm Arc Length and Measured Current for a Slow Approach Speed..... | 19 |

| | |
|--|----|
| Figure 1.21. Measured and Simulated Magnetic Field at 5 cm away from the Discharge Point | 20 |
| Figure 2.1. Equivalence and Extraction of the Antenna Impedance..... | 25 |
| Figure 2.2. Real and Imaginary Part of the Radiation Impedance..... | 25 |
| Figure 2.3. Incorporate MTL with Equivalent Radiation Impedance..... | 26 |
| Figure 2.4. Writing KVL around the Small Segment Δz | 26 |
| Figure 2.5. MTL With Ground Impedance In The Current Return Path | 27 |
| Figure 2.6. S-parameters Comparison from Different Approaches | 28 |
| Figure 2.7. Equivalent Radiation Impedance Could Be Considered as a Two-Port Network | 29 |
| Figure 2.8. Equivalent Circuit Network of Multiple Bundles in Small Segment of Δz | 30 |
| Figure 2.9. S-parameters Comparison from Different Approaches for Multi-Bundle Transmission Line | 32 |
| Figure 2.10. Discretization of Surface Structure by Triangles | 34 |
| Figure 2.11. RWG Basis Function Illustration | 35 |
| Figure 2.12. Rooftop Basis Functions (End Condition 1) | 39 |
| Figure 2.13. Rooftop Basis Functions (End Condition 2) | 39 |
| Figure 2.14. Rooftop Basis Function for Thin Wire Approximation | 40 |
| Figure 2.15. Lumped Element Defined on Wire Segment..... | 44 |
| Figure 2.16. Adjustment of Original Impedance Matrix | 44 |
| Figure 2.17. Equivalence of Discrete Voltage Source..... | 45 |
| Figure 2.18. Relation between Nodal Current and Branch Current..... | 48 |
| Figure 2.19. Surface Current Density Distribution on Cell n | 52 |
| Figure 2.20. A Simple Two-conductor Transmission Line | 57 |
| Figure 2.21. Introduction of Pseudo Cell..... | 57 |
| Figure 2.22. Validation by Comparing Z-parameter from Different Approaches | 58 |
| Figure 2.23. Conversion to Norton Equivalent Circuit..... | 58 |
| Figure 2.24. KCL for Pseudo Nodes..... | 60 |
| Figure 2.25. Current along Transmission Line | 61 |
| Figure 2.26. Equivalent Circuit of Taylor's Model | 62 |
| Figure 2.27. Equivalent Circuit of Agrawal's Model | 62 |
| Figure 2.28. Equivalent Circuit of Rachidi's Model..... | 62 |
| Figure 2.29. Magnitude of Green's Functions | 65 |

| | |
|--|----|
| Figure 2.30. TL-mode Line Per-Unit-Length Inductance..... | 66 |
| Figure 2.31. TL-mode Line Per-Unit-Length Capacitance..... | 67 |
| Figure 2.32. Antenna-mode Line Per-Unit-Length Inductance | 68 |
| Figure 2.33. Antenna-mode Line Per-Unit-Length Capacitance | 69 |
| Figure 2.34. T-Shape Lumped Circuit Representation of TL..... | 69 |
| Figure 2.35. Plane Wave Excitation onto an Open Loaded Two-Wire TL | 72 |
| Figure 2.36. Magnitude Comparison of Antenna-mode Current..... | 73 |
| Figure 2.37. Boundary Conditions in Total Voltage Form | 74 |
| Figure 2.38. Boundary Conditions in Scattered Voltage Form | 75 |
| Figure 2.39. Flowchart of Multi-Scattering Method by Pure MoM | 77 |
| Figure 2.40. Test Structure For Validating Multi-Scattering Approach..... | 78 |
| Figure 2.41. Current Comparison of Multi-Scattering And Full-Wave Approach..... | 79 |
| Figure 2.42. Flowchart of Multi-Scattering Method by Hybrid of MTL and MoM.... | 80 |
| Figure 2.43. Initial Current along Wire-1 | 80 |
| Figure 2.44. Calculate Induced Surface Current in the Absence of Wires | 81 |
| Figure 2.45. The 1 st Scattered E-field along Wire Surface | 81 |
| Figure 2.46. Convergence of TL-mode Current due to External Field..... | 82 |
| Figure 2.47. Convergence of antenna-mode Current due to External Field | 83 |
| Figure 2.48. Comparison of TL- and Antenna-Mode Current in 1 st Scattering..... | 83 |
| Figure 2.49. Comparison of TL- and Antenna-Mode Current in 2 nd Scattering..... | 84 |
| Figure 2.50. Comparison of TL- and Antenna-Mode Current in 3 rd Scattering | 84 |
| Figure 2.51. Total Current Convergence, 0 th Scattering | 85 |
| Figure 2.52. Total Current Convergence, 1 st Scattering | 86 |
| Figure 2.53. Total Current Convergence, 2 nd Scattering | 86 |
| Figure 2.54. Total Current Convergence, 3 rd Scattering..... | 87 |
| Figure 3.1. A Cross-Sectional View of A TSV Array | 90 |
| Figure 3.2. Evaluating the Matrix Element in $\overline{[\mathbf{D}]}$: Testing and Basis Functions are Located in the Same Local Coordinate System..... | 97 |
| Figure 3.3. Evaluating the Matrix Element in $\overline{[\mathbf{D}]}$: Testing and Basis Functions are Located in Different Local Coordinate Systems | 98 |
| Figure 3.4. Admittance Results for a Typical TSV Pair: $d = 15\mu\text{m}$; $r_{\text{TSV}} = 2.5\mu\text{m}$; $t_{\text{ox}} = 0.5\mu\text{m}$; $\rho_{\text{Si}} = 10\Omega\text{-cm}$ | 99 |

| | |
|---|-----|
| Figure 3.5. Admittance Results for a Typical TSV Pair: $d = 7\mu\text{m}$; $r_{\text{TSV}} = 2.5\mu\text{m}$; $t_{\text{ox}} = 0.5 \mu\text{m}$; $\rho_{\text{Si}} = 10 \Omega\text{-cm}$ | 100 |
| Figure 3.6. Convergence of the Proposed Approach: $d = 7\mu\text{m}$; $r_{\text{TSV}} = 2.5\mu\text{m}$; $t_{\text{ox}} = 0.5 \mu\text{m}$; $\rho_{\text{Si}} = 10 \Omega\text{-cm}$ | 100 |
| Figure 3.7. A 5-by-5 TSV Array..... | 101 |
| Figure 3.8. Node Pair C_{27} and G_{27}/ω for the 25-via TSV Array: pitch = $7\mu\text{m}$; $r_{\text{TSV}} = 2.5\mu\text{m}$; $t_{\text{ox}} = 0.5 \mu\text{m}$; $\rho_{\text{Si}} = 10 \Omega\text{-cm}$ | 102 |
| Figure 3.9. Convergence Study for Node Pair C_{27} and G_{27}/ω | 102 |

LIST OF TABLES

| | Page |
|--|------|
| Table 1.1. Four Step Process for Simulating Air Discharge ESD | 3 |
| Table 1.2. Comparison of Arc Length Effect | 13 |
| Table 3.1. Closed-Form Expressions for Calculating Electric Field and Potential | 96 |
| Table 3.2. Time Consumption of Proposed Method..... | 103 |

1. FULL WAVE SIMULATION OF AN ELECTROSTATIC DISCHARGE GENERATOR DISCHARGING IN AIR DISCHARGE MODE

1.1. INTRODUCTION

Simulating Electrostatic Discharge (ESD) allows predicting the currents and fields seen within a DUT during an ESD, thus it helps to predict failure levels [1], [2]. The most commonly used test standard IEC 61000-4-2 [3] requires using contact mode discharges to metallic surfaces and air discharge mode to non-conducting surfaces. If an air discharge is attempted to a non-conducting surface a discharge to a conducting part can occur.

In contact mode the output wave form is proportional to the charge voltage, thus, the ESD generator can be analyzed as a linear system in both time and frequency domain [4]. Those models differ in the software used, the upper frequency limits, and if a specific commercial model of an ESD generator is simulated. However, the numerical modelling of an air discharge is more complex due to the highly non-linear behaviour of the arc [9]-[14]. The generator needs to be separated into the linear sections comprising the metallic elements, resistors, capacitors, and the non-linear arc. It has been shown that the arc can be modelled as a time varying resistor valid for the first 10's of nanoseconds [13]. This model needs to be integrated into the numerical model.

Air discharge currents repeat badly. Even if the voltage and speed of approach are kept the same, ESD currents will vary strongly from discharge to discharge. The variations are due to different arc lengths and not a direct result of corona or speed of approach [13]. Reference [12] shows a method to combine the arc model from Rompe and Weizel with an equivalent circuit of the discharging object. This methodology is expanded in this paper to combine a linear full wave model of the ESD generator and the Device Under Test (DUT) with a non-linear arc model. Currents and fields are obtained.

Section 1.2 introduces the methodology. Sections 1.3 and 1.4 verify the methodology by comparison to measured data. Section 1.5 discusses the application and the limitations of this method.

1.2. METHODOLOGY

In general, different processes are possible for coupling SPICE to a full wave solver: Simultaneous solution exchange voltage and current information with a SPICE like solver after every time step of the full wave solution [15], [16]. Sequential solutions first calculate the S-parameters of the linear section of the circuit and then combine them with the nonlinear part of the circuit in SPICE. We use the second method. It allows re-using the S-parameters to save calculation time if only the arc parameters are changed.

More in detail, a four step process is used which simulates linear parts in full wave and non-linear in SPICE. The arc attaches at two points: At the ESD generator tip and at the DUT. These two points are used to define a port. In the first step the impedance at this port is calculated. This is the impedance looking into the DUT and a Noiseken ESD generator (ESS-2000). The simulation is performed using CST [17]. Both the TD (time domain) and FD (frequency domain) solver can be used. Although the impedance Z_{11} is calculated in the full wave model for a given distance (0.7 mm) between the ESD generator and the DUT as shown in Figure 1.1, different distances will influence the result little as long as the distance is in the arc length range (0.3 mm to 3.0 mm). The tip to ground capacitance is small relative to the distributed capacitance of the rod. This impedance is transformed into a form suitable for time domain simulation. Here the commercial software Broadband SPICE [21] was used. An order of 28 was selected to generate the circuit. SPICE then combines the impedance description from step 1 with an arc model based on the law of Rompe and Weizel. This law describes the arc during the first 10's of nanoseconds as a resistance and has been validated for ESD applications [18], [19]. The resulting current is re-imported into CST as the excitation waveform of the current port which is placed between the two points that had been previously selected to define the impedance port to calculate Z_{11} to obtain fields and currents within the ESD generator and the DUT. The process is summarized in Table 1.1.

The detailed combination in SPICE is now shown. The Z_{11} describes the linear part of the system. Once the Z_{11} has been obtained, it needs to be transformed into a form suitable for time domain simulation. Software tools like IDEM [20] or Broadband SPICE [21] have been used successfully in this research. The sub-circuit created from

Z_{11} is not unique. Its complexity can be user defined which depends on the transformation algorithm, the error, and the order of interest.

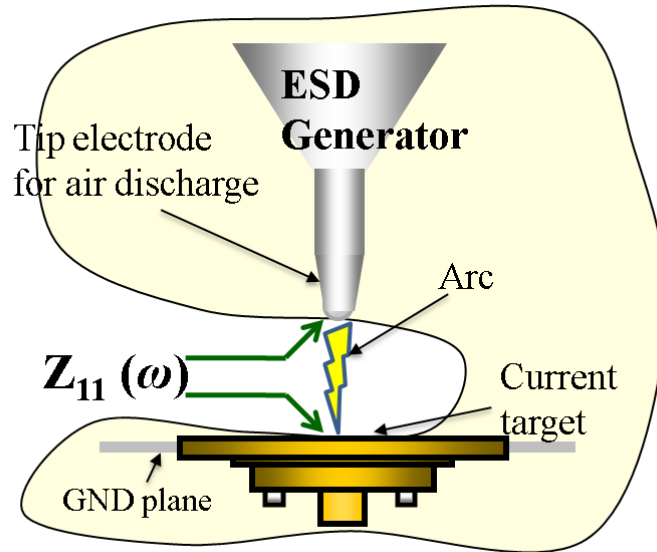


Figure 1.1. Definition of the Port Used for Z_{11} Calculation

Table 1.1. Four Step Process for Simulating Air Discharge ESD

| Step # | Method Description |
|--------|---|
| 1 | Obtain Z_{11} from the two points at which the arc attaches (looking into ESD generator and the DUT) using a full wave model. The DUT's inner details are not of concern in this step, as one only needs to know the impedance seen by the spark. |
| 2 | Obtain a time domain simulation suitable description of Z_{11} . The IDEM (Identification of Electrical Macromodels) tool [20] and Broadband SPICE [21] have been utilized. |
| 3 | Combine the equivalent sub-circuit with the arc length model in SPICE to simulate the time domain discharge current waveform. |
| 4 | Re-import the discharge current waveform $[I(t)]$ back into the full wave model as a port excitation signal and simulate $V(t)$ (for verification against the $V(t)$ obtained from SPICE), $E\text{-field}(t)$, and $H\text{-field}(t)$ in the full wave simulation. In this step a much more detailed model of the DUT can be used. |

The arc of an ESD can be modelled by breaking it down into different phases. The first phase is the resistive phase. The arc is best modelled by a time varying resistance. In the second phase, which is usually reached after a few 10's of nanoseconds, the impedance of the external circuit is larger than the impedance of the arc. In this case the arc often acts more as a constant voltage drop of about 25 V-40 V. The rising edge of the ESD is the main contributor to radiated and inductive coupling into DUTs. For that reason, we concentrate on the resistive phase and do not model other aspects (e.g., how the arc extinguishes). Multiple models describe the resistive phase or arcs [18], [19], [20]. In [13], it has been shown that the model of Rompe and Weizel's is most suitable for ESD simulation as it can correctly describe the effect of the arc length on the rise time and peak current. The arc resistance can be calculated by (1) [13]:

$$R(t) = d / \sqrt{2a \int_0^t i(\xi)^2 d\xi} \quad (1)$$

where R is the arc resistance (Ω), d is the arc length (m), a is the empirical constant, most empirically derived values are $a = (0.5-1) \times 10^{-4} \text{ m}^2/\text{V}^2 \text{ s}$ and $i(\xi)$ is the discharge current (A).

The structure of the SPICE model is shown in Figure 1.2. A step function having a rise time of approximately 30 ps was used as the source. The rise time is selected by two criteria: If it is too long, then it will influence the current rise time. The current rise time should be determined only the arc resistance law and the linear equivalent circuit. Further, the rise time cannot be too small, if the pulse contains strong frequency components beyond the range in which the impedance is calculated it can lead to instabilities in the SPICE simulation. The fast voltage rise starts the arc resistance model. The current rise time is not determined by the rise time of the step function, but by the arc resistance model. The subcircuit represents Z11. The user provides the voltage and the arc length to calculate the discharge currents. The longest possible arc length in a homogeneous field is given by the Paschen law [13]. Such arc lengths would occur in air discharge for low approach speeds or in humid air conditions. The long arc length leads to slow rise times and lower peak values. Longer arc lengths than the length given by Paschen's equation are possible in strongly non-homogeneous fields, e.g., if the discharge is between an ESD generator and a sharp edged metal part or if the discharge is gliding

on a non-conducting surface. Very short arc lengths occur at high approach speeds and in dry air [9], [13], [23], leading to fast rise times and very high peak current values.

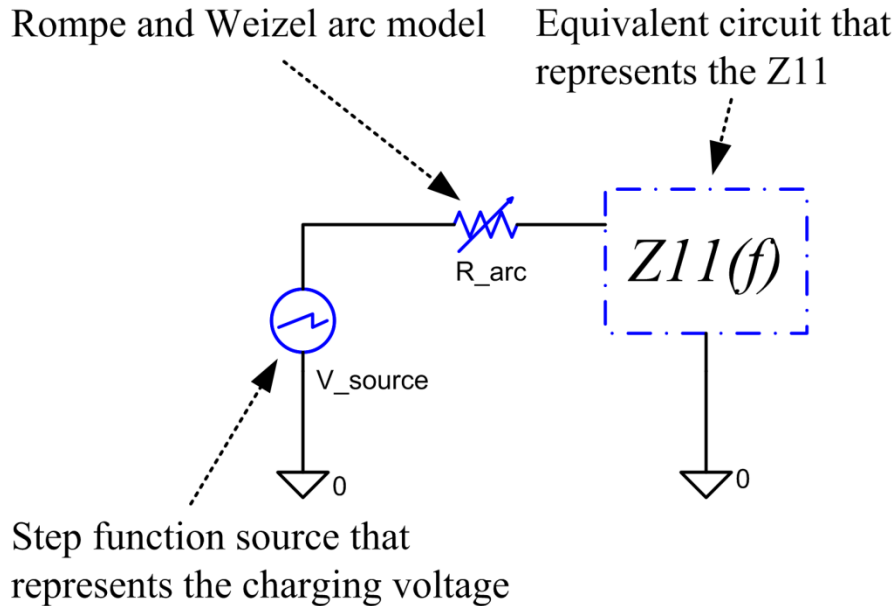


Figure 1.2. Structure of the SPICE Model with the Non-linear Arc [12]

In the following we will first apply this methodology to a discharge to a ground plane, mainly for verification purposes, and then to a discharge to a small MP3 player.

1.3. CASE 1: ESD GENERATOR DISCHARGE TO A GROUND PLANE

1.3.1. $Z11$ between the Tip of the ESD Generator and the Ground Plane.

The structural and discrete elements of the ESD generator are linear with respect to voltage. We further assume that the DUT acts linearly. For obtaining the current injected by the arc, this does not require that no non-linear effects take place inside the DUT; it only requires that the current injected into the DUT is proportional to the charge voltage. For example, if an internal ESD protection device would clamp a trace voltage while the ESD current is injected into the ground system of the DUT, then this clamping would have hardly any effect on the current, thus, the DUT would act as a linear device as seen by the ESD generator. However, if secondary breakdown occurs, e.g., a spark within an attached 2-wire power supply, then this could strongly affect the ESD current, thus the modelling approach might lead to wrong results.

Both time and frequency domain solvers can be used to obtain Z_{11} . We observed the frequency domain simulation giving a more reasonable Z_{11} result and using less simulation time. The simulated Z_{11} for the structure of the ESD generator above a ground plane is shown in Figure 1.3 as the dotted line. This result is verified by comparison with measurement, as shown in Figure 1.4, and an approximate SPICE model of this ESD generator [4]. The model contains sufficient detail for achieving a good match to measured impedance data, and correctly represents the 110 pF capacitor and 330 Ω resistor structure inside the ESD generator at lower frequencies. The calculation takes about 15 hours on a PC (CPU 3.20 GHz, 16G RAM).

ESD generators have long ground straps. It increases the simulation time if the full length is included into the simulation domain. As most disturbances are caused by the fast changing parts of the currents and fields, one may not need to include the full ground strap into the model. The ground strap mainly influences the falling part of the waveform. The SPICE model shown in Figure 1.5 includes a 3500 nH inductor to model the ground strap. A shorter ground strap will reduce the time between the first and the second peak of the discharge waveform.

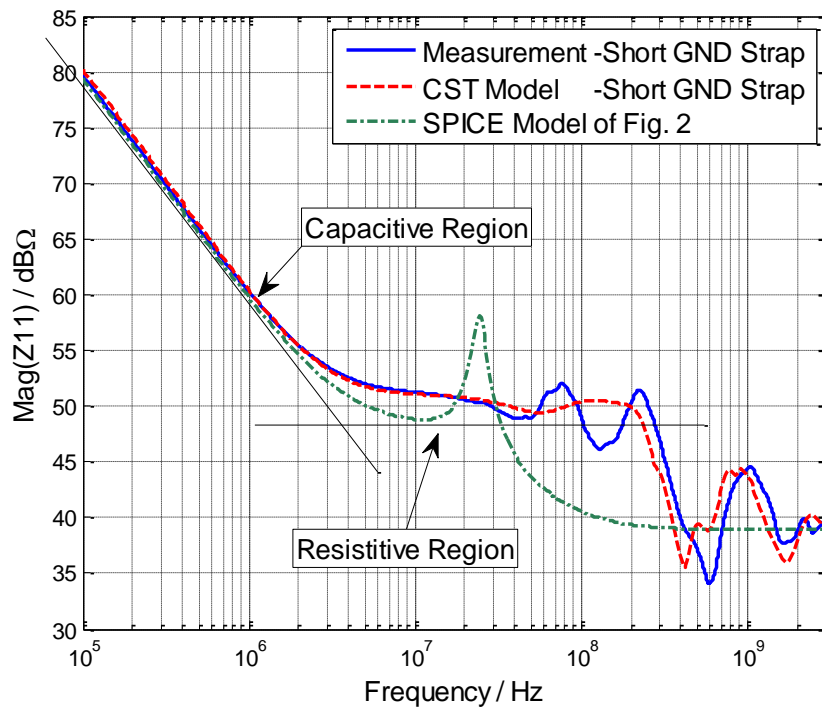


Figure 1.3. Comparison of $\text{Mag}(Z_{11})$ Obtained from Different Methods

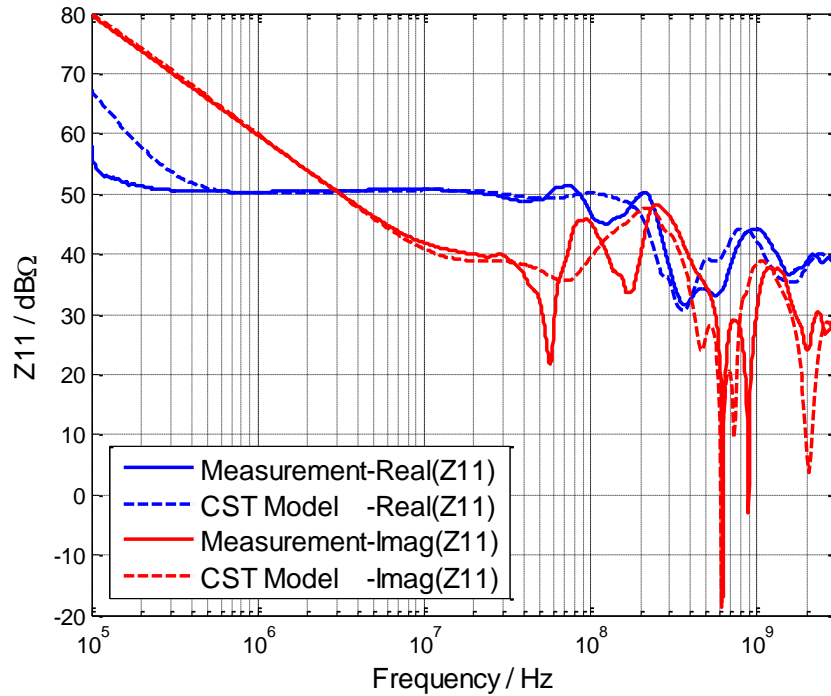


Figure 1.4. Comparison of Real(Z_{11}) and Imag(Z_{11}) Obtained from Different Methods

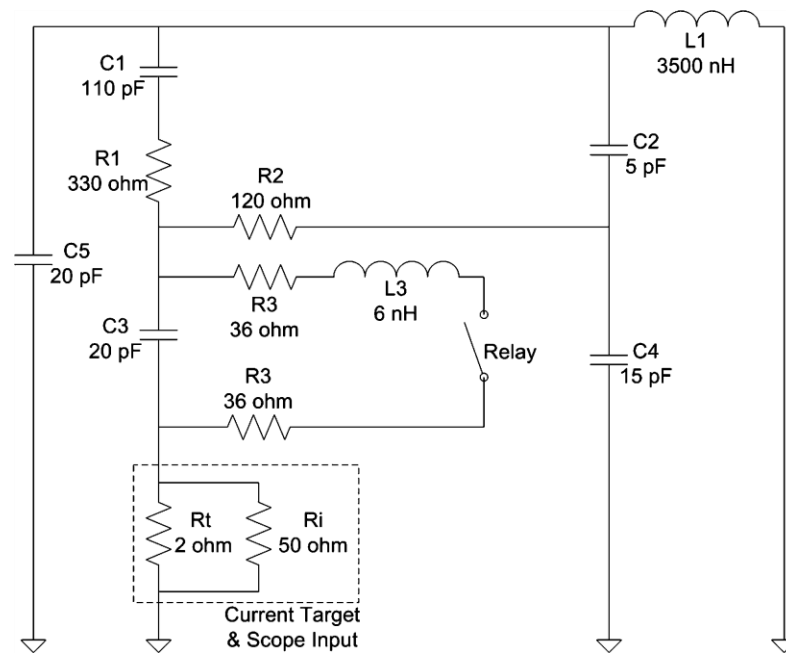


Figure 1.5. Equivalent Circuit of an ESD Generator [4]. R_t and R_i Represent the Current Target Resistance and Input Impedance of the Oscilloscope

The first step obtained the impedance representing an ESD generator discharges to a large ground plane. In the next step the impedance is transformed into the time domain suitable form and combined with a nonlinear arc equation in SPICE.

1.3.2. SPICE Simulation for the Discharge Current. Figure 1.6 illustrates the effect of the arc length on the current waveform. It shows SPICE simulated discharge currents for a 5 kV charge voltage. An arc length of 1.1 mm equals the Paschen length, such a discharge current would be expected at high humidity and slow approach speeds. A more typical value at moderate approach speeds is 0.7 mm. At this value the rise time will be somewhat similar to the rise time of an ESD as given in the IEC 61000-4-2 standard (about 850 ps). A more extreme case is given by the 0.3 mm arc length simulation. Very dry air and high approach speeds might lead to such a discharge. The simulated current peak value is 26 A and the rise time is 150 ps.

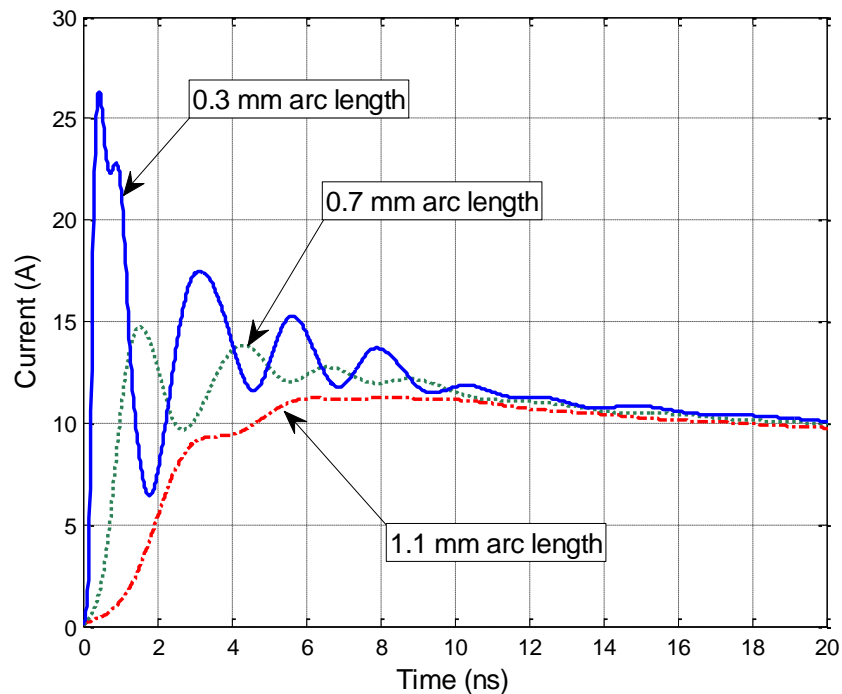


Figure 1.6. Simulated Discharge Currents of an ESD Generator Discharging to a Ground Plane in Air Discharge Mode at a 5 kV Charge Voltage

1.3.3. Re-import of Currents into CST. For obtaining the fields, one needs to re-import the discharge current into the full wave model as the excitation waveform. This is discussed and validated in the second case example.

1.3.4. Validation by Measurement Results. The current into the large ground plane was measured using an ESD current sensor as described in [3]. In Figure 1.7 through Figure 1.9, the SPICE simulated discharge currents are compared to the measured data for different approach speeds. Even if the exact approach speed or arc length are not known, it shows that the ranges of arc lengths used in the simulation are representative for discharge currents obtained in the experiment. A more in-depth comparison based on measured arc length values can be found in [13].

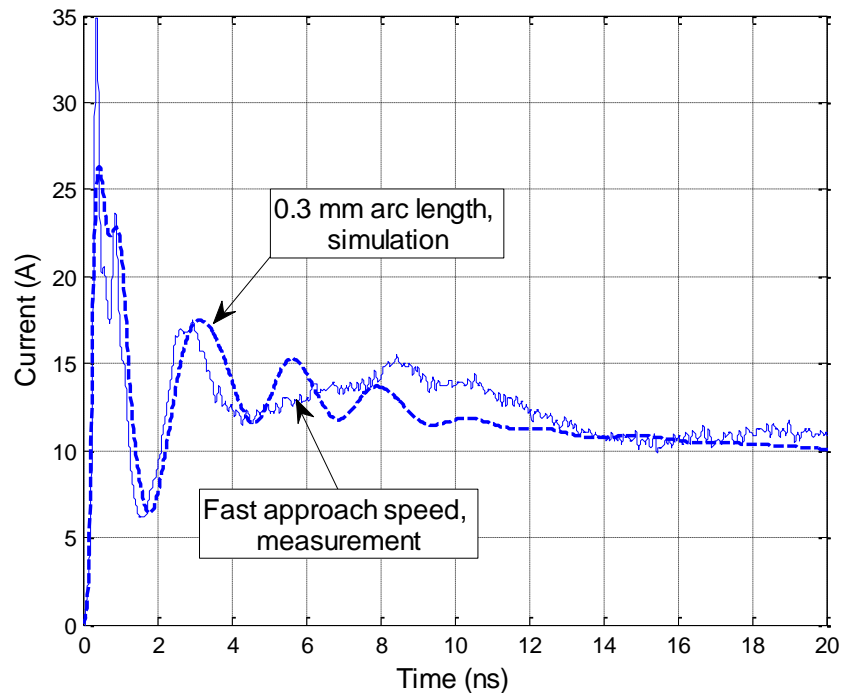


Figure 1.7. Comparison of Currents Discharging to Ground Plane for a 0.3 mm Arc Length and Measured Current for a Fast Approach Speed

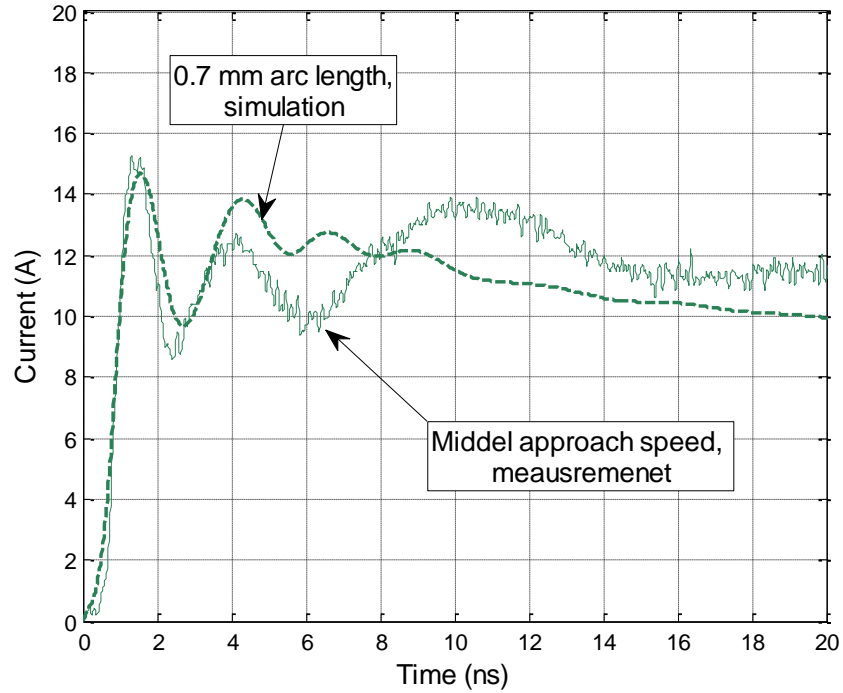


Figure 1.8. Comparison of Currents Discharging to Ground Plane for a 0.7 mm Arc Length and Measured Current for a Medium Approach Speed

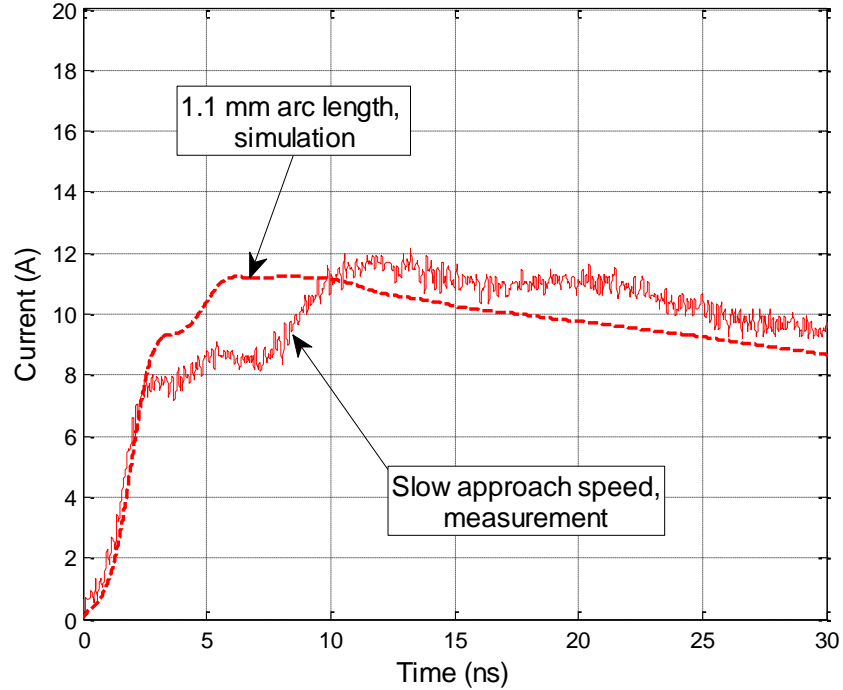


Figure 1.9. Comparison of Currents Discharging to Ground Plane for a 1.1 mm Arc Length and Measured Current for a Slow Approach Speed

1.4. CASE 2: ESD GENERATOR DISCHARGE INTO A PRODUCT

1.4.1. Z_{11} between the Tip of the ESD Generator and the Ground Plane.

This case simulates a discharge into an MP3 player, a small, non-grounded DUT. The whole geometry is shown in Figure 1.10. The MP3 player model includes the main blocks of the DUT similar to [24]. In brief, the major blocks of the player (metal frame, battery, display, PCBs) are modelled as metal blocks connected at locations of connectors and frame connection points.

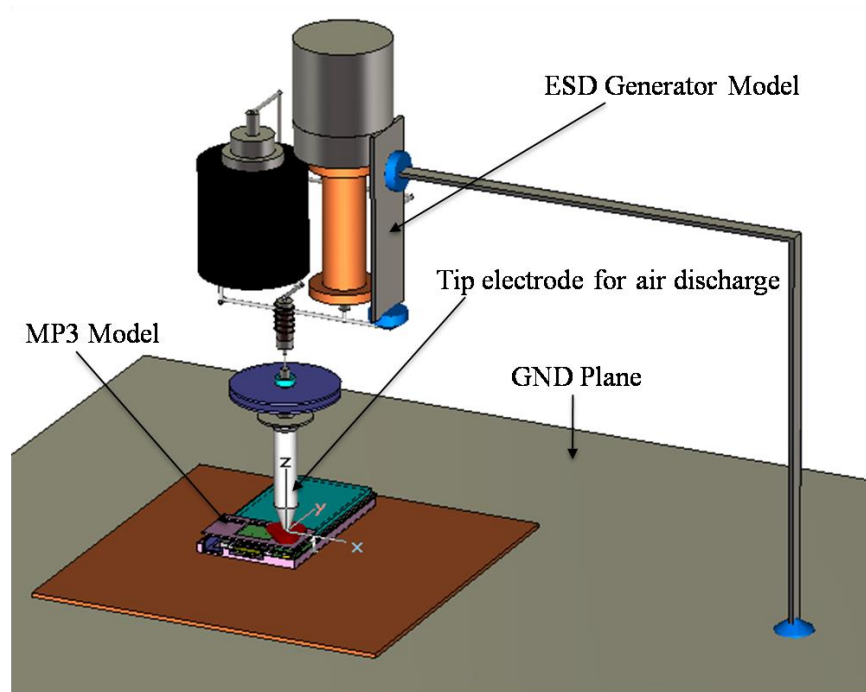


Figure 1.10. Full Wave Model of the ESD Generator and MP3 Player

The DUT is placed on a dielectric sheet above a larger ground plane. This forms a capacitor having a capacitance of about 25 pF, leading to a higher value of Z_{11} at lower frequencies. The value for Z_{11} was obtained as shown in Figure 1.11. The comparison between Z_{11} of the ESD generator and the large ground plane and Z_{11} of the ESD generator with the MP3 player is shown in Figure 1.12. It mainly shows the smaller capacitance at lower frequencies; at higher frequencies the impedance of the 25 pF capacitor formed by the player against the ground plane is lower than the source

impedance of the ESD generator, thus the impedance in case 2 is similar to the impedance seen in case 1, the discharge to a large ground plane.

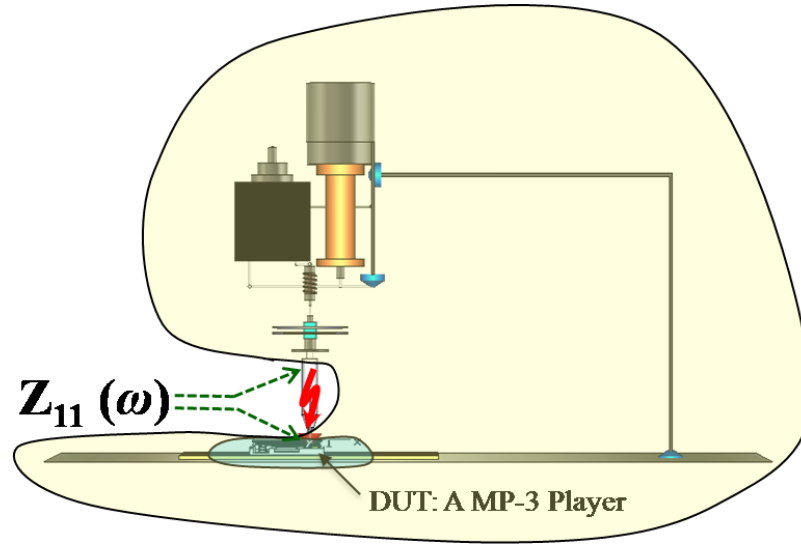


Figure 1.11. Location of the Z11 Port

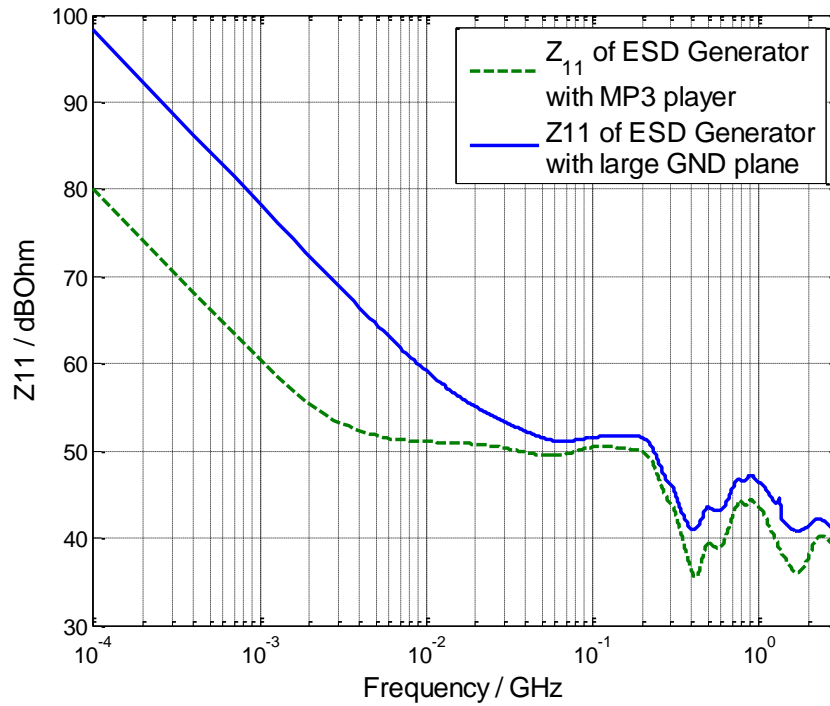


Figure 1.12. Simulated Z_{11} of the ESD Generator Discharging to a Small Product

1.4.2. SPICE Simulation for the Discharge Current. The Z11 defined between the discharge tip and the MP3 player was transformed into a subcircuit using Broadband SPICE. The subcircuit combined with the arc model gave the simulated discharge current for different user-defined charging voltage and arc length. The simulated discharge current at the 5 kV charge voltage with different arc lengths is shown in Figure 1.13.

The obtained peak values and rise times are tabulated in Table 1.2. The arc length has a very strong effect on the parameters shown, especially, the current derivative.

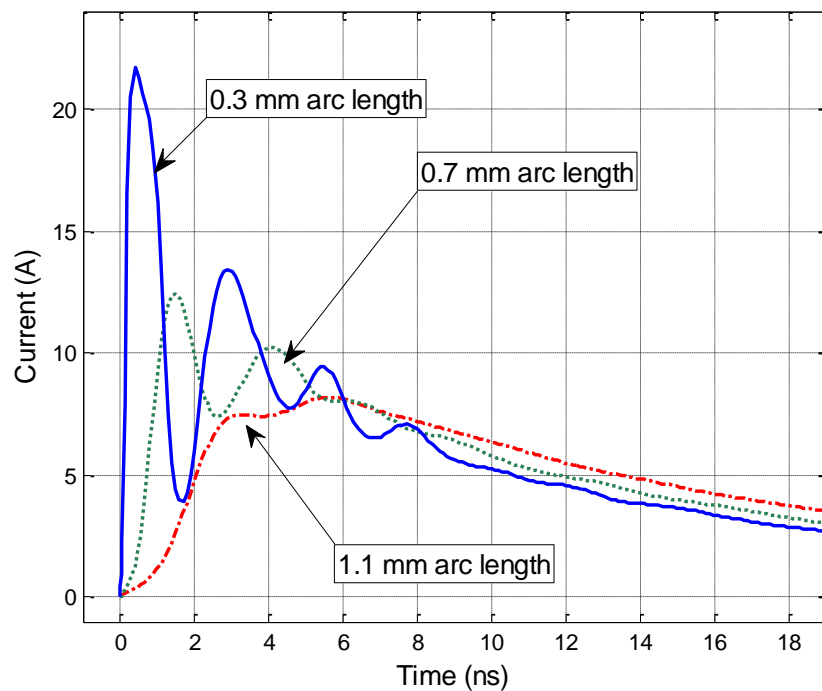


Figure 1.13. Simulated Discharge Current of the ESD Generator Discharging into the MP3 in the Air Discharge Mode at a 5 kV Charge Voltage

Table 1.2. Comparison of Arc Length Effect

| Arc Length | peak value (A) | rise time (ps) | max di/dt (A/ns) |
|------------|----------------|----------------|------------------|
| 0.3 mm | 21.7 | 200 | 105.19 |
| 0.7 mm | 12.4 | 780 | 16.617 |
| 1.1 mm | 8.1 | 2260 | 4.5170 |

1.4.3. Re-import of Currents into CST. To obtain transient fields the current waveform obtained from the SPICE simulation is re-imported into CST as the excitation waveform. The current source port is placed between the two points that had been previously selected to define the impedance port to calculate Z_{11} . One check is worthwhile: If the Z_{11} representation used in SPICE would perfectly match the Z_{11} from the frequency domain full wave simulation then the port voltage obtained during the full wave simulation using the re-imported current would match the port voltage (=voltage across the arc) in the SPICE simulation.

For Case II, the SPICE simulated current was imported back to the CST model as the current source. The comparison of the port voltage in the SPICE model and the port voltage in the CST model in Figure 1.14 shows a good match.

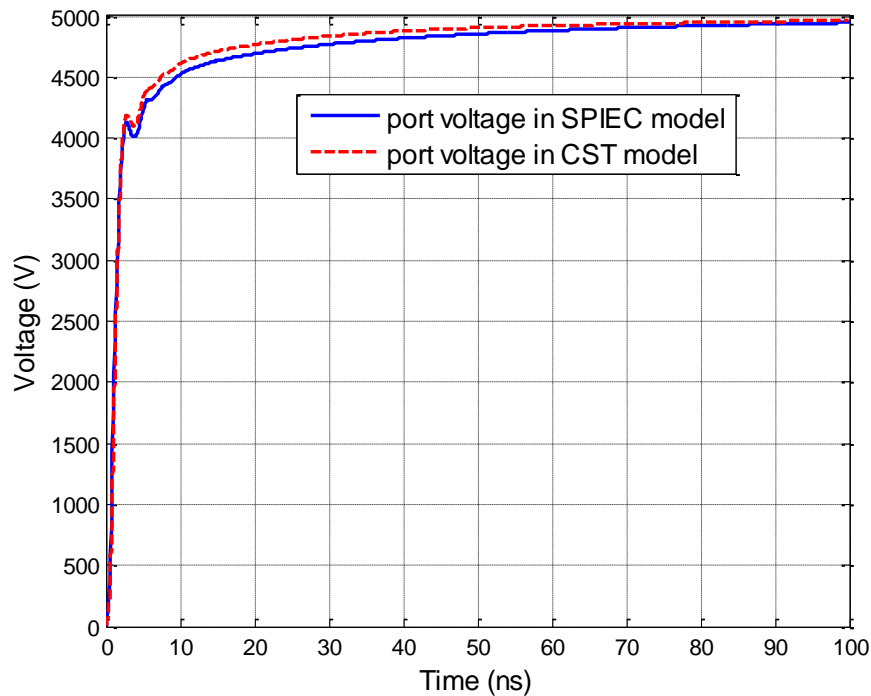


Figure 1.14. Comparison of the Port Voltage in SPICE and CST Model of Case I

The simulation using the re-imported current allows simulating the fields within and around the MP3 player by placing appropriate monitor probes. If these probes are placed close to the metallic surfaces of the MP3 player, then they represent the surface

current densities and the displacement current densities which can be used to estimate the coupling into bond wires of an IC, traces, and flex cables for predicting ESD upset threshold levels. Before current and field results are shown, the measurement methods are introduced.

1.4.4. Validation by Measurement Results. The current was injected into the small product and the magnetic field was measured. To capture the current injected into the MP3 player, an F-65 (1 MHz – 1 GHz) current probe was used as shown in Figure 1.15. The magnetic field was measured using a small shielded loop and a Tektronix 7404 (4 GHz BW, 20 GS/s) oscilloscope.

At 5 kV charge voltage, a NoiseKen ESD generator was discharged into the player. The player was placed above a large GND plane with a dielectric sheet between them. Figure 1.15 and Figure 1.16 illustrate the setup.

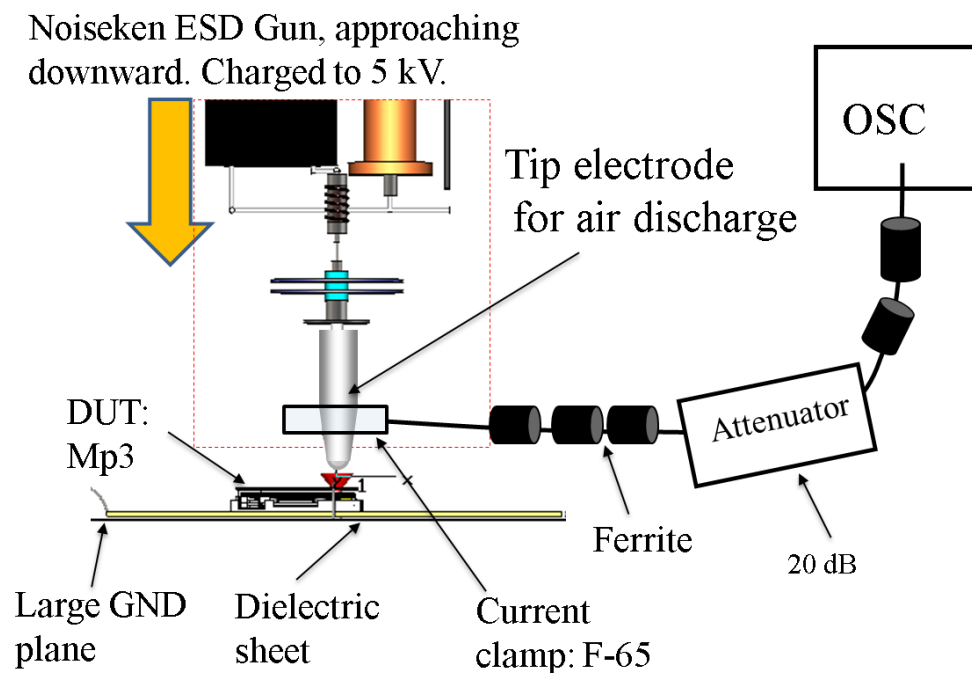


Figure 1.15. Measurement Setup. The F-65 Current Clamp was Placed around the Discharge Tip and above the Product

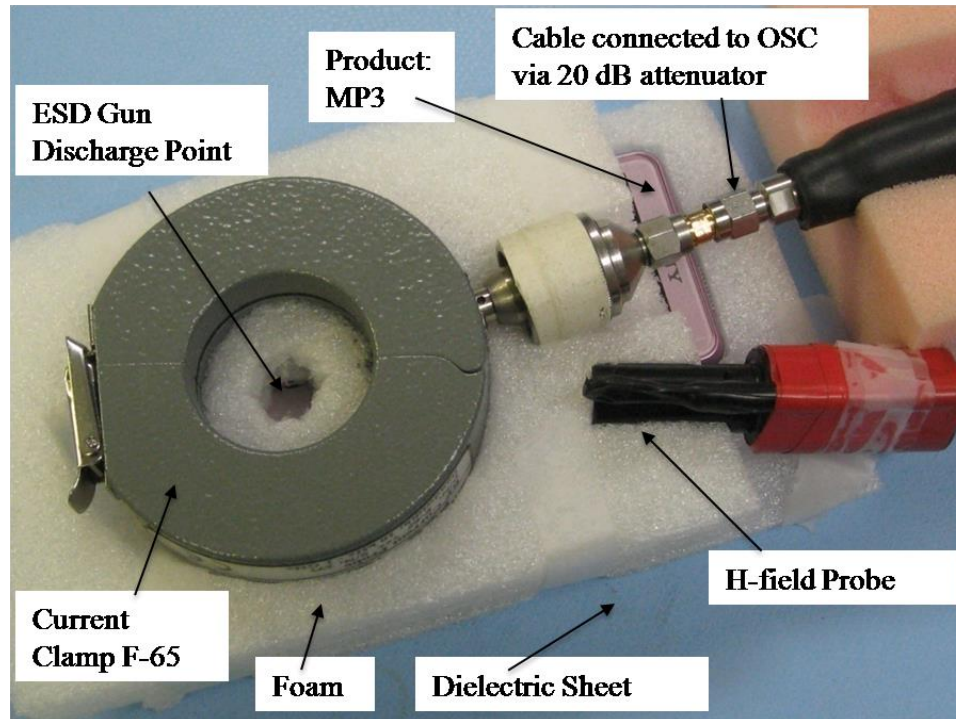


Figure 1.16. Measurement Setup. The Foam Prevents Direct Contact of the Current Probe with the MP3 Player or the ESD Generator. The H-field Probe was Placed about 5 cm away from the Discharge Point

The relationship between approach speed, humidity, and arc length is not of deterministic nature, but given by the influence of the humidity on the statistical time lag [13]. Thus, on average one will observe shorter arc lengths with increasing approach speeds for a given charge voltage. For achieving short arc length discharges without reducing the humidity, the surface had been cleaned using alcohol and fast approach speeds have been used, longer arc lengths are achieved by slow approach speeds. Shown are examples of the captured waveforms for different approach speeds.

1.4.4.1 Measured discharge current. The current clamp's frequency response falls off above 1 GHz bandwidth, thus the fastest rise time of a step response signal would be approximately 300 ps. Figure 1.17 shows measured discharge currents for different approach speeds.

The simulation results are compared to the measured results for verification. The fast rise time result is shown in Figure 1.18. The simulated discharge current for a 0.3 mm arc length and 5 kV charging voltage gives a discharge current with a rise time of

about 200 ps and a peak value of 21 A. The measured discharge current has a rise time of about 300 ps and a peak magnitude of about 22 A. The difference can be explained by the limited bandwidth of the F-65 clamp. Due to the difficulty in measuring arc length we can only approximately compare measured and simulated results. Nevertheless, the comparison shows that the simulated and measured data are within the same ranges.

In Figure 1.19 and Figure 1.20, the comparison of simulation discharge current for 0.7 mm and 1.1 mm arc length is shown. They match well with the measured results.

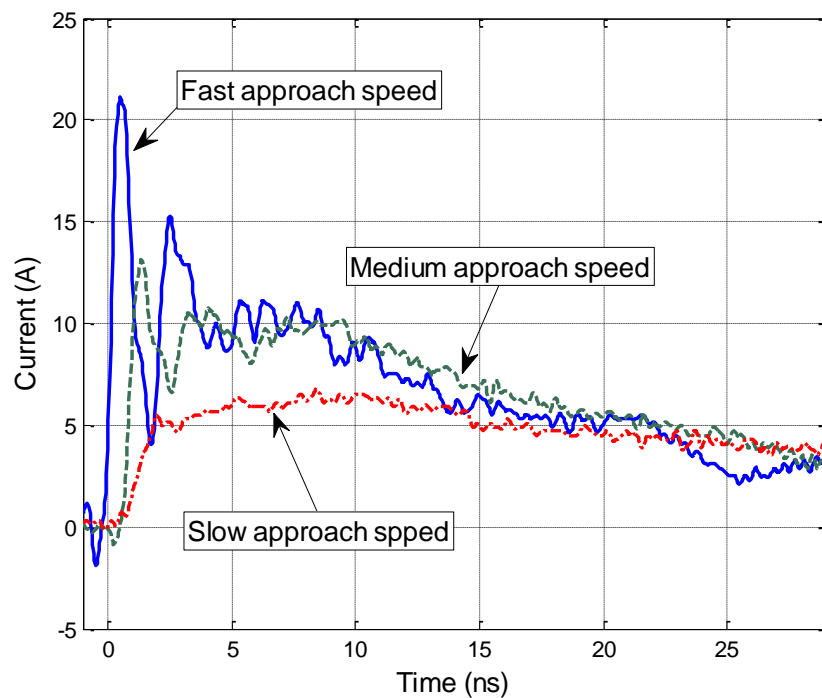


Figure 1.17. Measured Discharge Current of Short Ground Strap

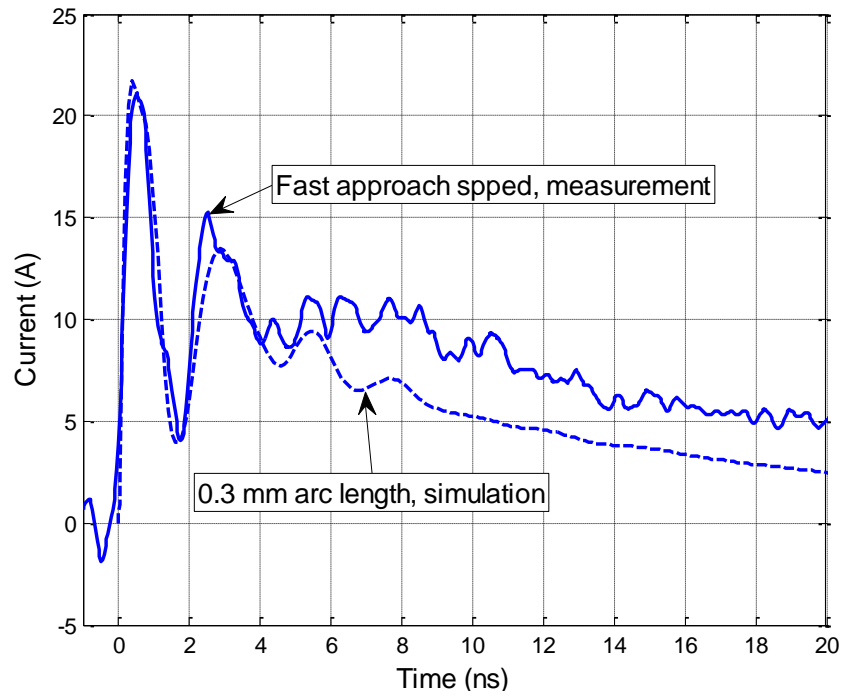


Figure 1.18. Simulated Discharge Current for a 0.3 mm Arc Length and Measured Current for a Fast Approach Speed

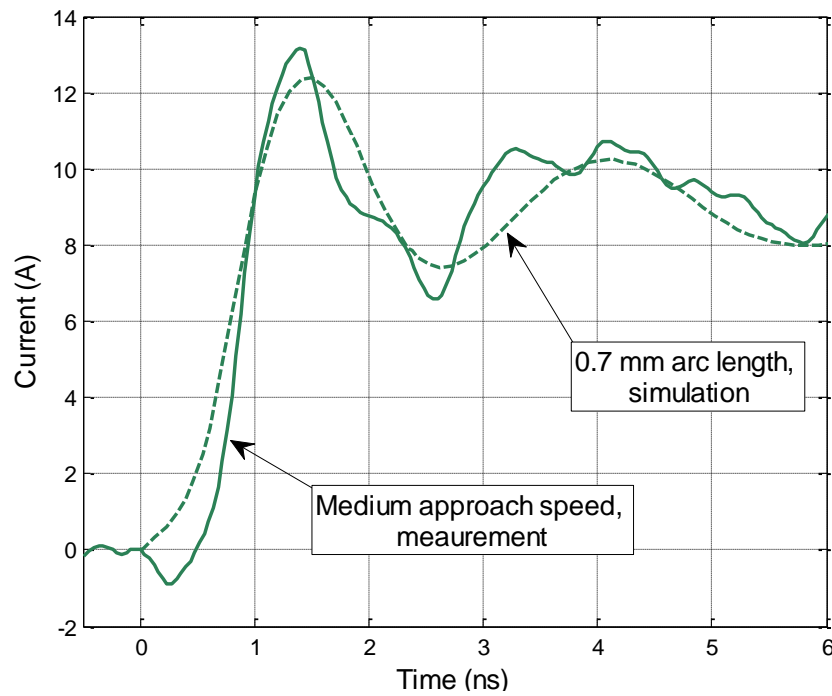


Figure 1.19. The Comparison of Simulated Discharge Current for a 0.7 mm Arc Length and Measured Current for a Medium Approach Speed

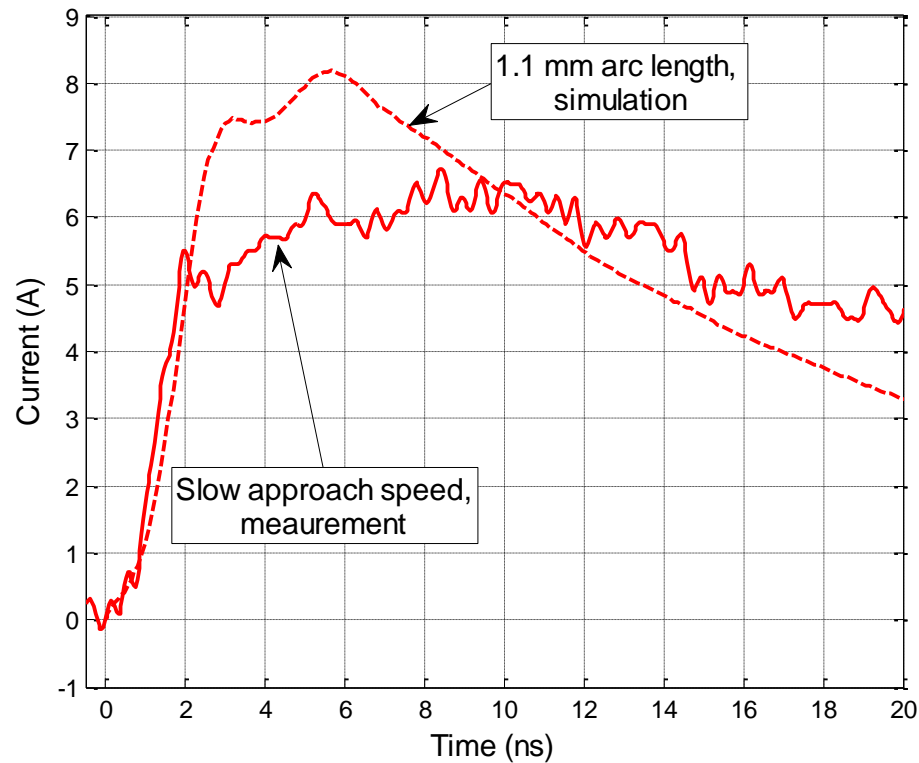


Figure 1.20. Simulated Discharge Current for a 1.1 mm Arc Length and Measured Current for a Slow Approach Speed

1.4.4.2 Measured magnetic field. This is to confirm the last step of the process: Injecting the SPICE simulated current back into the full wave simulation for obtaining fields. A shielded loop was placed 5 cm away from the product (Figure 1.16). A deconvolution was performed to obtain the field strength from the captured voltage at the probe output. The deconvolution is mainly an integration process, having two deviations from the ideal integration. At lower frequencies high pass filtering is performed to avoid the accumulation of the oscilloscope's small but relevant DC offset during the integration. Second, at higher frequencies the self-inductance of the probe in conjunction with the 50 Ω load, leads to a self-integration thus no external integration is needed above 3 GHz. The resulting magnetic fields are shown in Figure 1.21. The data match well. The measured rise time is about 250 ps. Using the SPICE model one can estimate the arc length from the rise time. Repeated simulations indicate an arc length of about 0.4 mm. The Paschen length for 5 kV is about 1.1 mm at sea level air pressure.

Thus, the combination of the speed of approach and the statistical time lag reduced the arc length in this measurement to 35% of the Paschen value, leading to a very fast rising ESD current.

Several field probes were placed in the full wave model to monitor the magnetic field. A probe that is 5 cm away from the discharge point gives the H-field data shown in Figure 1.21. The result matches well with the measured data.

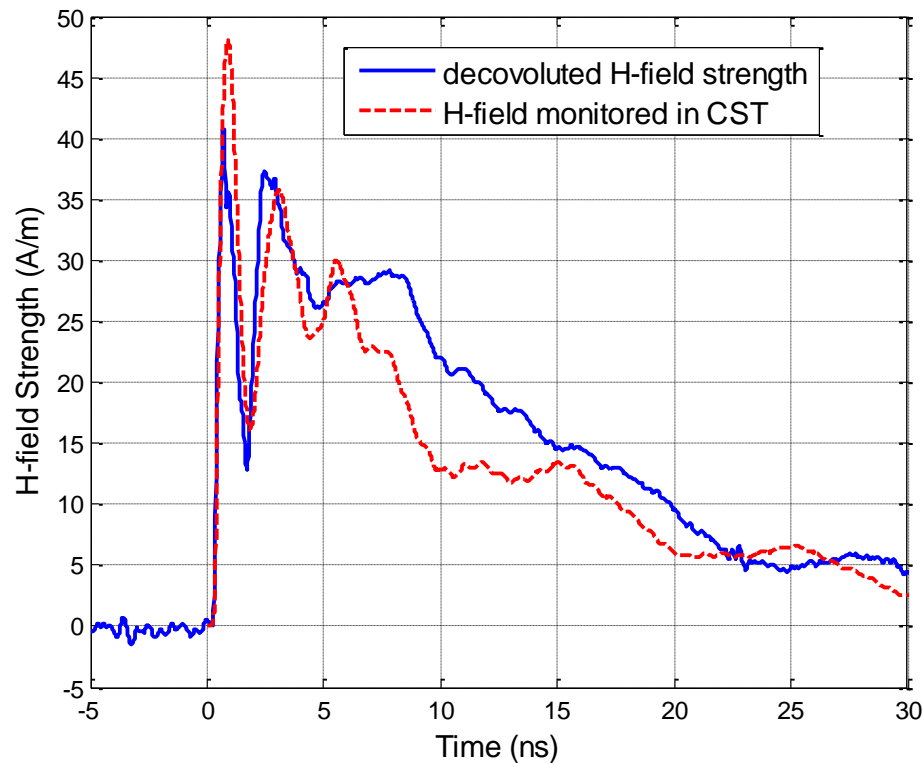


Figure 1.21. Measured and Simulated Magnetic Field at 5 cm away from the Discharge Point

1.5. DISSCUSSION

The methodology allows predicting the currents and fields in and around a product. There are three types of limitations in the methodology.

The most obvious one results from the limited ability of simulating details in the product and within the ESD generator. As with every simulation, the number of unknowns and the ratio of the smallest to the largest detail will limit the size of the

model. The methodology allows circumventing this at least partially, especially for small products. If the product is small, then the fields inside the product will be dominated by the fields caused from the injected current and not by fields directly coupling from the body of the ESD generator. Those fields would especially be significant in the contact mode in which the field components that are greater than 1 GHz are often caused by the rapid voltage breakdown in the gas filled relay that initiates the discharge. As this analysis is for an air discharge, one will find the strongest high frequency components directly at the arc, as with further distance from the arc high frequency components will be attenuated by both frequency dependent loss and radiation. If the fields are dominated by the injected current, then one can use a relatively simple model of the product just to determine the current, but in the last step, in which the current is re-injected into the product, a more complex model of the product can be used, but a very simple model of the ESD generator (and a forced current).

The second limitation results from the need for providing the arc length for the arc resistance calculation. Although possible, arc length measurements are difficult to implement. In a simulation we suggest the following approach. At first, an arc length should be selected that leads to an air discharge current that is similar to the contact mode discharge current, as specified in the IEC 61000-4-2 standard. For 5 kV this is about 0.8 mm arc length. Values for other voltages can be found in [13]. As a very slow rising current the Paschen value can be selected, leading to discharges of lower severity and as extremely fast rising current a value of about 30 % of the Paschen length is suggested. This value is based on experimental evidence. In measurements that captured the arc length [13] we found it possible even under very dry air and clean surface conditions to obtain arc lengths of less than 30 % of the Paschen value.

The third limitation is related to stability of the time domain SPICE simulation. In this simulation a very rapid change of resistance is combined with a SPICE impedance model created from full wave simulation. If instabilities occur, one should inspect the SPICE model for passivity and causality, in addition one can simulate the discharge using longer arc lengths first, as these show a slower change of the arc resistance.

The main application of this model lies in the simulation of ESD to products. For example, it is known that the arc length tends to be small for fast approach speeds in dry

air. The short arc length leads to fast rise times and high peak values. Using this model one can quantify the fields inside a product for different arc lengths. Further applications are the simulation of grounding conditions of products on the arc, and thus the current. Further, the model can be extended to the case of secondary breakdown, e.g., an ESD occurs to an ungrounded metal part leading to a second discharge from this ungrounded part to the main part of the DUT.

1.6. CONCLUSION

The article proposes a method for simulating an ESD generator discharging in air discharge mode into a product. The linear and the non-linear part of the problem are separated to simulate the linear part in a full wave solution and the non-linear arc in SPICE. The SPICE results are re-imported into the full wave problem as the excitation. This allows the fields inside a product during an air discharge to be obtained. The method has been verified by comparison of simulated current and transient field results with measurements.

2. COMMON MODE CURRENT ESTIMATION FOR CABLE BUNDLE INSIDE A VEHICLE

2.1. INTRODUCTION

The modelling of cable bundles inside a vehicle is important for vehicle EMI design. Statistical analysis, fullwave EM method, as well as several hybrid methods has been used to model the cable bundles.

Method of Moment (MoM) is suitable for EMI fullwave simulation because of the advantage of straightforward electrical field integral equation, and the omit of boundary conditions. In conventional MoM, RWG basis functions are used to represent the current density distribution on surface scatters. For a cylindrical thin wire structure, only axial component of current is assumed to exist. And therefore a current filament is used to represent the current density along the wire. The 1D rooftop basis functions are used in this Arbitrary Thin Wire approximation method (ATW).

A cable bundle usually consists of tens of wires, which are further generally twisted. It is very computationally expensive to treat each wire using ATW. The hybrid approach combining Multi-conductor Transmission Line (MTL) theory with 3D MoM has been used in various commercial electromagnetic (EM) tools [25], [26], [27].

In the susceptibility problem, one method is to first compute fields (fields external to cables) using a fullwave field solver that ignores the presence of the cables. Then, one extracts the fields in the cables' vicinity, which are used in conjunction with coupling models to produce source terms for a separate transmission line analysis of guided fields propagating along the cables [35], [36], [37]. This method doesn't consider the reflected fields from cables to the external structures.

In the radiation problem, one method calculates the current along cables with MTL analysis. These currents is then considered as impressed sources for the fullwave field solver, and the radiated field due to external structure scattering is calculated in the absence of cable bundles. Again, this method neglects the reflected fields from the external structures back to cable.

Therefore, another method is proposed that, just as in [35], [36], [37], at first, the cables are ignored, and the external fields in cables' vicinity are computed; these external

fields produce source terms for the transmission line analysis that yields the guided fields. Then, these guided fields produce source terms for the field solver that updates the external fields in the vicinity of the cables accordingly. These new fields are then used to update the guided fields and so on. One reference talks about the electromagnetic field coupling to a line of finite length [50]. In another reference, the surrounding structure is modeled via MoM and SPICE-like simulator is used to simulate equivalent circuit model of the multi-conductor transmission lines extracted via the PEEC method [51], 0.

The modeling of cable bundles with outer environment can be divided into two parts: the wire part and the surface part, and a multi-scattering method can be used. In the wire part problem, MTL per-unit-length (pul) parameters for both TL- and antenna-mode currents can be derived from thin wire approximation MoM. The MTL is excited by a discrete voltage source applied on one end of the wires. The excited current on wires create fields incident to the surface, and induces current density on surface structure. The induced current density on the surface of outer environment due to the incident fields can be easily calculated by conventional 3D MoM. The scattered fields are then calculated in the vicinity of the MTL, illuminating the wire for additional current, including both TL- and antenna-mode. Those illuminated currents can be treated as a small increment of total wire currents. These new current increment will generate new incident fields for the MoM problem, and so on. This multi-scattering process can be repeated several times until the increase of the wire current is smaller than a threshold.

2.2. ENGINEER SOLUTION

When a cable bundle crosses a slotted ground plane below it, the return current could form a loop on the plane, and a typical resonant structure is associated. Equivalent radiation impedance $Z_{antenna}(f)$ can be used to model the slot resonator as shown in Figure 2.1 [54], where the 6 wires are vertically aligned. An example of the radiation impedance is shown in Figure 2.2.

In MTL, the radiation impedance can be seen by the return current as a per-unit-length ground resistance and inductance. Therefore, the original structure can be separated into three segments, including two ideal transmission line segments and one with additional return impedance, as shown in Figure 2.3.

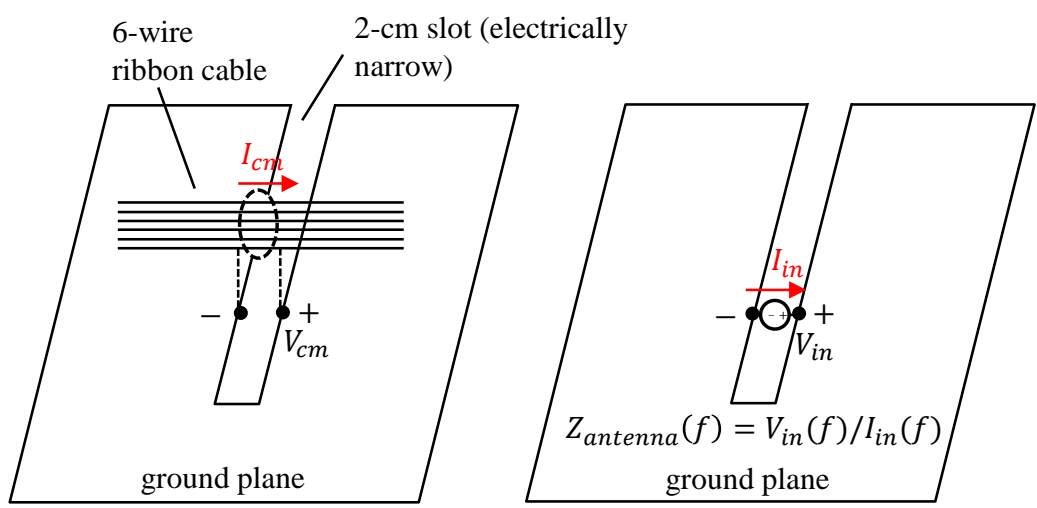


Figure 2.1. Equivalence and Extraction of the Antenna Impedance

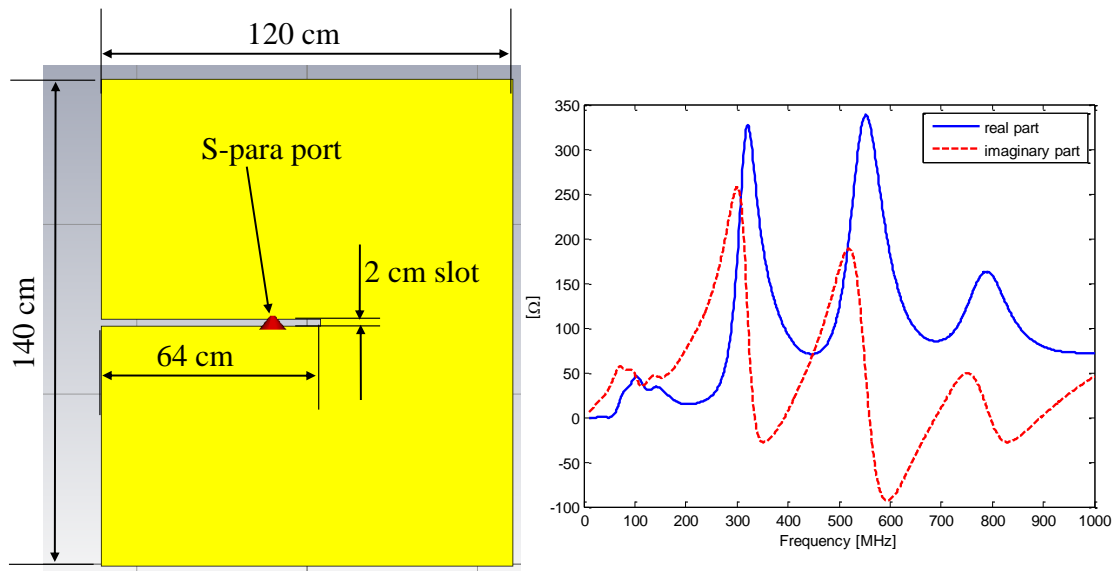


Figure 2.2. Real and Imaginary Part of the Radiation Impedance

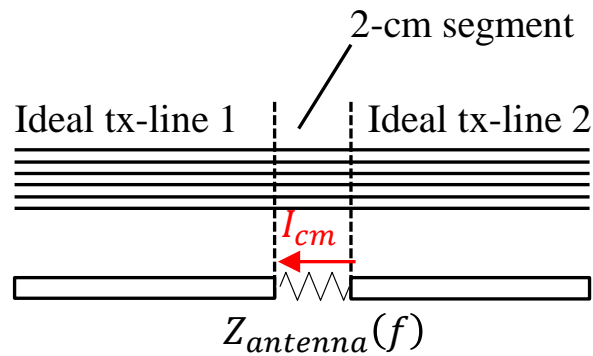


Figure 2.3. Incorporate MTL with Equivalent Radiation Impedance

The first transmission line equation can be derived by writing KVL around a small segment of Δz , as shown in Figure 2.4.

$$v(z,t) - v(z + \Delta z, t) = R\Delta z i(z,t) + L\Delta z \frac{\partial i(z,t)}{\partial t} \quad (2)$$

Take the limit as $\Delta z \rightarrow 0$, and in frequency domain

$$\begin{aligned} \frac{v(z,t) - v(z + \Delta z, t)}{\Delta z} &= Ri(z,t) + L \frac{\partial i(z,t)}{\partial t} \\ \rightarrow \frac{dV(z)}{dz} &= -(R + j\omega L)I(z) \end{aligned} \quad (3)$$

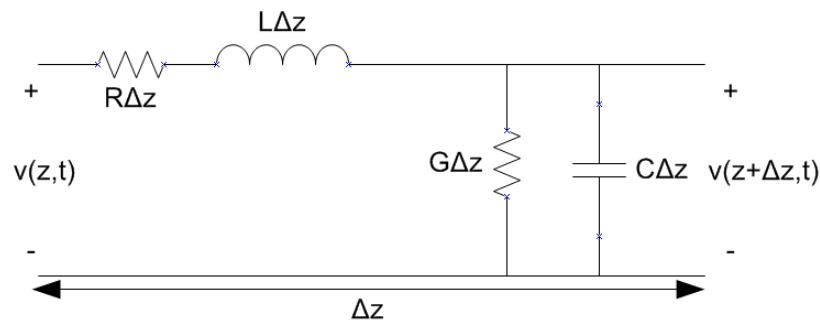


Figure 2.4. Writing KVL around the Small Segment Δz

Similar ideas can be expanded into multi-conductor transmission line with ground impedance. Write KVL for transmission line #1, as shown in Figure 2.5, one could get

$$\begin{aligned}
 V_1(z) - V_1(z + \Delta z) = & R_1 \Delta z I_1(z) \\
 & + [R_0 \Delta z (I_1(z) + I_2(z) + \dots + I_6(z))] \\
 & + [j\omega L_{11} \Delta z I_1(z) + j\omega L_{12} \Delta z I_2(z) + \dots + j\omega L_{16} \Delta z I_6(z)] \\
 & + [j\omega L_0 \Delta z (I_1(z) + I_2(z) + \dots + I_6(z))]
 \end{aligned} \tag{4}$$

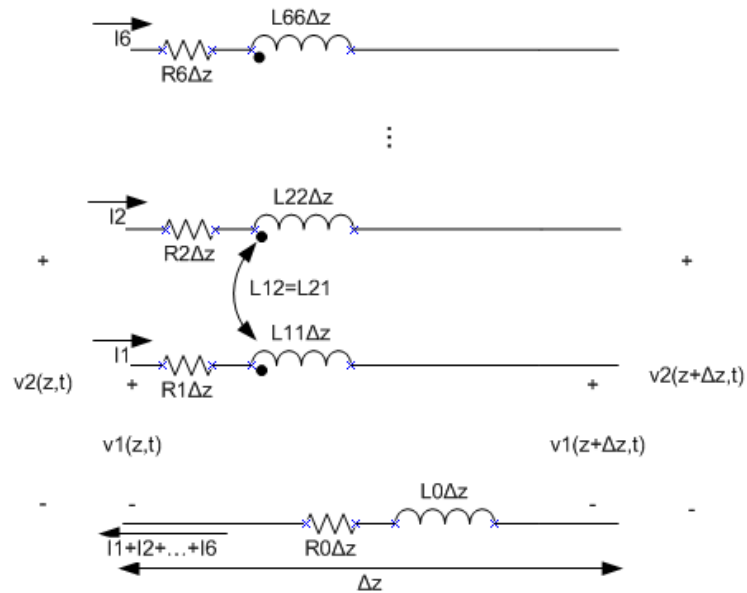


Figure 2.5. MTL With Ground Impedance In The Current Return Path

Write KVL for other wires, and rearrange in a matrix form as shown in (5), we could see that the ground impedance in the return path can be easily added to the original PUL R and L matrix of ideal transmission line.

$$\begin{bmatrix} dV_1(z)/dz \\ dV_2(z)/dz \\ \vdots \\ \vdots \\ dV_6(z)/dz \end{bmatrix} = - \begin{bmatrix} R_{11} + R_0 & R_{12} + R_0 & R_{13} + R_0 & R_{14} + R_0 & R_{15} + R_0 & R_{16} + R_0 \\ R_{21} + R_0 & R_{22} + R_0 & & & & \\ \vdots & & R_{33} + R_0 & & & \\ R_{41} + R_0 & & & R_{44} + R_0 & & \\ \vdots & & & & R_{55} + R_0 & \\ R_{61} + R_0 & \dots & \dots & \dots & \dots & R_{66} + R_0 \end{bmatrix} \begin{bmatrix} I_1(z) \\ I_2(z) \\ \vdots \\ \vdots \\ I_6(z) \end{bmatrix} \quad (5)$$

$$-j\omega \begin{bmatrix} L_{11} + L_0 & L_{12} + L_0 & L_{13} + L_0 & L_{14} + L_0 & L_{15} + L_0 & L_{16} + L_0 \\ L_{21} + L_0 & L_{22} + L_0 & & & & \\ L_{31} + L_0 & & L_{33} + L_0 & & & \\ L_{41} + L_0 & & & L_{44} + L_0 & & \\ L_{51} + L_0 & & & & L_{55} + L_0 & \\ L_{61} + L_0 & \dots & \dots & \dots & \dots & L_{66} + L_0 \end{bmatrix} \begin{bmatrix} I_1(z) \\ I_2(z) \\ \vdots \\ \vdots \\ I_6(z) \end{bmatrix}$$

where,

$$\begin{aligned} R_0 &= \text{Re}\{Z_{\text{antenna}}\} / (\text{segment length}) \\ L_0 &= \text{Im}\{Z_{\text{antenna}}\} / \omega / (\text{segment length}) \end{aligned} \quad (6)$$

S-parameters of this 3-segment transmission line with the modified PUL RLGC parameters can be solved by the chain parameters approach [29], and the results is shown in Figure 2.6.

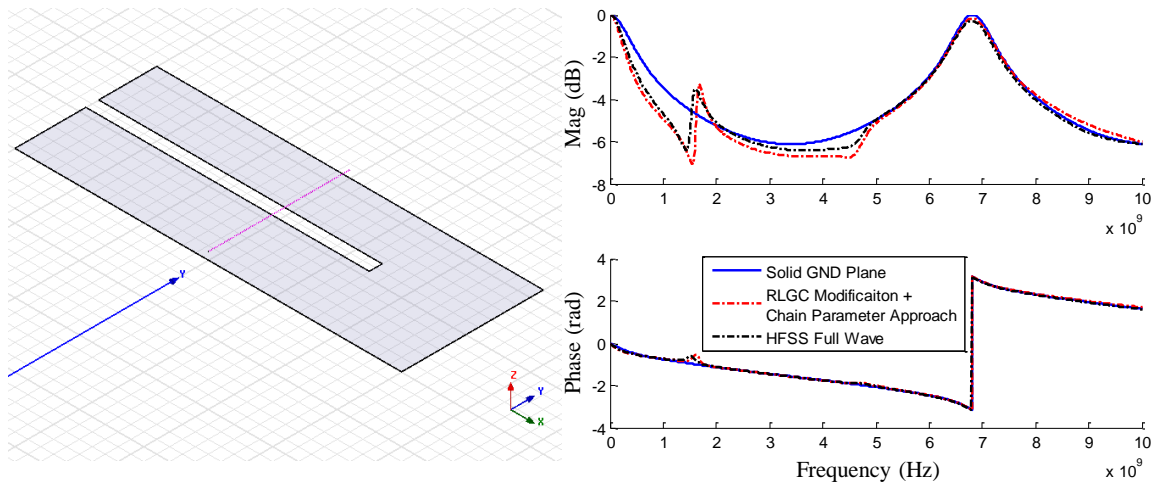


Figure 2.6. S-parameters Comparison from Different Approaches

When multiple bundles across one gap problem is analyzed, if the bundles are far away from each other, i.e. the mutual effect between each bundle can be neglected, the proposed RLGC modification method could be extended here. Similar equivalent radiation impedance can be obtained by full wave simulation, except we have two ports defined beneath the two bundles now, as shown in Figure 2.7.

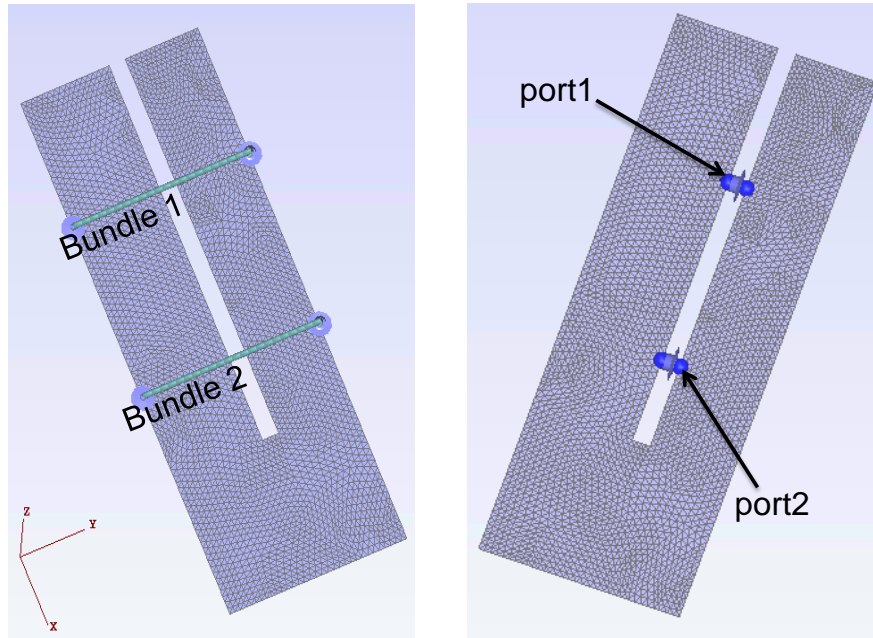


Figure 2.7. Equivalent Radiation Impedance Could Be Considered as a Two-Port Network

Again writing KVL for Wire #1 within Bundle #1 in Figure 2.8 gives,

$$\begin{aligned}
 V_1(z) - V_1(z + \Delta z) = & R_{11} \Delta z I_1(z) + j\omega L_{11} \Delta z I_1(z) \quad \left. \vphantom{R_{11} \Delta z I_1(z)} \right\} : \text{Self Term} \\
 & + j\omega L_{12} \Delta z I_2(z) \\
 & + j\omega L_{13} \Delta z I_3(z) \\
 & + j\omega L_{14} \Delta z I_4(z) \\
 & + j\omega L_{15} \Delta z I_5(z) \quad \left. \vphantom{j\omega L_{12} \Delta z I_2(z)} \right\} : \text{Mutual Term} \\
 & + [Z_{11} (I_1(z) + I_2(z) + I_3(z)) \\
 & + Z_{12} (I_4(z) + I_5(z))] \quad \left. \vphantom{Z_{11} (I_1(z) + I_2(z) + I_3(z))} \right\} : \text{GND Term}
 \end{aligned} \tag{7}$$

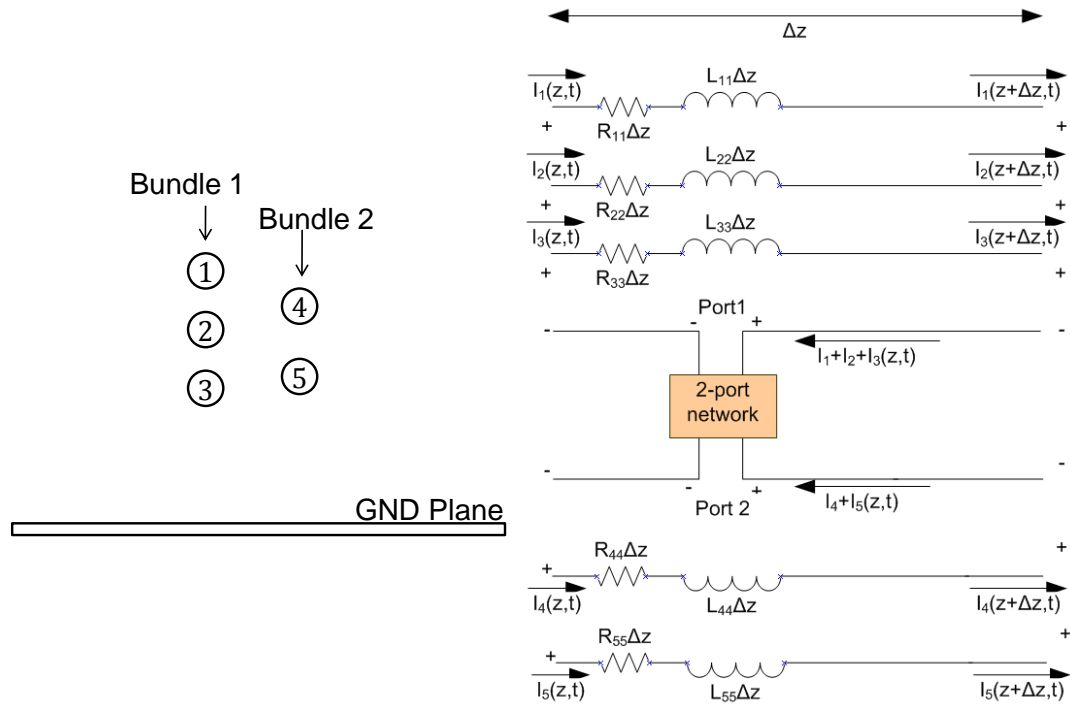


Figure 2.8. Equivalent Circuit Network of Multiple Bundles in Small Segment of Δz

Notice the original PUL \mathbf{R} and \mathbf{L} matrices are given as

$$\mathbf{R} = \begin{bmatrix} R_{11} & & & & & \\ & R_{22} & & & & \\ & & R_{33} & & & \\ & & & R_{44} & & \\ & & & & R_{55} & \\ & & & & & \end{bmatrix}, \mathbf{L} = \begin{bmatrix} L_{11} & L_{12} & L_{13} & L_{14} & L_{15} \\ L_{21} & L_{22} & L_{23} & L_{24} & L_{25} \\ L_{31} & L_{32} & L_{33} & L_{34} & L_{35} \\ L_{41} & L_{42} & L_{43} & L_{44} & L_{45} \\ L_{51} & L_{52} & L_{53} & L_{54} & L_{55} \end{bmatrix} \quad (8)$$

Write KVL for other wires and rearrange the terms into a sub-matrix notation, we could get the modification for the PUL \mathbf{R} matrix.

$$\mathbf{R}' = \begin{bmatrix} \mathbf{R}_{B11} + \frac{\text{Re}\{Z_{11}\}}{len} & \mathbf{R}_{B12} + \frac{\text{Re}\{Z_{12}\}}{len} \\ \mathbf{R}_{B21} + \frac{\text{Re}\{Z_{21}\}}{len} & \mathbf{R}_{B22} + \frac{\text{Re}\{Z_{22}\}}{len} \end{bmatrix} \quad (9)$$

where,

$$\mathbf{R} = \begin{bmatrix} R_{11} & & & & \\ & R_{22} & & & \\ & & R_{22} & & \\ & & & R_{22} & \\ & & & & R_{22} \end{bmatrix} = \begin{bmatrix} \mathbf{R}_{B11} & \mathbf{R}_{B12} \\ \mathbf{R}_{B21} & \mathbf{R}_{B22} \end{bmatrix} \quad (10)$$

$$\mathbf{R}_{B11} = \begin{bmatrix} R_{11} & & \\ & R_{22} & \\ & & R_{33} \end{bmatrix}, \mathbf{R}_{B12} = \begin{bmatrix} 0 & 0 \\ 0 & 0 \\ 0 & 0 \end{bmatrix}, \quad (11)$$

$$\mathbf{R}_{B21} = \begin{bmatrix} 0 & 0 & 0 \\ 0 & 0 & 0 \end{bmatrix}, \mathbf{R}_{B22} = \begin{bmatrix} R_{44} & \\ & R_{55} \end{bmatrix}$$

Similarly, the modified PUL \mathbf{L} matrix becomes

$$\mathbf{L}' = \begin{bmatrix} \mathbf{L}_{B11} + \frac{\text{Im}\{Z_{11}\}}{\text{len} * \omega} & \mathbf{L}_{B12} + \frac{\text{Im}\{Z_{12}\}}{\text{len} * \omega} \\ \mathbf{L}_{B21} + \frac{\text{Im}\{Z_{21}\}}{\text{len} * \omega} & \mathbf{L}_{B22} + \frac{\text{Im}\{Z_{22}\}}{\text{len} * \omega} \end{bmatrix} \quad (12)$$

where,

$$\mathbf{L} = \begin{bmatrix} L_{11} & L_{12} & L_{13} & L_{14} & L_{15} \\ L_{21} & L_{22} & L_{23} & L_{24} & L_{25} \\ L_{31} & L_{32} & L_{33} & L_{34} & L_{35} \\ L_{41} & L_{42} & L_{43} & L_{44} & L_{45} \\ L_{51} & L_{52} & L_{53} & L_{54} & L_{55} \end{bmatrix} = \begin{bmatrix} \mathbf{L}_{B11} & \mathbf{L}_{B12} \\ \mathbf{L}_{B21} & \mathbf{L}_{B22} \end{bmatrix} \quad (13)$$

$$\mathbf{L}_{B11} = \begin{bmatrix} L_{11} & L_{12} & L_{13} \\ L_{21} & L_{22} & L_{23} \\ L_{31} & L_{32} & L_{33} \end{bmatrix}, \mathbf{L}_{B12} = \begin{bmatrix} L_{14} & L_{15} \\ L_{24} & L_{25} \\ L_{34} & L_{35} \end{bmatrix}, \quad (14)$$

$$\mathbf{L}_{B21} = \begin{bmatrix} L_{41} & L_{42} & L_{43} \\ L_{51} & L_{52} & L_{53} \end{bmatrix}, \mathbf{L}_{B22} = \begin{bmatrix} L_{44} & L_{45} \\ L_{54} & L_{55} \end{bmatrix}$$

S-parameters of this 3-segment multi-bundle transmission line with the modified PUL RLGC parameters can be again solved by the chain parameters approach, and the results are shown in Figure 2.9.

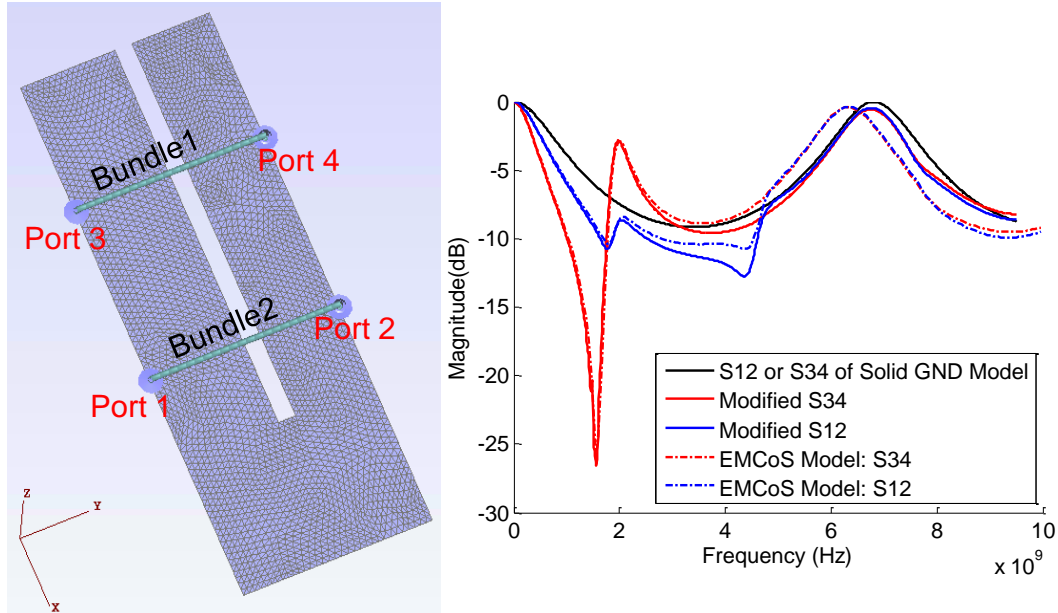


Figure 2.9. S-parameters Comparison from Different Approaches for Multi-Bundle Transmission Line

2.3. METHOD OF MOMENT

When dealing with complex cable and environment structures, the engineering solution is not any more valid. The full wave Method of Moment (MoM) is used for accurate analysis of EMI and radiation analysis.

2.3.1. EFIE with RWG Basis Functions. The electric field in the vicinity of conductor is the summation of incident field and scattered field. The conductor can be completely replaced by the equivalent surface current density $\vec{J}(\vec{r}')$ and surface charge density $\sigma(\vec{r}')$. The scattered electric field can be written as

$$\vec{E}^{sct}(\vec{r}) = -j\omega\vec{A}(\vec{r}) - \nabla\phi(\vec{r}) \quad (15)$$

where \vec{A} is the vector magnetic potential, and ϕ is the scalar electric potential.

$$\vec{A}(\vec{r}) = \mu \int_{S'} \vec{G}^A(\vec{r}, \vec{r}') \vec{J}(\vec{r}') ds' \quad (16)$$

$$\phi(\vec{r}) = \frac{1}{\epsilon} \int_{S'} G^\phi(\vec{r}, \vec{r}') \sigma(\vec{r}') ds' \quad (17)$$

$\overline{\overline{G}}^A(\vec{r}, \vec{r}')$ is the dyadic Green's function for the vector magnetic potential \vec{A} and $G^\phi(\vec{r}, \vec{r}')$ is the Green's function for scalar electric potential ϕ . In free space, both $\overline{\overline{G}}^A(\vec{r}, \vec{r}')$ and $G^\phi(\vec{r}, \vec{r}')$ can be defined as

$$G_0(\vec{r}, \vec{r}') = \frac{e^{-jk|\vec{r}-\vec{r}'|}}{4\pi|\vec{r}-\vec{r}'|}, k = \omega\sqrt{\epsilon_0\mu_0} \quad (18)$$

The total electric field (incident \vec{E}^{inc} + scattered \vec{E}^{sct}) has to satisfy the boundary condition on the wire surface S. For PEC boundary condition,

$$\hat{n} \times [\vec{E}^{inc}(\vec{r}) + \vec{E}^{sct}(\vec{r})] = 0 \quad (19)$$

Substitute (15) into (19), we have,

$$\hat{n} \times \left[-j\omega\mu \int_{S'} \overline{\overline{G}}^A(\vec{r}, \vec{r}') \vec{J}(\vec{r}') ds' - \frac{1}{\epsilon} \nabla \int_{S'} G^\phi(\vec{r}, \vec{r}') \sigma(\vec{r}') ds' \right] = -\hat{n} \times \vec{E}^{inc}(\vec{r}) \quad (20)$$

which is known as Mixed Potential Integral Equation (**MPIE**), since two unknowns, $\vec{J}(\vec{r}')$ (related to \vec{A}) and $\sigma(\vec{r}')$ (related to ϕ) are mixed together.

Surface current density $\vec{J}(\vec{r}')$ and surface charge density $\sigma(\vec{r}')$ can be related by the continuity equation.

$$\nabla'_{s'} \cdot \vec{J}(\vec{r}') = -j\omega\sigma(\vec{r}') \quad (21)$$

Substitution of (21) into (20) leads to

$$\hat{n} \times \left[-j\omega\mu \int_{S'} \vec{J}(\vec{r}') \overline{\overline{G}}^A(\vec{r}, \vec{r}') ds' - \frac{j}{\epsilon\omega} \nabla \int_{S'} \nabla'_{s'} \cdot \vec{J}(\vec{r}') G^\phi(\vec{r}, \vec{r}') ds' \right] = -\hat{n} \times \vec{E}^{inc} \quad (22)$$

which is the Electric Field Integral Equation (**EFIE**), where the only unknown is $\vec{J}(\vec{r}')$.

The surface scatter are meshed by triangles (as shown in Figure 2.10), and the classic Rao-Wilton-Gilsson (RWG) basis function (as shown in Figure 2.11) is used to expand the unknown induced current density $\vec{J}(\vec{r}')$ as

$$\vec{J}(\vec{r}') = \sum_{n=1}^M J_n \vec{f}_n(\vec{r}') \quad (23)$$

where M is truncation number (the total number of basis functions), J_n is the unknown coefficient, and $\vec{f}_n(\vec{r}')$ is the basis function.

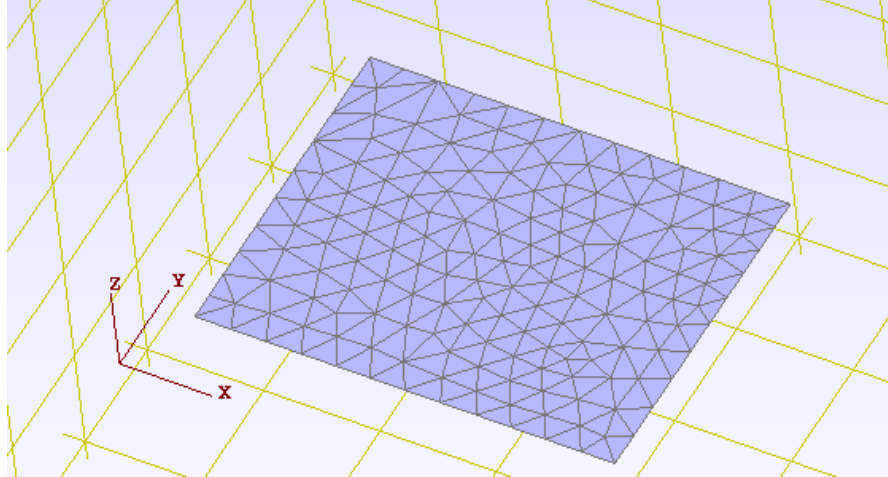


Figure 2.10. Discretization of Surface Structure by Triangles

For the n^{th} interior edge, it uniquely defines two adjacent triangular cells T_n^+ and T_n^- . Their corresponding areas are A_n^+ and A_n^- , respectively. The n^{th} RWG basis function (that is associated with the n^{th} edge) is defined as,

$$\vec{f}_n(\vec{r}) = \begin{cases} \frac{1}{h_n^+} (\vec{r} - \vec{r}_n^+) = \frac{\vec{\rho}_n^+}{h_n^+}, & \vec{r} \in T_n^+ \\ -\frac{1}{h_n^-} (\vec{r} - \vec{r}_n^-) = \frac{\vec{\rho}_n^-}{h_n^-}, & \vec{r} \in T_n^- \\ 0, & \text{elsewhere} \end{cases} \quad (24)$$

where,

$$h_n^+ = \frac{2A_n^+}{l_n}, h_n^- = \frac{2A_n^-}{l_n}, \vec{\rho}_n^+ = \vec{r} - \vec{r}_n^+, \vec{\rho}_n^- = \vec{r}_n^- - \vec{r} \quad (25)$$

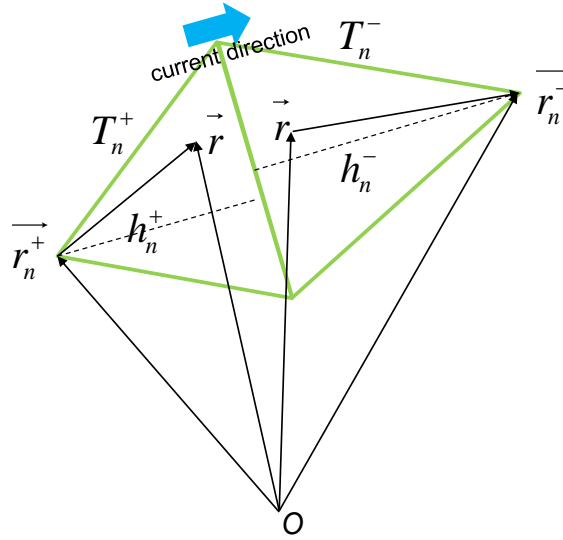


Figure 2.11. RWG Basis Function Illustration

Some important properties of the RWG basis functions are:

1. The basis function is defined at an interior edge. At any boundary edge, current is zero, so no need to define a basis function there.
2. The component normal to the edge direction l_n is unity everywhere on the edge, which means the current normal to the edge is continuous.
3. In a local polar system,

$$\nabla_s \cdot \vec{f}_n(\vec{r}) = \frac{\pm 1}{\rho_n^\pm} \frac{\partial}{\partial \rho_n^\pm} (\rho_n^\pm f_n) = \begin{cases} \frac{l_n}{A_n^+}, & \vec{r} \in T_n^+ \\ -\frac{l_n}{A_n^-}, & \vec{r} \in T_n^- \\ 0, & \text{elsewhere} \end{cases} \quad (26)$$

Substitute (23) into (22) with the expansion, and test the equation with the same basis function (Galerkin's method) by inner product,

$$\begin{aligned} & \left\langle \vec{f}_m(\vec{r}), j\omega\mu \sum_{n=1}^M J_n \int_{S'} \vec{G}^A(\vec{r}, \vec{r}') \vec{f}_n(\vec{r}') ds' \right\rangle \\ & + \left\langle \vec{f}_m(\vec{r}), \frac{j}{\epsilon\omega} \sum_{n=1}^M J_n \nabla \int_{S'} G^\phi(\vec{r}, \vec{r}') \nabla_{s'} \cdot \vec{f}_n(\vec{r}') ds' \right\rangle = \left\langle \vec{f}_m(\vec{r}), \vec{E}^{inc}(\vec{r}) \right\rangle \end{aligned} \quad (27)$$

where since the basis function is defined on the surface, the volume dot product was replaced by the surface dot product, and the inner product is defined **on surface** as,

$$\langle \vec{f}, \vec{g} \rangle \triangleq \int_S \vec{f} \cdot \vec{g} \, ds \quad (28)$$

The first term in the LHS of (27) is

$$\begin{aligned} \text{1st term in LHS} &= j\omega\mu \sum_{n=1}^M J_n \left\langle \vec{f}_m(\vec{r}), \int_S \vec{G}^{\overline{\overline{A}}}(\vec{r}, \vec{r}') \vec{f}_n(\vec{r}') ds' \right\rangle \\ &= j\omega\mu \sum_{n=1}^M J_n \left\langle \vec{f}_m(\vec{r}), \int_{T_n^+ + T_n^-} \vec{G}^{\overline{\overline{A}}}(\vec{r}, \vec{r}') \vec{f}_n(\vec{r}') ds' \right\rangle \\ &= j\omega\mu \sum_{n=1}^M J_n \int_{T_m^+ + T_m^-} \int_{T_n^+ + T_n^-} \vec{G}^{\overline{\overline{A}}}(\vec{r}, \vec{r}') \vec{f}_m(\vec{r}) \cdot \vec{f}_n(\vec{r}') ds' ds \\ &= j\omega\mu \sum_{n=1}^M J_n \left\{ \int_{T_m^+} \int_{T_n^+} \frac{l_m}{2A_m^+} \frac{l_n}{2A_n^+} (\vec{r} - \vec{r}_m^+) \cdot (\vec{r}' - \vec{r}_n^+) \vec{G}^{\overline{\overline{A}}}(\vec{r}, \vec{r}') ds' ds \right. \\ &\quad - \int_{T_m^+} \int_{T_n^-} \frac{l_m}{2A_m^+} \frac{l_n}{2A_n^-} (\vec{r} - \vec{r}_m^+) \cdot (\vec{r}' - \vec{r}_n^-) \vec{G}^{\overline{\overline{A}}}(\vec{r}, \vec{r}') ds' ds \\ &\quad - \int_{T_m^-} \int_{T_n^+} \frac{l_m}{2A_m^-} \frac{l_n}{2A_n^+} (\vec{r} - \vec{r}_m^-) \cdot (\vec{r}' - \vec{r}_n^+) \vec{G}^{\overline{\overline{A}}}(\vec{r}, \vec{r}') ds' ds \\ &\quad \left. + \int_{T_m^-} \int_{T_n^-} \frac{l_m}{2A_m^-} \frac{l_n}{2A_n^-} (\vec{r} - \vec{r}_m^-) \cdot (\vec{r}' - \vec{r}_n^-) \vec{G}^{\overline{\overline{A}}}(\vec{r}, \vec{r}') ds' ds \right\} \\ &= j\omega\mu \sum_{n=1}^M J_n \frac{l_m l_n}{4} (M_{m+n+} - M_{m+n-} - M_{m-n+} + M_{m-n-}) \end{aligned} \quad (29)$$

where,

$$M_{pq} = \frac{1}{A_p A_q} \int_{T_p} \int_{T_q} (\vec{r} - \vec{r}_p) \cdot (\vec{r}' - \vec{r}_q) \vec{G}^{\overline{\overline{A}}}(\vec{r}, \vec{r}') ds' ds \quad (30)$$

The second term in the LHS of (27) is

$$\text{2nd term in LHS} = \frac{1}{j\omega\epsilon} \sum_{n=1}^M J_n l_m l_n (W_{m+n+} - W_{m+n-} - W_{m-n+} + W_{m-n-}) \quad (31)$$

where,

$$W_{pq} = \frac{1}{A_p A_q} \int_{T_p} \int_{T_q} G^\phi(\vec{r}, \vec{r}') ds' ds \quad (32)$$

Then (27) can be written in the matrix representation,

$$\begin{bmatrix} Z_{11} & Z_{12} & \cdots & Z_{1M} \\ Z_{21} & Z_{22} & \cdots & Z_{2M} \\ \vdots & \vdots & \ddots & \vdots \\ Z_{M1} & Z_{M2} & \cdots & Z_{MM} \end{bmatrix} \begin{bmatrix} J_1 \\ J_2 \\ \vdots \\ J_M \end{bmatrix} = \begin{bmatrix} V_1 \\ V_2 \\ \vdots \\ V_M \end{bmatrix} \quad (33)$$

where,

$$\begin{aligned}
Z_{mm} &= j\omega\mu \frac{l_m l_n}{4} (M_{m+n+} - M_{m+n-} - M_{m-n+} + M_{m-n-}) \\
&\quad + \frac{1}{j\omega\epsilon} l_m l_n (W_{m+n+} - W_{m+n-} - W_{m-n+} + W_{m-n-})
\end{aligned} \tag{34}$$

$$\begin{aligned}
V_m &= \left\langle \vec{f}_m(\vec{r}), \vec{E}^{\text{inc}}(\vec{r}) \right\rangle \\
&= \int_{T_m^+ + T_m^-} \vec{f}_m(\vec{r}) \cdot \vec{E}^{\text{inc}}(\vec{r}) ds \\
&= \int_{T_m^+} \frac{l_m}{2A_m^+} (\vec{r} - \vec{r}_m^+) \cdot \vec{E}^{\text{inc}}(\vec{r}) ds + \int_{T_m^-} \frac{-l_m}{2A_m^-} (\vec{r} - \vec{r}_m^-) \cdot \vec{E}^{\text{inc}}(\vec{r}) ds \\
&= \frac{l_m}{2} \left[\frac{1}{A_m^+} \int_{T_m^+} (\vec{r} - \vec{r}_m^+) \cdot \vec{E}^{\text{inc}}(\vec{r}) ds - \frac{1}{A_m^-} \int_{T_m^-} (\vec{r} - \vec{r}_m^-) \cdot \vec{E}^{\text{inc}}(\vec{r}) ds \right]
\end{aligned} \tag{35}$$

2.3.2. Scattered Field by Induced Surface Current Density. The induced current density represented as RWG basis coefficients J_n in (27) generates scattered field as in (15). Rewrite the equation here as

$$\begin{aligned}
\vec{E}^{\text{sct}}(\vec{r}) &= -j\omega\mu \sum_{n=1}^M J_n \int_{S_n'} \vec{G}^{\text{A}}(\vec{r}, \vec{r}') \vec{f}_n(\vec{r}') ds' \\
&\quad - \frac{j}{\omega\epsilon} \sum_{n=1}^M J_n \nabla \int_{S_n'} G^\phi(\vec{r}, \vec{r}') \nabla_{S'} \cdot \vec{f}_n(\vec{r}') ds'
\end{aligned} \tag{36}$$

By taking advantage of (24), the first integral is

$$\begin{aligned}
I_{1n} &= \int_{S_n'} \vec{G}^{\text{A}}(\vec{r}, \vec{r}') \vec{f}_n(\vec{r}') ds' \\
&= \int_{T_n^+ + T_n^-} \vec{f}_n(\vec{r}') G_0(\vec{r}, \vec{r}') ds \\
&= \int_{T_n^+} \frac{l_n}{2A_n^+} (\vec{r}' - \vec{r}_n^+) G_0(\vec{r}, \vec{r}') ds + \int_{T_n^-} \frac{-l_n}{2A_n^-} (\vec{r}' - \vec{r}_n^-) G_0(\vec{r}, \vec{r}') ds \\
&= A_n^+ \sum_{i=1}^{N^{2D}} \omega_i^{2D} \frac{l_n}{2A_n^+} (\vec{r}'_i - \vec{r}_n^+) G_0(\vec{r}, \vec{r}'_i) + A_n^- \sum_{i=1}^{N^{2D}} \omega_i^{2D} \frac{-l_n}{2A_n^-} (\vec{r}'_i - \vec{r}_n^-) G_0(\vec{r}, \vec{r}'_i) \\
&= \frac{l_n}{2} \left[\sum_{i=1}^{N^{2D}} \omega_i^{2D} (\vec{r}'_i - \vec{r}_n^+) G_0(\vec{r}, \vec{r}'_i) - \sum_{i=1}^{N^{2D}} \omega_i^{2D} (\vec{r}'_i - \vec{r}_n^-) G_0(\vec{r}, \vec{r}'_i) \right]
\end{aligned} \tag{37}$$

where N^{2D} is the number of Gaussian Quadrature Integral points, ω_i^{2D} is the Gaussian Quadrature Integral coefficients, and l_n is the length of n-th interior edge.

By taking advantage of (26), the second integral with gradient becomes

$$\begin{aligned}
I_{2n} &= \nabla \int_{S'_n} G^\phi(\vec{r}, \vec{r}') \nabla'_{s'} \cdot \vec{f}_n(\vec{r}') ds' \\
&= \int_{T_n^+ + T_n^-} \nabla G_0(\vec{r}, \vec{r}') \nabla'_{s'} \cdot \vec{f}_n(\vec{r}') ds \\
&= \int_{T_n^+} \frac{l_n}{A_n^+} \nabla G_0(\vec{r}, \vec{r}') ds + \int_{T_n^-} \frac{-l_n}{A_n^-} \nabla G_0(\vec{r}, \vec{r}') ds \\
&= A_n^+ \sum_{i=1}^{N^{2D}} \omega_i^{2D} \frac{l_n}{A_n^+} \nabla G_0(\vec{r}, \vec{r}'_i) + A_n^- \sum_{i=1}^{N^{2D}} \omega_i^{2D} \frac{-l_n}{A_n^-} \nabla G_0(\vec{r}, \vec{r}'_i) \\
&= l_n \left[\sum_{i=1}^{N^{2D}} \omega_i^{2D} \nabla G_0(\vec{r}, \vec{r}'_i) - \sum_{i=1}^{N^{2D}} \omega_i^{2D} \nabla G_0(\vec{r}, \vec{r}'_i) \right]
\end{aligned} \tag{38}$$

where the gradient ∇ applies on r rather than r' . That the gradient ∇ can be moved inside the integral onto $G_0(\vec{r}, \vec{r}')$ is because only $G_0(\vec{r}, \vec{r}')$ is a function of r . The Green's function is again written as

$$G_0(\vec{r}, \vec{r}') = \frac{e^{-jkR}}{4\pi R} \tag{39}$$

and its gradient is

$$\nabla G_0(\vec{r}, \vec{r}') = -\hat{R} \left(jk + \frac{1}{R} \right) G_0(\vec{r}, \vec{r}') = -\hat{R} \left(jk + \frac{1}{R} \right) \frac{e^{-jkR}}{4\pi R} \tag{40}$$

where $R = |\vec{r} - \vec{r}'|$, and $\hat{R} = (\vec{r} - \vec{r}') / R$. The observation point \vec{r} is usually distant away from the surface structure, and therefore no singularity issue should be considered.

The final equation for scattered E-field is just

$$\vec{E}^{sct}(\vec{r}) = -\sum_{n=1}^M J_n \left(j\omega\mu I_{1n} + \frac{j}{\omega\epsilon} I_{2n} \right) \tag{41}$$

2.3.3. Arbitrary Thin Wire (ATW) Approximation. The EFIE formulation for thin wire structure is shown below.

$$\hat{n} \times \left[-j\omega\mu \int_{S'} \vec{J}(\vec{r}') \vec{G}^A(\vec{r}, \vec{r}') ds' - \frac{j}{\omega\epsilon} \nabla \int_{S'} \nabla'_{s'} \cdot \vec{J}(\vec{r}') G^\phi(\vec{r}, \vec{r}') ds' \right] = -\hat{n} \times \vec{E}^{inc}(\vec{r}) \tag{42}$$

The surface current density $\vec{J}(\vec{r}')$ is defined on the surface of thin wire structure.

Since the wire is assumed very thin, only axial direction of $\vec{J}(\vec{r}')$ is considered. The cross-sectional distribution of current density $\vec{J}(\vec{r}')$ is simple (uniformly distributed

around the circular wire surface) and can be written in terms of a filamentary current $I_z(\vec{r}')$ oriented to the thin wire direction,

$$\vec{J}(\vec{r}') = \frac{\vec{I}(\vec{r}')}{2\pi a} = \frac{I_z(z')}{2\pi a} \hat{z} \quad (43)$$

where a is the radius of the thin wire, \hat{z} is the axial direction of local coordinate, and $\vec{J}(\vec{r}')$ is not dependent on wire azimuthal angle. The filamentary current $I_z(\vec{r}')$ can be expanded as 1-D rooftop basis functions.

$$\vec{I}(\vec{r}') = \sum_{n=1}^M I_n \vec{f}_n(\vec{r}') \quad (44)$$

When there is no current flowing at two ends of the thin wire (end condition 1), the rooftop basis function is defined on each interior edge (1-D edge), as shown in Figure 2.12. When there is current flowing at two ends (end condition 2), two more half basis functions are defined on the boundary edge (1-D edge) [73], as shown in Figure 2.13.

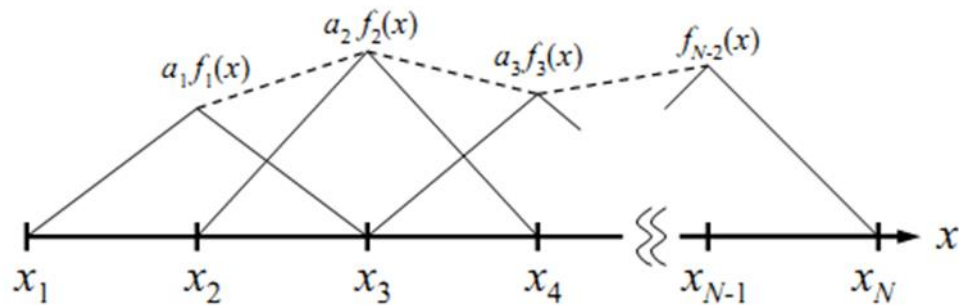


Figure 2.12. Rooftop Basis Functions (End Condition 1)

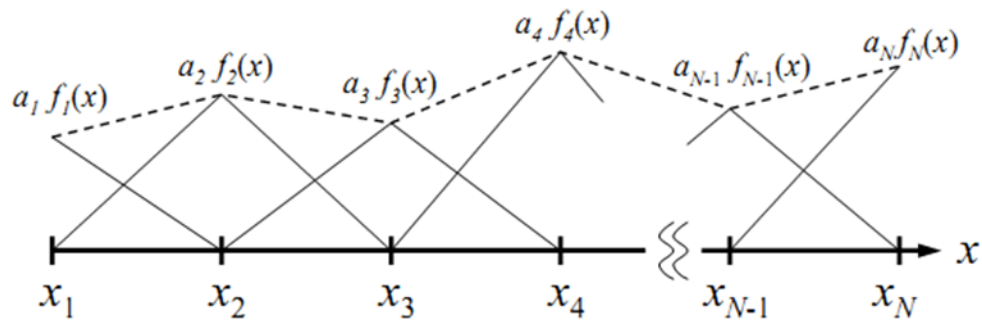


Figure 2.13. Rooftop Basis Functions (End Condition 2)

For n^{th} interior edge, it uniquely defines two adjacent line cells L_n^+ and L_n^- . Their corresponding lengths are l_n^+ and l_n^- , and their corresponding surface areas are $A_n^+ = 2\pi a l_n^+$ and $A_n^- = 2\pi a l_n^-$, respectively. As shown in Figure 2.14, the n^{th} rooftop basis function defined on the n^{th} interior edge is

$$\vec{f}_n(\vec{r}) = \begin{cases} \frac{1}{l_n^+}(\vec{r} - \vec{r}_n^+) = \frac{\vec{\rho}_n^+}{l_n^+}, & \vec{r} \in L_n^+ \\ -\frac{1}{l_n^-}(\vec{r} - \vec{r}_n^-) = \frac{\vec{\rho}_n^-}{l_n^-}, & \vec{r} \in L_n^- \\ 0, & \text{elsewhere} \end{cases} \quad (45)$$

where,

$$\vec{\rho}_n^+ = \vec{r} - \vec{r}_n^+, \vec{\rho}_n^- = \vec{r}_n^- - \vec{r} \quad (46)$$

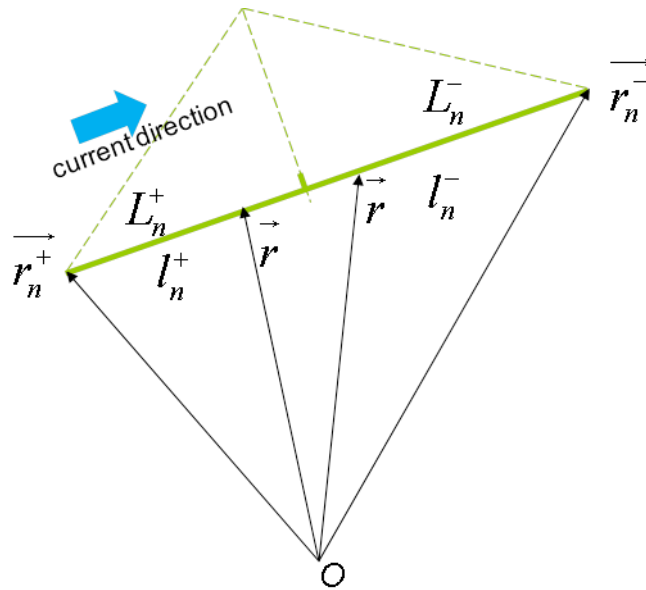


Figure 2.14. Rooftop Basis Function for Thin Wire Approximation

The current density $\vec{J}(\vec{r}')$ on the thin wire surface is written as

$$\vec{J}(\vec{r}') = \frac{1}{2\pi a} \sum_{n=1}^M I_n \vec{f}_n(\vec{r}') \quad (47)$$

Substitute (47) into (42) with the expansion, and test the equation with the same basis function (Galerkin's method) by inner product,

$$\begin{aligned} & \left\langle \vec{f}_m(\vec{r}), j\omega\mu \sum_{n=1}^M \frac{I_n}{2\pi a} \int_{S'} \vec{G}^{\overline{\overline{A}}}(\vec{r}, \vec{r}') \vec{f}_n(\vec{r}') ds' \right\rangle \\ & + \left\langle \vec{f}_m(\vec{r}), \frac{j}{\varepsilon\omega} \sum_{n=1}^M \frac{I_n}{2\pi a} \nabla \int_{S'} G^\phi(\vec{r}, \vec{r}') \nabla_{S'} \cdot \vec{f}_n(\vec{r}') ds' \right\rangle = \left\langle \vec{f}_m(\vec{r}), \vec{E}^{inc}(\vec{r}) \right\rangle \end{aligned} \quad (48)$$

where because of the 1-D rooftop basis, the inner product is defined in **1-D** as,

$$\langle \vec{f}, \vec{g} \rangle \triangleq \int_S \vec{f} \cdot \vec{g} dl \quad (49)$$

Due to the thin wire approximation, in the reduced kernel [73], [74], source point is on the surface of the thin wire, while the testing point is on the axial. Similarly as the surface structure, the first term in the LHS of (48) is

$$\begin{aligned} \text{1st term in LHS} &= j\omega\mu \sum_{n=1}^M \frac{I_n}{2\pi a} \left\langle \vec{f}_m(\vec{r}), \int_{S'} \vec{G}^{\overline{\overline{A}}}(\vec{r}, \vec{r}') \vec{f}_n(\vec{r}') ds' \right\rangle \\ &= j\omega\mu \sum_{n=1}^M \frac{I_n}{2\pi a} \left\langle \vec{f}_m(\vec{r}), \int_{L_m^+ L_n^+} \vec{G}^{\overline{\overline{A}}}(\vec{r}, \vec{r}') \vec{f}_n(\vec{r}') 2\pi a dl' \right\rangle \\ &= j\omega\mu \sum_{n=1}^M \frac{I_n}{2\pi a} \int_{L_m^+ L_n^+} \int_{L_m^+ L_n^+} \vec{G}^{\overline{\overline{A}}}(\vec{r}, \vec{r}') \vec{f}_m(\vec{r}) \cdot \vec{f}_n(\vec{r}') 2\pi a dl' dl \\ &= j\omega\mu \sum_{n=1}^M I_n \left\{ \int_{L_m^+} \int_{L_n^+} \frac{1}{l_m^+} \frac{1}{l_n^+} (\vec{r} - \vec{r}_m^+) \cdot (\vec{r}' - \vec{r}_n^+) \vec{G}^{\overline{\overline{A}}}(\vec{r}, \vec{r}') dl' dl \right. \\ &\quad - \int_{L_m^+} \int_{L_n^-} \frac{1}{l_m^+} \frac{1}{l_n^-} (\vec{r} - \vec{r}_m^+) \cdot (\vec{r}' - \vec{r}_n^-) \vec{G}^{\overline{\overline{A}}}(\vec{r}, \vec{r}') dl' dl \\ &\quad - \int_{L_m^-} \int_{L_n^+} \frac{1}{l_m^-} \frac{1}{l_n^+} (\vec{r} - \vec{r}_m^-) \cdot (\vec{r}' - \vec{r}_n^+) \vec{G}^{\overline{\overline{A}}}(\vec{r}, \vec{r}') dl' dl \\ &\quad \left. + \int_{L_m^-} \int_{L_n^-} \frac{1}{l_m^-} \frac{1}{l_n^-} (\vec{r} - \vec{r}_m^-) \cdot (\vec{r}' - \vec{r}_n^-) \vec{G}^{\overline{\overline{A}}}(\vec{r}, \vec{r}') dl' dl \right\} \\ &= j\omega\mu \sum_{n=1}^M I_n (M_{m+n+} - M_{m+n-} - M_{m-n+} + M_{m-n-}) \end{aligned} \quad (50)$$

where,

$$M_{pq} = \frac{1}{l_p l_q} \int_{L_p} \int_{L_q} (\vec{r} - \vec{r}_p) \cdot (\vec{r}' - \vec{r}_q) \vec{G}^{\overline{\overline{A}}}(\vec{r}, \vec{r}') dl' dl \quad (51)$$

l_p and l_q are the length of p^{th} and q^{th} wire cell, respectively.

The second term in the LHS of (48) is

$$2^{\text{nd}} \text{ term in LHS} = \frac{1}{j\omega\epsilon} \sum_{n=1}^M I_n (W_{m+n+} - W_{m+n-} - W_{m-n+} + W_{m-n-}) \quad (52)$$

where,

$$W_{pq} = \frac{1}{l_p l_q} \int_{L_p} \int_{L_q} G^\phi(\vec{r}, \vec{r}') dl' dl \quad (53)$$

(48) can then be written in the matrix representation.

$$\begin{bmatrix} Z_{11} & Z_{12} & \dots & Z_{1M} \\ Z_{21} & Z_{22} & \dots & Z_{2M} \\ \vdots & \vdots & \ddots & \vdots \\ Z_{M1} & Z_{M2} & \dots & Z_{MM} \end{bmatrix} \begin{bmatrix} I_1 \\ I_2 \\ \vdots \\ I_M \end{bmatrix} = \begin{bmatrix} V_1 \\ V_2 \\ \vdots \\ V_M \end{bmatrix} \quad (54)$$

where,

$$\begin{aligned} Z_{mm} &= j\omega\mu(M_{m+n+} - M_{m+n-} - M_{m-n+} + M_{m-n-}) \\ &+ \frac{1}{j\omega\epsilon} (W_{m+n+} - W_{m+n-} - W_{m-n+} + W_{m-n-}) \end{aligned} \quad (55)$$

$$\begin{aligned} V_m &= \left\langle \vec{f}_m(\vec{r}), \vec{E}^{inc}(\vec{r}) \right\rangle \\ &= \int_{L_m^+ L_m^-} \vec{f}_m(\vec{r}) \cdot \vec{E}^{inc}(\vec{r}) dl \\ &= \int_{L_m^+} \frac{1}{l_m^+} (\vec{r} - \vec{r}_m^+) \cdot \vec{E}^{inc}(\vec{r}) dl - \int_{L_m^-} \frac{1}{l_m^-} (\vec{r} - \vec{r}_m^-) \cdot \vec{E}^{inc}(\vec{r}) dl \end{aligned} \quad (56)$$

2.3.4. Lumped Element on ATW Wire Segment. The thin wire segment can be considered with finite conductivity to represent a lumped element embedded in that particular wire segment. With finite conductivity, the surface impedance boundary condition shall be satisfied on surface. (19) becomes,

$$\hat{n}(\vec{r}) \times (\vec{E}^{inc}(\vec{r}) + \vec{E}^{sct}(\vec{r})) = Z_s(\vec{r}) [\hat{n}(\vec{r}) \times \vec{J}_s(\vec{r})] \quad (57)$$

Test above equation by the same basis function $\vec{f}_m(\vec{r})$, which is defined on surface, one obtains,

$$\left\langle \vec{f}_m(\vec{r}), -\vec{E}^{sct}(\vec{r}) \right\rangle + \left\langle \vec{f}_m(\vec{r}), Z_s(\vec{r}) \vec{J}_s(\vec{r}) \right\rangle = \left\langle \vec{f}_m(\vec{r}), \vec{E}^{inc}(\vec{r}) \right\rangle \quad (58)$$

where the RHS is the original excitation term, the 1st term on LHS is the original impedance term, and the 2nd term on LHS is the additional impedance adjustment term.

For lumped element defined on a thin wire segment, the adjustment term becomes,

$$\left\langle \vec{f}_m(\vec{r}), Z_S(\vec{r}') \vec{J}_S(\vec{r}') \right\rangle = \left\langle \vec{f}_m(\vec{r}), \frac{Z_i}{\Delta_i} \sum_{n=1}^M J_n \vec{f}_n(\vec{r}') \right\rangle \quad (59)$$

where,

Z_i : the total impedance assigned to Segment i , defined by node p and q ,

$$Z_i = \begin{cases} Z_i, & \text{in Segment } i \\ 0, & \text{in other Seg} \end{cases} \quad (60)$$

Δ_i : length of Segment i ,

$Z_S(\vec{r})$: the surface impedance at \vec{r} , and $Z_S(\vec{r}) = \frac{E_{\tan}(\vec{r})}{H_{\tan}(\vec{r})}$.

The relationship between total impedance Z_i and surface impedance Z_S is (without loss of generality, assume the thin wire is z -oriented)

$$Z_i = \frac{V}{I} = \frac{E_z \Delta_i}{H_\phi 2\pi a} = \frac{E_z}{H_\phi} \frac{\Delta_i}{2\pi a} = Z_S \frac{\Delta_i}{2\pi a} \quad (61)$$

For thin wire, $J_S = \frac{I}{2\pi a}$, and given configuration in Figure 2.15, (59) reduces to

current only related to node p and q ,

$$\left\langle \vec{f}_m(\vec{r}), \frac{Z_i}{\Delta_i} [I_p \vec{f}_p(\vec{r}') + I_q \vec{f}_q(\vec{r}')] \right\rangle = \int_{L_p^+ L_q^+} \vec{f}_m(\vec{r}) \cdot \frac{Z_i}{\Delta_i} [I_p \vec{f}_p(\vec{r}') + I_q \vec{f}_q(\vec{r}')] dl \quad (62)$$

If $m=p$,

$$\int_{L_p^-} \vec{f}_p^-(\vec{r}) \cdot \frac{Z_i}{\Delta_i} [I_p \vec{f}_p(\vec{r}') + I_q \vec{f}_q(\vec{r}')] \hat{t}_i dl = \frac{Z_i}{3} I_p + \frac{Z_i}{6} I_q \quad (63)$$

If $m=q$,

$$\int_{L_q^+} \vec{f}_q^+(\vec{r}) \cdot \frac{Z_i}{\Delta_i} [I_p \vec{f}_p(\vec{r}') + I_q \vec{f}_q(\vec{r}')] \hat{t}_i dl = \frac{Z_i}{6} I_p + \frac{Z_i}{3} I_q \quad (64)$$

Therefore, it is equivalent to add $Z_i/3$ or $Z_i/6$ to the original impedance matrix at specific entries, as shown in Figure 2.16.

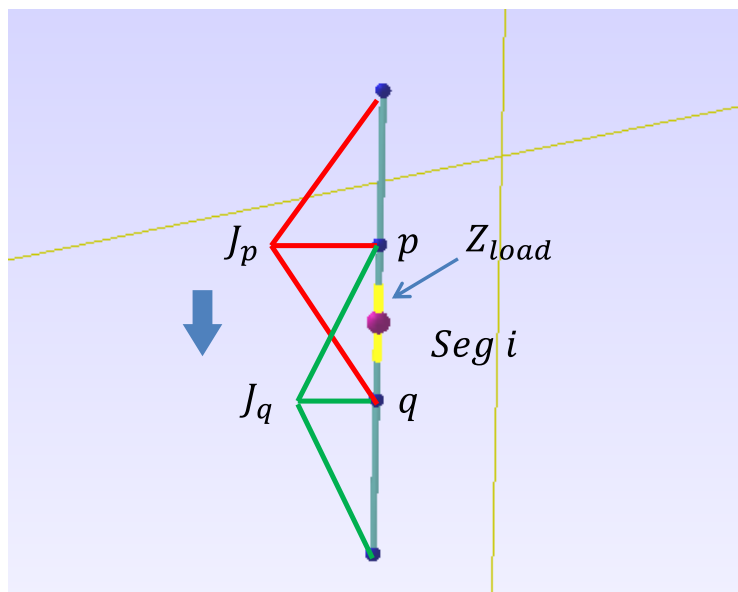


Figure 2.15. Lumped Element Defined on Wire Segment

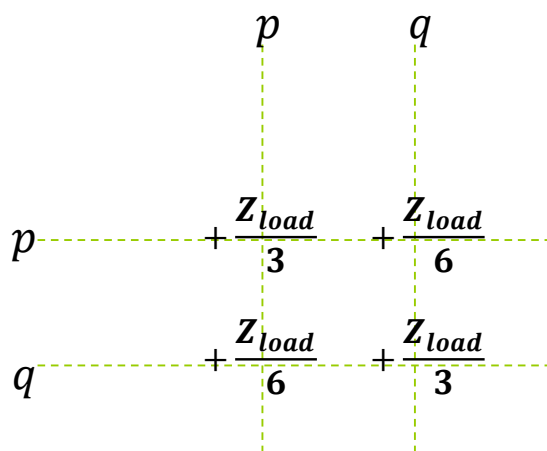


Figure 2.16. Adjustment of Original Impedance Matrix

2.3.5. Discrete Voltage Source on ATW Wire Segment. When a discrete voltage source is added on wire segment- i , it is equivalent to apply an impressed E-field only between node p and q , as shown in Figure 2.17.

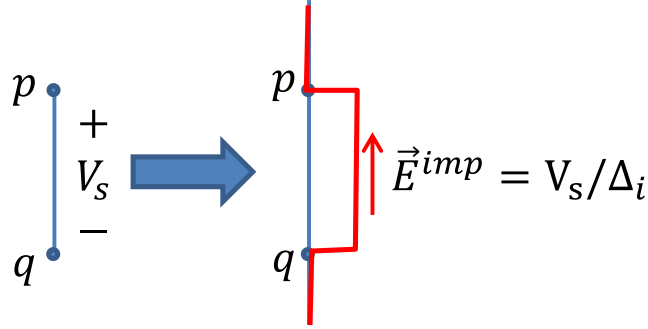


Figure 2.17. Equivalence of Discrete Voltage Source

Using integral of (56), the adjustment of excitation term is like equivalently adding $V_s / 2$ to both V_p and V_q .

2.3.6. Interaction between Surface and ATW Wire Segment. Recall (34) for surface structure EFIE impedance matrix and (55) for thin wire structure impedance matrix,

$$\begin{aligned}
 Z_{mn}^{surface} &= j\omega\mu \frac{l_m l_n}{4} (M_{m+n+}^{ss} - M_{m+n-}^{ss} - M_{m-n+}^{ss} + M_{m-n-}^{ss}) \\
 &\quad + \frac{1}{j\omega\epsilon} l_m l_n (W_{m+n+}^{ss} - W_{m+n-}^{ss} - W_{m-n+}^{ss} + W_{m-n-}^{ss}) \\
 Z_{mn}^{thin_wire} &= j\omega\mu (M_{m+n+}^{ww} - M_{m+n-}^{ww} - M_{m-n+}^{ww} + M_{m-n-}^{ww}) \\
 &\quad + \frac{1}{j\omega\epsilon} (W_{m+n+}^{ww} - W_{m+n-}^{ww} - W_{m-n+}^{ww} + W_{m-n-}^{ww})
 \end{aligned} \tag{65}$$

If m represents the surface edge, and n represents the thin wire edge, the interaction between surface and thin wire is

$$\begin{aligned}
 Z_{mn}^{sw} &= j\omega\mu \frac{l_m}{2} (M_{m+n+}^{sw} - M_{m+n-}^{sw} - M_{m-n+}^{sw} + M_{m-n-}^{sw}) \\
 &\quad + \frac{1}{j\omega\epsilon} l_m (W_{m+n+}^{ss} - W_{m+n-}^{sw} - W_{m-n+}^{sw} + W_{m-n-}^{sw})
 \end{aligned} \tag{66}$$

where M_{pq}^{sw} and W_{pq}^{sw} are defined as

$$\begin{aligned}
 M_{pq}^{sw} &= \frac{1}{A_p L_q} \int_{T_p} \int_{L_q} (\vec{r} - \vec{r}_p) \cdot (\vec{r}' - \vec{r}_q) G_0(\vec{r}, \vec{r}') ds' dl \\
 W_{pq}^{sw} &= \frac{1}{A_p L_q} \int_{T_p} \int_{L_q} G_0(\vec{r}, \vec{r}') ds' dl
 \end{aligned} \tag{67}$$

2.4. PARTIAL CIRCUIT ELEMENT EXTRACTION FROM MOM

The traditional MoM equations can be recast into a set of linear partial circuit element equations, extracted from MoM [72]. The circuit nodal analysis is used to construct those equations, and therefore, we could call this approach ‘‘Nodal MoM’’. In this way, external ideal lumped circuit elements can be easily added by stamping them into the right entries of the original nodal analysis equations. The results from nodal MoM will be used for comparison in Section 2.6.2 later on.

2.4.1. Surface Structure. For surface structure, recall the MPIE in(20).

$$\hat{n} \times \left[-j\omega\mu \int_{S'} \overline{\overline{G}}^A(\vec{r}, \vec{r}') \vec{J}(\vec{r}') ds' - \frac{1}{\epsilon} \nabla \int_{S'} G^\phi(\vec{r}, \vec{r}') \sigma(\vec{r}') ds' \right] = -\hat{n} \times \vec{E}^{inc}(\vec{r}) \quad (68)$$

Unlike the EFIE in (22), $\vec{J}(\vec{r}')$ (related to \vec{A}) and $\sigma(\vec{r}')$ (related to ϕ) are mixed together in(68). Using the same RWG basis functions in(24), the surface current density $\vec{J}(\vec{r}')$ is expanded

$$\vec{J}(\vec{r}') = \sum_{n=1}^M J_n \vec{f}_n(\vec{r}') = \sum_{n=1}^M \frac{i_n}{l_n} \vec{f}_n(\vec{r}') \quad (69)$$

where M is the total number of interior edges, and i_n is the unknown current associated with the n^{th} edge, l_n is the length of the n^{th} edge. Notice here i_n is edge based, so an edge is defined as a circuit branch, and i_n is a branch-wise current (unit is Ampere).

Again substitute (69) into(68), and apply Galerkin’s method on the MPIE formula, we get

$$\left\langle \vec{f}_m(\vec{r}), j\omega\mu \sum_{n=1}^M J_n \int_{S'} \overline{\overline{G}}^A(\vec{r}, \vec{r}') \vec{f}_n(\vec{r}') ds' \right\rangle + \left\langle \vec{f}_m(\vec{r}), \nabla'_s \phi(\vec{r}') \right\rangle = 0 \quad (70)$$

Notice the first term of LHS is exactly the same as the first term of LHS in EFIE. The second term is derived below. Due to the self-adjoint property of the linear operator ∇ ,

$$\left\langle \vec{f}_m(\vec{r}), \nabla'_s \phi(\vec{r}') \right\rangle = \left\langle \nabla_s \cdot \vec{f}_m(\vec{r}), \phi(\vec{r}') \right\rangle \quad (71)$$

Recall the important property #3 of RWG basis function in(26), divergence of RWG basis function is constant within one cell,

$$\nabla \cdot \vec{f}_n(\vec{r}) = \frac{\pm 1}{\rho_n^\pm} \frac{\partial}{\partial \rho_n^\pm} (\rho_n^\pm f_n) = \begin{cases} \frac{l_n}{A_n^+}, & \vec{r} \in T_n^+ \\ -\frac{l_n}{A_n^-}, & \vec{r} \in T_n^- \\ 0, & \text{elsewhere} \end{cases} \quad (72)$$

(71) is derived as

$$\begin{aligned} \langle \vec{f}_m(\vec{r}), \nabla'_s \phi(\vec{r}') \rangle &= \langle \nabla_s \cdot \vec{f}_m(\vec{r}), \phi(\vec{r}') \rangle \\ &= \int_{T_m^+ + T_m^-} [\nabla_s \cdot \vec{f}_m(\vec{r})] \phi(\vec{r}') ds \\ &= \int_{T_m^+} \frac{l_m}{A_m^+} \phi_{T_m^+} ds + \int_{T_m^-} -\frac{l_m}{A_m^-} \phi_{T_m^-} ds \\ &= l_m (\phi_{T_m^+} - \phi_{T_m^-}) \end{aligned} \quad (73)$$

where we have assumed that the scalar electric potential ϕ is constant within one cell.

Notice that a cell can be defined as a circuit node.

Recall (29) that

$$1^{\text{st}} \text{ term in LHS} = j\omega\mu \sum_{n=1}^M J_n \frac{l_n l_n}{4} (M_{m+n+} - M_{m+n-} - M_{m-n+} + M_{m-n-}) \quad (74)$$

Substitute $J_n = \frac{i_n}{l_n}$ into (74), we get

$$1^{\text{st}} \text{ term in LHS} = j\omega l_m \sum_{n=1}^M L_{mn} i_n \quad (75)$$

where

$$L_{mn} = \frac{\mu}{4} (M_{m+n+} - M_{m+n-} - M_{m-n+} + M_{m-n-}) \quad (76)$$

Combine (73) and (75) for branch n ,

$$\begin{aligned} j\omega l_m L_{mn} i_n + l_m (\phi_{T_m^+} - \phi_{T_m^-}) &= 0 \\ j\omega L_{mn} i_n + (\phi_{T_m^+} - \phi_{T_m^-}) &= 0 \end{aligned} \quad (77)$$

and write in matrix representation, one get

$$j\omega \overline{\overline{\mathbf{L}}} i - \overline{\overline{\mathbf{\Lambda}}} \phi = 0 \quad (78)$$

where $\overline{\overline{\mathbf{\Lambda}}}$ is connectivity matrix between edge-wise quantities and cell-wise quantities, the element of $\overline{\overline{\mathbf{\Lambda}}}$ is

$$\Lambda_{\alpha n} = \begin{cases} 1, & \text{if cell } n \text{ is edge } \alpha\text{'s positive side;} \\ -1, & \text{if cell } n \text{ is edge } \alpha\text{'s negative side;} \\ 0, & \text{otherwise.} \end{cases} \quad (79)$$

To further extract capacitance term related to cell-wise electric potential ϕ , the continuity equation for current density is utilized. Recall(21), in time harmonic representation,

$$\nabla_s \cdot \vec{J} = -j\omega\sigma \quad (80)$$

On the other hand, *nodal current* can be defined as total current flowing out of the corresponding mesh cell (as shown in Figure 2.18), which means from divergence theorem,

$$I_n = \oint_C \hat{n} \cdot \vec{J}(\vec{r}') dl' = \iint_{T_n} \nabla'_s \cdot \vec{J}(\vec{r}') ds' \quad (81)$$

Integrate (80) over Cell n ,

$$\begin{aligned} -j\omega \iint_{T_n} \sigma ds &= \iint_{T_n} \nabla_s \cdot \vec{J} ds \\ -j\omega Q_n &= I_n \end{aligned} \quad (82)$$

where, Q_n is total charge within Cell n , and I_n is the impressed nodal current source of Cell n .

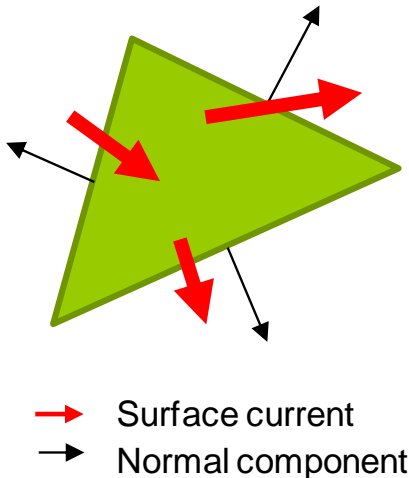


Figure 2.18. Relation between Nodal Current and Branch Current

The induced nodal currents are related to the induced branch-wise currents by connectivity matrix as

$$\bar{I} = \bar{\Lambda}^T i \quad (83)$$

The continuity equation can then be described in matrix representation as

$$-j\omega\bar{Q} = \bar{I} + \bar{I}^e \quad (84)$$

where \bar{I}^e is the impressed current.

Since surface charge density $\sigma(\vec{r})$ is constant over each cell, the charge density can be expressed using *pulse basis functions*.

$$\sigma(\vec{r}) = \sum_{n=1}^N \frac{Q_n}{A_n} p_n(\vec{r}) \quad (85)$$

where

$$p_n(\vec{r}) = \begin{cases} 1, & \vec{r} \text{ in cell } n \\ 0, & \text{elsewhere} \end{cases} \quad (86)$$

Then recall (17), the electric potential $\phi(\vec{r})$ is related to the surface charge density $\sigma(\vec{r}')$ by the scalar electric potential Green's function as,

$$\phi(\vec{r}) = \frac{1}{\epsilon} \int_{S'} G^\phi(\vec{r}, \vec{r}') \sigma(\vec{r}') ds' = \frac{1}{\epsilon} \int_{S'} \sum_{n=1}^N \frac{Q_n}{A_n} p_n(\vec{r}') G^\phi(\vec{r}, \vec{r}') ds' \quad (87)$$

Apply Galerkin's method again on (87), we get

$$\left\langle \frac{p_m(\vec{r})}{A_m}, \phi(\vec{r}) \right\rangle = \left\langle \frac{p_m(\vec{r})}{A_m}, \frac{1}{\epsilon} \sum_{n=1}^N \frac{Q_n}{A_n} p_n(\vec{r}') \int_{T_n} G^\phi(\vec{r}, \vec{r}') ds' \right\rangle \quad (88)$$

The inner product is evaluated over the cell m (which is triangle T_m).

$$\begin{aligned} \phi_m(\vec{r}) &= \frac{1}{A_m} \frac{1}{\epsilon} \sum_{n=1}^N \frac{Q_n}{A_n} \int_{T_m} p_m(\vec{r}) \int_{T_n} p_n(\vec{r}') G^\phi(\vec{r}, \vec{r}') ds' ds \\ &= \sum_{n=1}^N \frac{Q_n}{\epsilon A_m A_n} \int_{T_m} \int_{T_n} G^\phi(\vec{r}, \vec{r}') ds' ds \end{aligned} \quad (89)$$

where N is the total number of mesh cells. Write (89) in matrix representation, one gets

$$\begin{aligned} \bar{\phi} &= \bar{\mathbf{K}} \bar{Q} \\ \bar{\mathbf{C}} &= \bar{\mathbf{K}}^{-1} \end{aligned} \quad (90)$$

where $\overline{\mathbf{K}}$ is the cell-wise matrix of coefficient of potential, and

$$K_{pq} = \frac{1}{\varepsilon} W_{pq} \quad (91)$$

Using (78), (83), (84), and (90), a discretized form of a mixed potential integral equation (MPIE) results as

$$\begin{bmatrix} j\omega\overline{\mathbf{C}} & \overline{\mathbf{\Lambda}}^T \\ -\overline{\mathbf{\Lambda}} & j\omega\overline{\mathbf{L}} \end{bmatrix} \begin{bmatrix} \overline{\phi} \\ \overline{i} \end{bmatrix} = \begin{bmatrix} -\overline{I}^e \\ \overline{0} \end{bmatrix} \quad (92)$$

This equation is like the MNA (Modified Nodal Analysis) used in most commercial SPICE-like solvers.

2.4.2. Thin Wire Structure. The MPIE formulation for thin wire structures is the same as surface structures. Recall the MPIE formula in (20) again,

$$\hat{n} \times \left[-j\omega\mu \int_{S'} \overline{\mathbf{G}}^A(\vec{r}, \vec{r}') \overline{J}(\vec{r}') ds' - \frac{1}{\varepsilon} \nabla \int_{S'} G^\phi(\vec{r}, \vec{r}') \sigma(\vec{r}') ds' \right] = 0 \quad (93)$$

and basis function expansion in (47),

$$\overline{J}(\vec{r}') = \frac{1}{2\pi a} \sum_{n=1}^M i_n \overline{f}_n(\vec{r}') \quad (94)$$

where there is no azimuthal component of current, $\overline{f}_n(\vec{r}')$ is everywhere tangential to the wire, in axial direction.

Similar to (70) and (71), the Galerkin's method is applied to the MPIE formula, we get

$$\left\langle \overline{f}_m(\vec{r}), j\omega\mu \sum_{n=1}^M J_n \int_{S'} \overline{\mathbf{G}}^A(\vec{r}, \vec{r}') \overline{f}_n(\vec{r}') ds' \right\rangle + \left\langle \overline{f}_m(\vec{r}), \nabla'_s \phi(\vec{r}') \right\rangle = 0 \quad (95)$$

Inner product is defined on **1-D** rooftop basis,

$$j\omega\mu \sum_{n=1}^M \frac{i_n}{2\pi a} \int_{l_m} \overline{f}_m(\vec{r}) \int_{l'_n} \overline{f}_n(\vec{r}') \overline{\mathbf{G}}^A(\vec{r}, \vec{r}') 2\pi a dl'_n dl_m + \left\langle \nabla \cdot \overline{f}_m(\vec{r}), \phi(\vec{r}') \right\rangle = 0 \quad (96)$$

For thin wire approximation, the source point is defined on the thin wire surface, while the testing point is defined on the thin wire axial. The second term on the Left Hand Side is derived as

$$\begin{aligned}
\langle \nabla \cdot \vec{f}_m(\vec{r}), \phi(\vec{r}) \rangle &= \int_{l_m} \nabla \cdot \vec{f}_m(\vec{r}) \phi(\vec{r}) dl_m \\
&= \int_{L_{m+}} \nabla \cdot \vec{f}_m(\vec{r}) \phi_{L_{m+}} dl_{m+} + \int_{L_{m-}} \nabla \cdot \vec{f}_m(\vec{r}) \phi_{L_{m-}} dl_{m-} \\
&= \int_{L_{m+}} \frac{1}{l_{m+}}(\vec{r}) \phi_{L_{m+}} dl_{m+} + \int_{L_{m-}} \frac{-1}{l_{m-}}(\vec{r}) \phi_{L_{m-}} dl_{m-} \\
&= \phi_{L_{m+}} - \phi_{L_{m-}}
\end{aligned} \tag{97}$$

Recall (50) that

$$1^{\text{st}} \text{ term in LHS} = j\omega\mu \sum_{n=1}^M i_n (M_{m+n+} - M_{m+n-} - M_{m-n+} + M_{m-n-}) \tag{98}$$

$$1^{\text{st}} \text{ term in LHS} = j\omega \sum_{n=1}^M i_n L_{mn} \tag{99}$$

where

$$L_{mn} = \mu(M_{m+n+} - M_{m+n-} - M_{m-n+} + M_{m-n-}) \tag{100}$$

Combine (97) and (99) for branch n ,

$$j\omega L_{mn} i_n + (\phi_{L_{m+}} - \phi_{L_{m-}}) = 0 \tag{101}$$

Write in matrix representation,

$$j\omega \overline{\mathbf{L}} \overline{\mathbf{i}} - \overline{\mathbf{\Lambda}} \overline{\phi} = 0 \tag{102}$$

where $\mathbf{\Lambda}$ is connectivity matrix between edge-wise quantities and cell-wise quantities, the element of $\mathbf{\Lambda}$ is

$$\mathbf{\Lambda}_{\alpha n} = \begin{cases} 1, & \text{if cell } n \text{ is edge } \alpha \text{'s positive side;} \\ -1, & \text{if cell } n \text{ is edge } \alpha \text{'s negative side;} \\ 0, & \text{otherwise.} \end{cases} \tag{103}$$

To further extract capacitance term related to cell-wise electric potential ϕ , the continuity equation for current density is utilized. Recall(21), in time harmonic representation,

$$\nabla_s \cdot \vec{J} = -j\omega\sigma \tag{104}$$

For thin wire approximation, surface current is uniformly distributed along the azimuthal direction ($J_n = \frac{i_n}{2\pi a}$). Peel off the surface of Cell n , and apply divergence theorem, as shown in Figure 2.19, we get

$$I_n = \oint_C \hat{n} \cdot \vec{J}(\vec{r}') dl = \iint_{S_n} \nabla_s \cdot \vec{J}(\vec{r}') ds$$

$$LHS : \oint_C \hat{n} \cdot \vec{J} dl = 2\pi a (J_{m+1} - J_m) = i_{m+1} - i_m \quad (105)$$

$$RHS : \iint_{S_n} \nabla_s \cdot \vec{J} ds = -j\omega \iint_{S_n} \sigma ds = -j\omega Q_n$$

$$-j\omega Q_n = I_n \quad (106)$$

where, Q_n is total charge within Cell n , and I_n is the impressed nodal current source of Cell n . The induced nodal currents are related to the induced branch-wise currents by connectivity matrix as

$$\bar{I} = \bar{\Lambda}^T \bar{i} \quad (107)$$

The continuity equation can then be described in matrix representation as

$$-j\omega \bar{Q} = \bar{I} + \bar{I}^e \quad (108)$$

where \bar{I}^e is the impressed current.

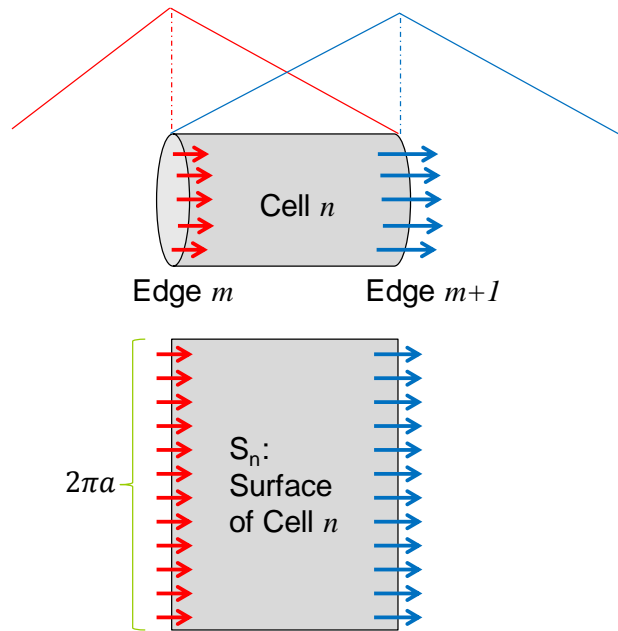


Figure 2.19. Surface Current Density Distribution on Cell n

Since surface charge density $\sigma(\vec{r})$ is constant over each cell, the charge density can be expressed using *pulse basis functions*.

$$\sigma(\vec{r}) = \sum_{n=1}^N \frac{Q_n}{2\pi a l_n} p_n(\vec{r}) \quad (109)$$

where l_n is the length of the wire cell n , and

$$p_n(\vec{r}) = \begin{cases} 1, & \vec{r} \text{ in cell } n \\ 0, & \text{elsewhere} \end{cases} \quad (110)$$

Then recall (17), the electric potential $\phi(\vec{r})$ is related to the surface charge density $\sigma(\vec{r}')$ by the scalar electric potential Green's function as,

$$\phi(\vec{r}) = \frac{1}{\epsilon} \int_{S'} G^\phi(\vec{r}, \vec{r}') \sigma(\vec{r}') ds' = \frac{1}{\epsilon} \int_{S'} \sum_{n=1}^N \frac{Q_n p_n(\vec{r}')}{2\pi a l_n} G^\phi(\vec{r}, \vec{r}') ds' \quad (111)$$

The above integral is evaluated over the cell m (which is wire surface m), and the below inner product for pulse basis function is evaluated over cell as well. Apply Galerkin's method again on(111), we get

$$\left\langle \frac{p_m(\vec{r})}{2\pi a l_m}, \phi(\vec{r}) \right\rangle = \left\langle \frac{p_m(\vec{r})}{2\pi a l_m}, \frac{1}{\epsilon} \int_{S'} \sum_{n=1}^N \frac{Q_n p_n(\vec{r}')}{2\pi a l_n} G^\phi(\vec{r}, \vec{r}') ds' \right\rangle \quad (112)$$

The left hand side of (112) is

$$\begin{aligned} \left\langle \frac{p_m(\vec{r})}{2\pi a l_m}, \phi(\vec{r}) \right\rangle &= \int_l \int_\phi \frac{p_m(\vec{r}) \phi(\vec{r})}{2\pi a l_m} a d\phi dl \\ &= \int_{l_m} \frac{\phi_m(\vec{r})}{l_m} dl \\ &= \phi_m(\vec{r}) \end{aligned} \quad (113)$$

The right hand side of (112) is

$$\begin{aligned} &\left\langle \frac{p_m(\vec{r})}{2\pi a l_m}, \frac{1}{\epsilon} \int_{S'} \sum_{n=1}^N \frac{Q_n p_n(\vec{r}')}{2\pi a l_n} G^\phi(\vec{r}, \vec{r}') ds' \right\rangle \\ &= \frac{1}{\epsilon} \sum_{n=1}^N Q_n \int_{S_m} \frac{p_m(\vec{r})}{2\pi a l_m} \int_{S'_n} \frac{p_n(\vec{r}')}{2\pi a l_n} G^\phi(\vec{r}, \vec{r}') ds'_n ds_m \\ &= \frac{1}{\epsilon} \sum_{n=1}^N Q_n \frac{1}{l_m} \frac{1}{l_n} \int_{L_m} \int_{L'_n} G^\phi(\vec{r}, \vec{r}') dl'_n dl_m \end{aligned} \quad (114)$$

Recall (53),

$$W_{pq} = \frac{1}{l_p l_q} \int_{L_p} \int_{L_q} G^\phi(\vec{r}, \vec{r}') dl' dl \quad (115)$$

(113)and (114)can be written as

$$\phi_m(\vec{r}) = \sum_{n=1}^N Q_n K_{mn} \quad (116)$$

where N is the total number of mesh cells, and

$$\begin{aligned} K_{mn} &= \frac{1}{\varepsilon} \frac{1}{l_m} \frac{1}{l_n} \int_{L_m} \int_{L'_n} G^\phi(\vec{r}, \vec{r}') dl'_n dl_m \\ &= \frac{W_{mn}}{\varepsilon} \end{aligned} \quad (117)$$

Write (116)in matrix representation,

$$\begin{aligned} \vec{\phi} &= \overline{\overline{\mathbf{K}}} \overline{\overline{\mathbf{Q}}} \\ \overline{\overline{\mathbf{C}}} &= \overline{\overline{\mathbf{K}}}^{-1} \end{aligned} \quad (118)$$

where $\overline{\overline{\mathbf{K}}}$ is the cell-wise matrix of coefficient of potential.

Using(102),(107),(108) and(118), a discretized form of a mixed potential integral equation (**MPIE**) results as

$$\begin{bmatrix} j\omega \overline{\overline{\mathbf{C}}} & \overline{\overline{\mathbf{\Lambda}}}^T \\ -\overline{\overline{\mathbf{\Lambda}}} & j\omega \overline{\overline{\mathbf{L}}} \end{bmatrix} \begin{bmatrix} \vec{\phi} \\ \vec{i} \end{bmatrix} = \begin{bmatrix} -\vec{I}^e \\ \vec{0} \end{bmatrix} \quad (119)$$

2.4.3. Interaction between Surface and Thin Wire Structures. Recalling the partial inductance and partial capacitance definition for both surface structure and thin wire structure, we get for surface structure,

$$\begin{aligned} L_{mn}^{surface} &= \frac{1}{4} \mu (M_{m+n+} - M_{m+n-} - M_{m-n+} + M_{m-n-}) \\ K_{i_{r-p}, j_{r-p}}^{surface} &= \frac{W_{m+n+}}{\varepsilon} > 0 \\ K_{i_{r-p}, j_{r-n}}^{surface} &= \frac{W_{m+n-}}{\varepsilon} > 0 \\ K_{i_{r-n}, j_{r-p}}^{surface} &= \frac{W_{m-n+}}{\varepsilon} > 0 \\ K_{i_{r-n}, j_{r-n}}^{surface} &= \frac{W_{m-n-}}{\varepsilon} > 0 \end{aligned} \quad (120)$$

where

$$\begin{aligned}
M_{pq} &= \frac{1}{A_p A_q} \int_{T_p} \int_{T_q} (\vec{r} - \vec{r}_p) \cdot (\vec{r}' - \vec{r}_q) G_0(\vec{r}, \vec{r}') ds' ds \\
W_{pq} &= \frac{1}{A_p A_q} \int_{T_p} \int_{T_q} G_0(\vec{r}, \vec{r}') ds' ds
\end{aligned} \tag{121}$$

For thin wire structure,

$$\begin{aligned}
L_{mn}^{thin_wire} &= \mu(M_{m+n+} - M_{m+n-} - M_{m-n+} + M_{m-n-}) \\
K_{i_{Seg_p}, j_{Seg_p}}^{thin_wire} &= \frac{W_{m+n+}}{\varepsilon} > 0 \\
K_{i_{Seg_p}, j_{Seg_n}}^{thin_wire} &= \frac{W_{m+n-}}{\varepsilon} > 0 \\
K_{i_{Seg_n}, j_{Seg_p}}^{thin_wire} &= \frac{W_{m-n+}}{\varepsilon} > 0 \\
K_{i_{Seg_n}, j_{Seg_n}}^{thin_wire} &= \frac{W_{m-n-}}{\varepsilon} > 0
\end{aligned} \tag{122}$$

where

$$\begin{aligned}
M_{pq} &= \frac{1}{L_p L_q} \int_{L_p} \int_{L_q} (\vec{r} - \vec{r}_p) \cdot (\vec{r}' - \vec{r}_q) G_0(\vec{r}, \vec{r}') dl' dl \\
W_{pq} &= \frac{1}{L_p L_q} \int_{L_p} \int_{L_q} G_0(\vec{r}, \vec{r}') dl' dl
\end{aligned} \tag{123}$$

If m represents the surface edge, and n represents the thin wire edge, the interaction between surface and thin wire is

$$\begin{aligned}
L_{mn} &= \frac{1}{2} \mu(M_{m+n+} - M_{m+n-} - M_{m-n+} + M_{m-n-}) \\
K_{i_{Tr_p}, j_{Seg_p}} &= \frac{W_{m+n+}}{\varepsilon} > 0 \\
K_{i_{Tr_p}, j_{Seg_n}} &= \frac{W_{m+n-}}{\varepsilon} > 0 \\
K_{i_{Tr_n}, j_{Seg_p}} &= \frac{W_{m-n+}}{\varepsilon} > 0 \\
K_{i_{Tr_n}, j_{Seg_n}} &= \frac{W_{m-n-}}{\varepsilon} > 0
\end{aligned} \tag{124}$$

where

$$\begin{aligned}
M_{pq} &= \frac{1}{A_p L_q} \int_{T_p} \int_{L_q} (\vec{r} - \vec{r}_p) \cdot (\vec{r}' - \vec{r}_q) G_0(\vec{r}, \vec{r}') ds' dl \\
W_{pq} &= \frac{1}{A_p L_q} \int_{T_p} \int_{L_q} G_0(\vec{r}, \vec{r}') ds' dl
\end{aligned} \tag{125}$$

To construct the complete circuit network equation, $\overline{\overline{\mathbf{L}}}$ and $\overline{\overline{\mathbf{K}}}$ matrix for both surface and thin wire should be combined together,

$$\overline{\overline{\mathbf{L}}} = \begin{bmatrix} \overline{\overline{\mathbf{L}}}_s & \overline{\overline{\mathbf{L}}}_{sw} \\ \overline{\overline{\mathbf{L}}}_{sw}^T & \overline{\overline{\mathbf{L}}}_w \end{bmatrix} \tag{126}$$

$$\overline{\overline{\mathbf{\Lambda}}} = \begin{bmatrix} \overline{\overline{\mathbf{\Lambda}}}_s & \overline{\overline{\mathbf{\Lambda}}}_{sw} \\ \overline{\overline{\mathbf{\Lambda}}}_{sw}^T & \overline{\overline{\mathbf{\Lambda}}}_w \end{bmatrix} \tag{127}$$

$$\overline{\overline{\mathbf{K}}} = \begin{bmatrix} \overline{\overline{\mathbf{K}}}_s & \overline{\overline{\mathbf{K}}}_{sw} \\ \overline{\overline{\mathbf{K}}}_{sw}^T & \overline{\overline{\mathbf{K}}}_w \end{bmatrix}, \overline{\overline{\mathbf{C}}} = \overline{\overline{\mathbf{K}}}^{-1} \tag{128}$$

$$\overline{\overline{\phi}} = \begin{bmatrix} \overline{\overline{\phi}}_s \\ \overline{\overline{\phi}}_w \end{bmatrix}, \overline{\overline{i}} = \begin{bmatrix} \overline{\overline{i}}_s \\ \overline{\overline{i}}_w \end{bmatrix} \tag{129}$$

The complete circuit network equation is as the same form,

$$\begin{bmatrix} j\omega \overline{\overline{\mathbf{C}}} & \overline{\overline{\mathbf{\Lambda}}}^T \\ -\overline{\overline{\mathbf{\Lambda}}} & j\omega \overline{\overline{\mathbf{L}}} \end{bmatrix} \begin{bmatrix} \overline{\overline{\phi}} \\ \overline{\overline{i}} \end{bmatrix} = \begin{bmatrix} -\overline{\overline{I}}^e \\ \overline{\overline{0}} \end{bmatrix} \tag{130}$$

2.4.4. Pseudo Node Concept and Case Validation. A simple two conductor transmission line structure as shown in Figure 2.20 was used for validation. The per-unit-length inductance and capacitance can be obtained analytically by

$$\begin{aligned}
l &= \frac{\mu}{\pi} \cosh^{-1} \left(\frac{D}{2a} \right) \\
c &= \frac{\pi \epsilon}{\cosh^{-1} \left(\frac{D}{2a} \right)}
\end{aligned} \tag{131}$$

where D is the separation between two cylindrical conductors, and a is the wire radius.

The port is defined between two pseudo nodes. Since when there is connection out of the wire ends, the ending current is not zero. And therefore, an inductance is

associated with that branch-wise current. But because that current is only defined on half rooftop basis, only a “half-inductance” shall be introduced into the original equivalent circuit network, as shown in Figure 2.21. Notice that the pseudo cell doesn’t introduce additional partial capacitance terms, because the area of that pseudo cell is zero, i.e., no charge is associated with the pseudo cell.

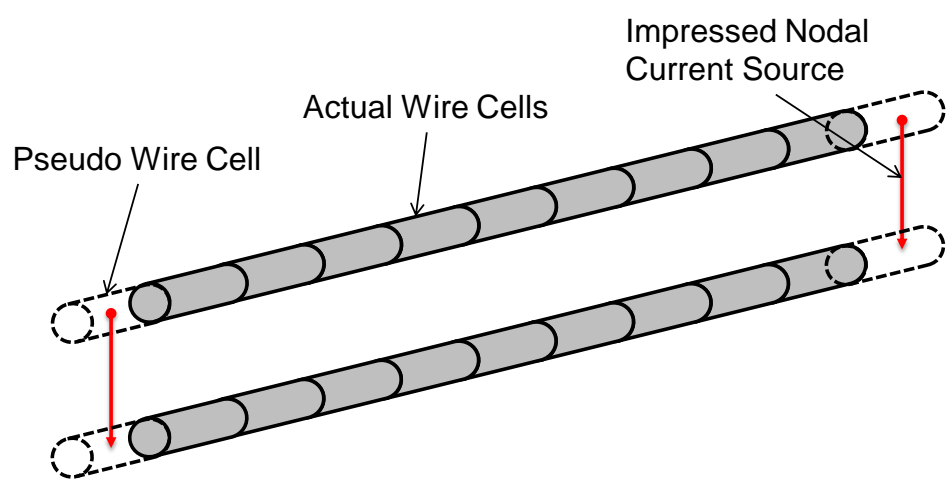


Figure 2.20. A Simple Two-conductor Transmission Line

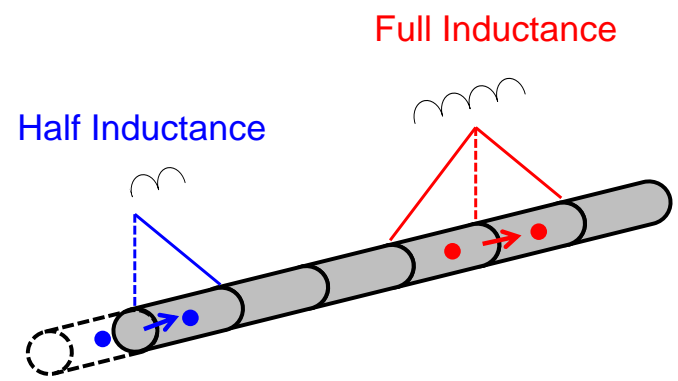


Figure 2.21. Introduction of Pseudo Cell

The Z-parameter obtained from EMC Studio [25], the equivalent circuit extraction method, and the analytical equations are compared for the same geometry

shown in Figure 2.20. By adding pseudo wire cells at the port locations, the circuit extraction method gives close results as the other two, as shown in Figure 2.22.

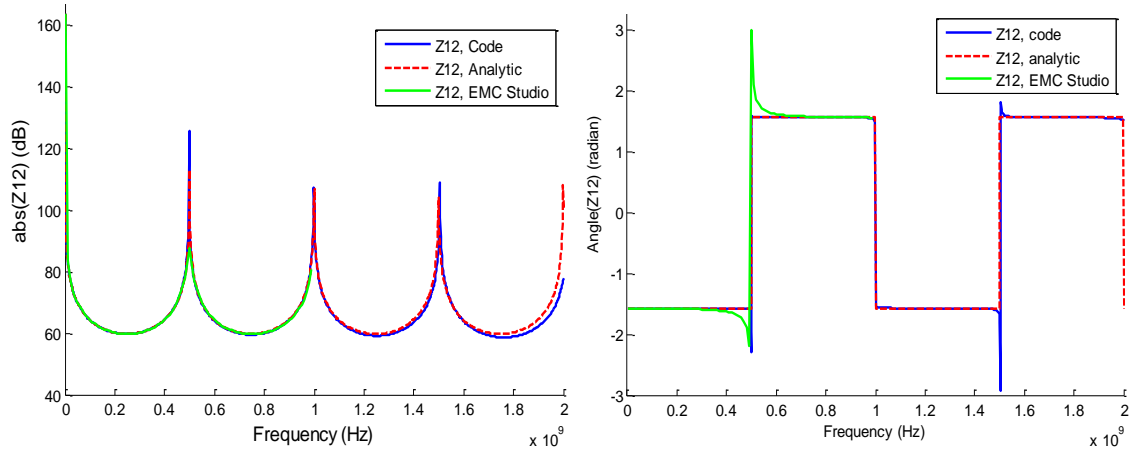


Figure 2.22. Validation by Comparing Z-parameter from Different Approaches

The loading condition on two ends can be considered as well by connecting loadings between two pseudo nodes. A voltage source in series with impedance can be easily converted to a current source in parallel with the impedance, as shown in Figure 2.23.

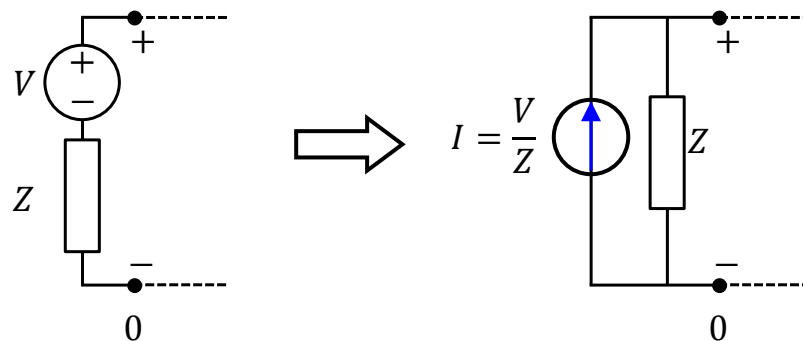


Figure 2.23. Conversion to Norton Equivalent Circuit

If the current direction is defined as in Figure 2.24, one can write KCL for pseudo nodes J and K as:

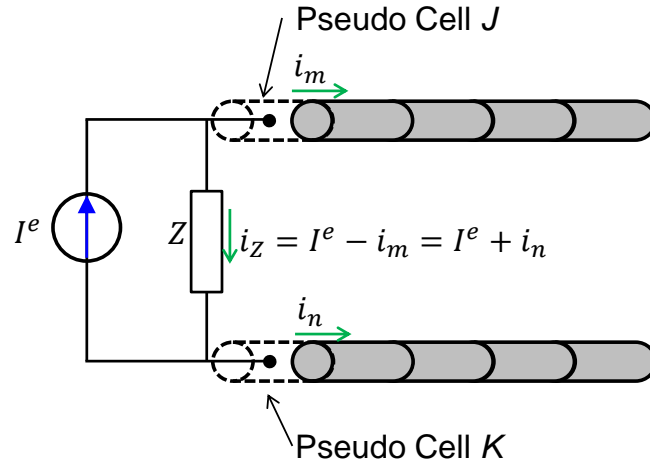


Figure 2.24. KCL for Pseudo Nodes

2.5. MTL WITH INCIDENT FIELD

2.5.1. Conventional Theory of TL-Mode Current Excited by External Fields.

Current flowing on wire-like structures consists of the so-called TL-mode and antenna-mode current. The conventional transmission line theory is only valid for TL-mode current [29]. Three different approaches have been developed to calculate the TL-mode current on transmission line due to incident field excitation [28], [31], [32], however, the three different formulations introduced here are just approximations under special conditions where TL condition holds (Section III.B, 0). The exact solution (full-wave) of two wires illuminated by external field can be calculated in an iterative manner [50].

In 1965, *Taylor* developed a Total Voltage Form representation [28]. Both incident E and H-field are considered and converted to equivalent voltage and current source along the transmission line. In the coordinate of Figure 2.25, the modified Telegrapher's Equation is

$$\begin{cases} \frac{dV^t(z)}{dz} + j\omega LI^t(z) = V_F(z) = j\omega \int_0^d B_y^e(x, 0, z) dx \\ \frac{dI^t(z)}{dz} + j\omega CV^t(z) = I_F(z) = -j\omega C \int_0^d E_x^e(x, 0, z) dx \end{cases} \quad (137)$$

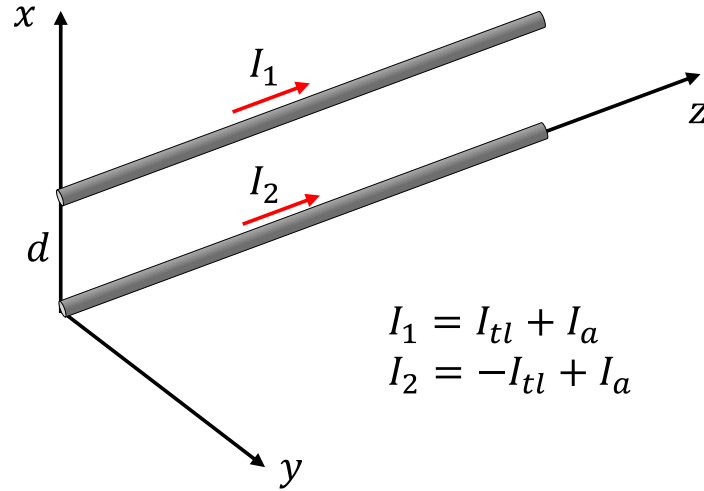


Figure 2.25. Current along Transmission Line

The detailed derivation extended to multi-conductor TL is referred to *Clayton Paul* [29], [30]. Later in 1980, Agrawal developed a Scattered Voltage Form representation [31], which only requires the tangential component of excitation E-field. The modified Telegrapher's Equation is

$$\begin{cases} \frac{dV^s(z)}{dz} + j\omega LI^s(z) = V_F(z) = E_z^e(d, 0, z) - E_z^e(0, 0, z) \\ \frac{dI^s(z)}{dz} + j\omega CV^s(z) = I_F(z) = 0 \end{cases} \quad (138)$$

Then in 1993, *Rachidi* proposed the third Scattered Current Form representation, which only requires the tangential component of excitation H-field [32]. The modified Telegrapher's Equation is

$$\begin{cases} \frac{dV^t(z)}{dz} + j\omega LI^s(z) = V_F(z) = 0 \\ \frac{dI^s(z)}{dz} + j\omega CV^t(z) = I_F(z) = -\frac{1}{L} \int_0^d \frac{\partial B_z^e}{\partial y}(x, 0, z) dx \end{cases} \quad (139)$$

The equivalent SPICE circuits for all three models are shown below in Figure 2.26, Figure 2.27, and Figure 2.28.

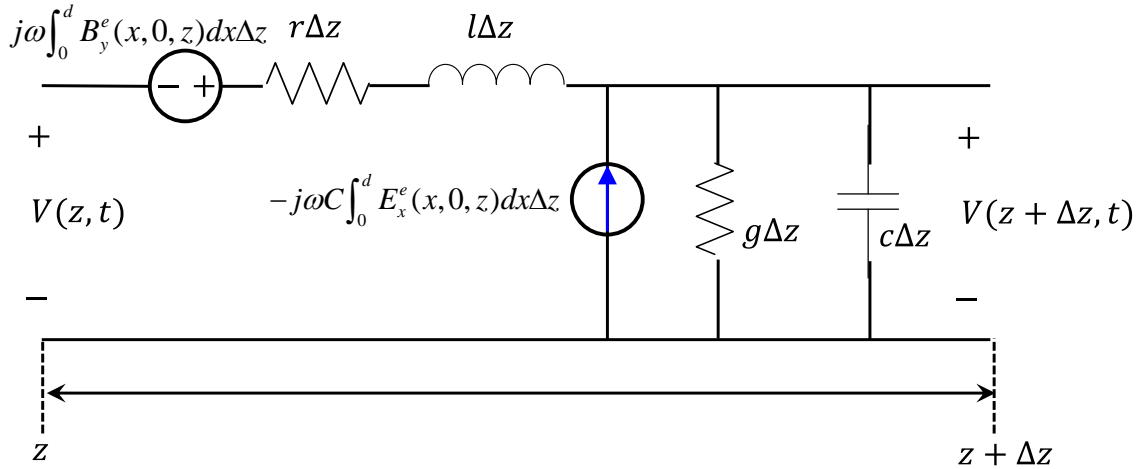


Figure 2.26. Equivalent Circuit of Taylor's Model

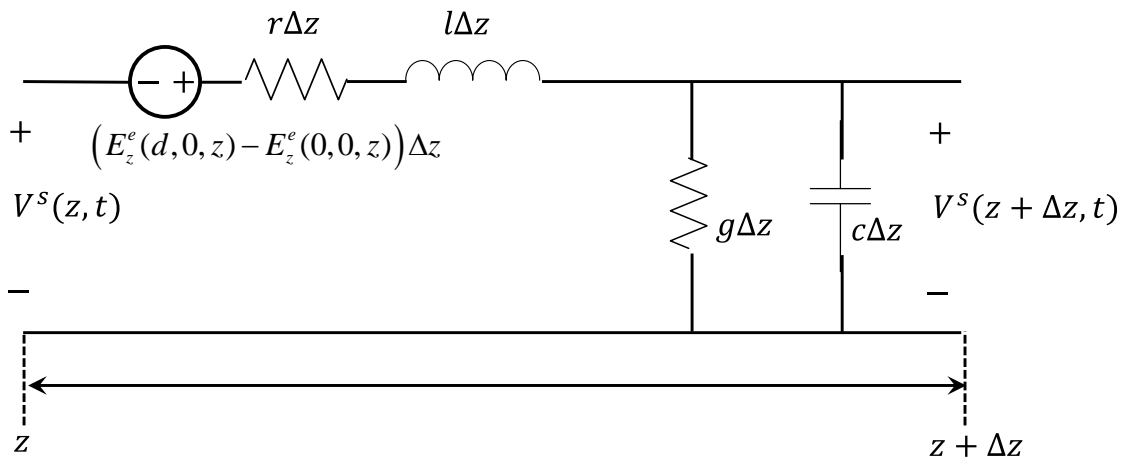


Figure 2.27. Equivalent Circuit of Agrawal's Model

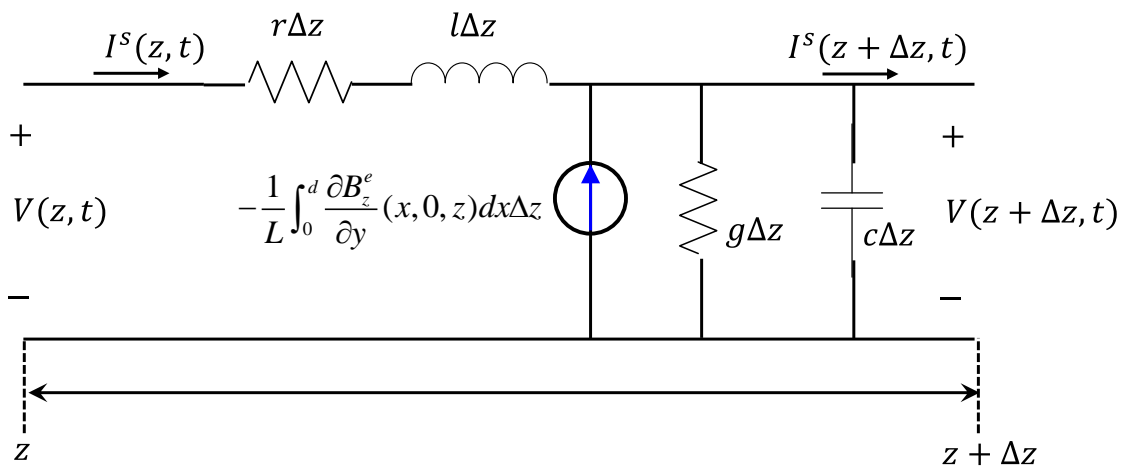


Figure 2.28. Equivalent Circuit of Rachidi's Model

All three models should give the same results if used correctly. And again, we should notice that these three models only work for estimating TL-mode current or the terminal response [34], since the antenna-mode current equals zero at wire terminals.

2.5.2. Exact TL-, Antenna-Mode Current on a Two Wire Transmission Line.

For a two wire structure, both TL and antenna mode current can be evaluated by taking advantage of Agrawal's model. The distributed scattered voltage source in Telegrapher's Equation is the difference of tangential E-field on thin wire surface for TL-mode current; while for antenna-mode current, it is the average [55].

Consider a two-wire line of length L in free space, with separation of d and wire radius a , as shown in Figure 2.25. At any position along the wires,

$$\begin{aligned} I_1(z) &= I_a(z) + I_u(z) \\ I_2(z) &= I_a(z) - I_u(z) \end{aligned} \quad (140)$$

where $I_a(z)$ and $I_u(z)$ is the antenna-mode and TL-mode currents, respectively.

As in the thin wire MoM, the scattered E-field is

$$\vec{E}^{sc} = -j\omega\vec{A} - \nabla\phi \quad (141)$$

where

$$\vec{A}(\vec{r}) = \vec{A}_1(\vec{r}) + \vec{A}_2(\vec{r}) = \frac{\mu}{4\pi} \int_0^L I_1(\vec{r}'_1) \vec{e}_z g_1(\vec{r}, \vec{r}'_1) dz' + \frac{\mu}{4\pi} \int_0^L I_2(\vec{r}'_2) \vec{e}_z g_2(\vec{r}, \vec{r}'_2) dz' \quad (142)$$

$$\phi(\vec{r}) = \phi_1(\vec{r}) + \phi_2(\vec{r}) = \frac{1}{4\pi\epsilon} \int_0^L \rho_1(\vec{r}'_1) g_1(\vec{r}, \vec{r}'_1) dz' + \frac{1}{4\pi\epsilon} \int_0^L \rho_2(\vec{r}'_2) g_2(\vec{r}, \vec{r}'_2) dz' \quad (143)$$

In the thin wire approximation, we can assume that currents are concentrated in the wire axis for the two wires. Therefore, the current continuity equation becomes:

$$\rho_{1,2} = -\frac{1}{j\omega} \nabla \cdot \vec{J}_{1,2} = -\frac{1}{j\omega} \frac{dI_{1,2}}{dz} \quad (144)$$

Substitute (144) into (142) and (143), and evaluate electric potentials on surface of both two wires,

$$\vec{A}_1(d, 0, z) = \frac{\mu}{4\pi} \int_0^L I_1(z') \vec{e}_z g_1(z, z') dz' \quad (145)$$

$$\vec{A}_2(d, 0, z) = \frac{\mu}{4\pi} \int_0^L I_2(z') \vec{e}_z g_2(z, z') dz' \quad (146)$$

$$\phi_1(d, 0, z) = -\frac{1}{4\pi\epsilon j\omega} \int_0^L \frac{dI_1(z')}{dz'} g_1(z, z') dz' \quad (147)$$

$$\phi_2(d, 0, z) = -\frac{1}{4\pi\epsilon j\omega} \int_0^L \frac{dI_2(z')}{dz'} g_2(z, z') dz' \quad (148)$$

$$\bar{A}_1(0, 0, z) = \frac{\mu}{4\pi} \int_0^L I_1(z') \bar{e}_z g_2(z, z') dz' \quad (149)$$

$$\bar{A}_2(0, 0, z) = \frac{\mu}{4\pi} \int_0^L I_2(z') \bar{e}_z g_1(z, z') dz' \quad (150)$$

$$\phi_1(0, 0, z) = -\frac{1}{4\pi\epsilon j\omega} \int_0^L \frac{dI_1(z')}{dz'} g_2(z, z') dz' \quad (151)$$

$$\phi_2(0, 0, z) = -\frac{1}{4\pi\epsilon j\omega} \int_0^L \frac{dI_2(z')}{dz'} g_1(z, z') dz' \quad (152)$$

where

$$g_1(z, z') = \frac{e^{-jk\sqrt{(z-z')^2+a^2}}}{\sqrt{(z-z')^2+a^2}} \quad (153)$$

$$g_2(z, z') = \frac{e^{-jk\sqrt{(z-z')^2+d^2}}}{\sqrt{(z-z')^2+d^2}} \quad (154)$$

Referring to the scattered voltage definition in [55], we can similarly get the two equations for TL-mode current,

$$\frac{dV^s(z)}{dz} + j\omega \frac{\mu}{2\pi} \int_0^L I_{\text{tl}}(z') [g_1(z, z') - g_2(z, z')] dz' = E_z^i(d, 0, z) - E_z^i(0, 0, z) \quad (155)$$

$$V^s(z) + \frac{1}{2\pi\epsilon j\omega} \int_0^L \frac{dI_{\text{tl}}(z')}{dz'} [g_1(z, z') - g_2(z, z')] dz' = 0 \quad (156)$$

Notice that $I_{\text{tl}}(z')$ and $\frac{dI_{\text{tl}}(z')}{dz'}$ cannot be taken out of the integral, by rigorous

derivation. If we plot $g_1(z, z') - g_2(z, z')$ for a specific z value, its shape is like a delta-function, as shown in Figure 2.29. Taking this property, (155) and (156) can be approximated as Telegrapher's equation in Agrawal's form:

$$\begin{aligned} \frac{dV_{\text{tl}}^s(z)}{dz} + j\omega L_{\text{tl}} I_{\text{tl}}(z) &= E_z^i(d, 0, z) - E_z^i(0, 0, z) \\ \frac{dI_{\text{tl}}(z)}{dz} + j\omega C_{\text{tl}} V_{\text{tl}}^s(z) &= 0 \end{aligned} \quad (157)$$

where

$$L_{\text{ul}} = \frac{\mu}{2\pi} \int_0^L [g_1(z, z') - g_2(z, z')] dz' \quad (158)$$

and

$$C_{\text{ul}} = \frac{2\pi\epsilon}{\int_0^L [g_1(z, z') - g_2(z, z')] dz'}, \quad (159)$$

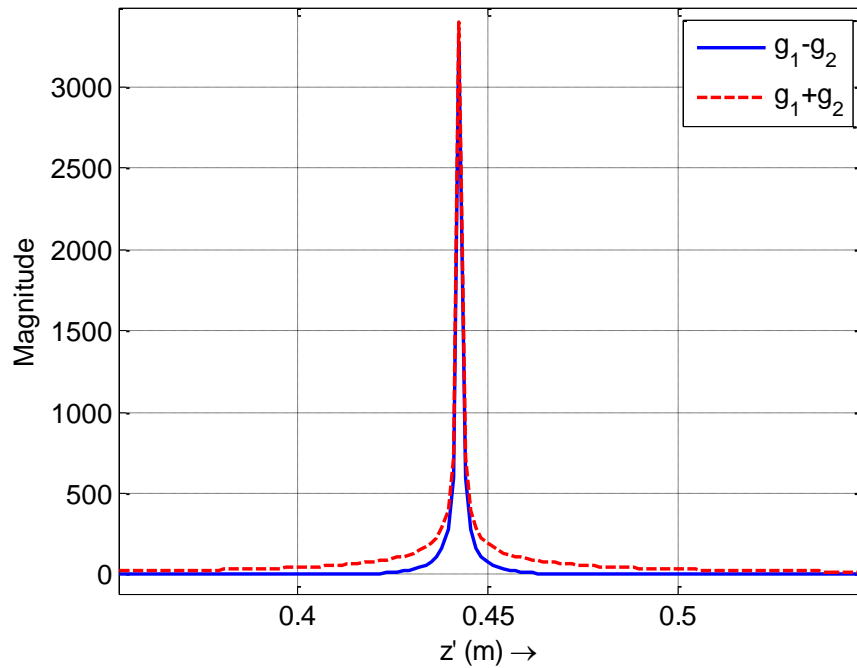


Figure 2.29. Magnitude of Green's Functions

The TL-mode per-unit-length inductance and capacitance for a two wire line is shown in Figure 2.30 and Figure 2.31. The line parameters is length $L=0.9750$ m, separation $d=0.0150$ m, wire radius $a=0.3$ mm, and frequency $f=1$ GHz. We could notice that the retardation term (imaginary part) is small compared to the real part, and it could be neglected when calculating TL-mode current. The analytical equation is the well-known formula for calculating PUL L&C of two round wires.

$$L = \frac{\mu}{\pi} \cosh^{-1}\left(\frac{d}{2a}\right) \cong \frac{\mu}{\pi} \ln\left(\frac{d}{a}\right), \text{ for } d \gg a$$

$$C = \frac{\pi\epsilon}{\cosh^{-1}(d/2a)} \cong \frac{\pi\epsilon}{\ln(d/a)}, \text{ for } d \gg a$$
(160)

Notice that when the integration limits of (158) and (159) exceed to $-\infty$ and ∞ , (158) and (159) reduces to (160) [50].

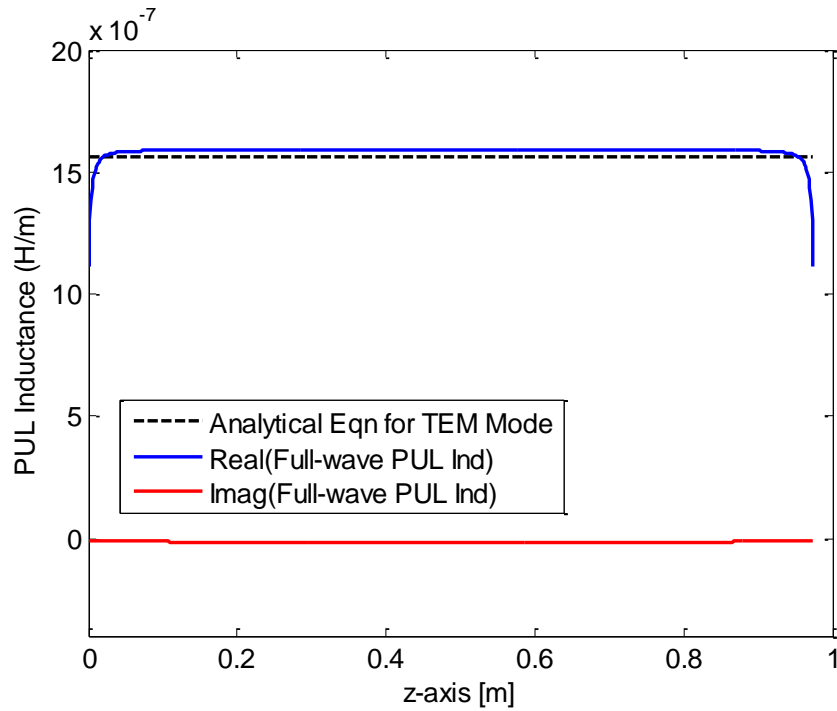


Figure 2.30. TL-mode Line Per-Unit-Length Inductance

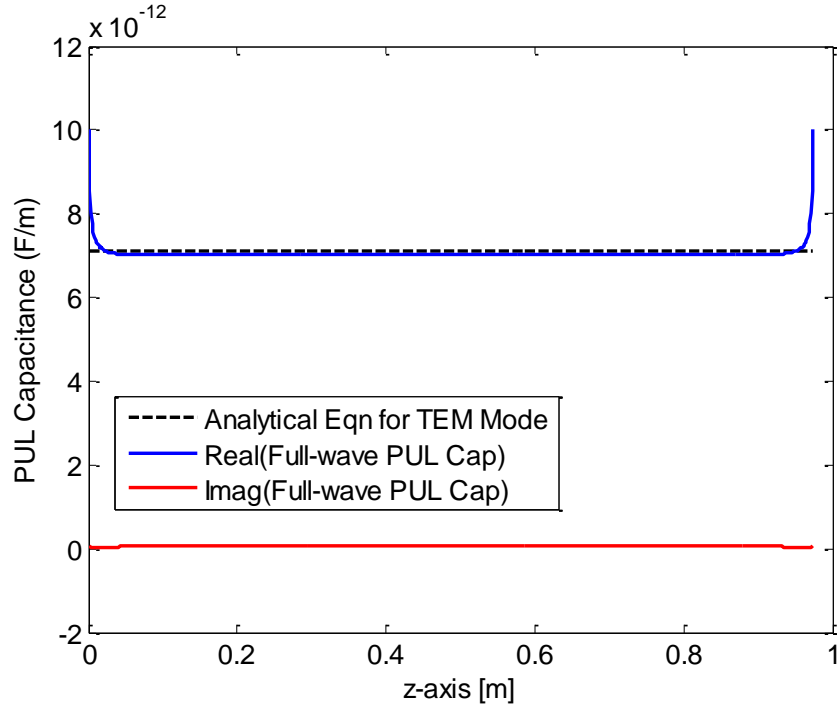


Figure 2.31. TL-mode Line Per-Unit-Length Capacitance

Similar to (155) and(156), the two equations for antenna-mode current are,

$$\frac{dV_a^s(z)}{dz} + j\omega \frac{\mu}{4\pi} \int_0^L I_a(z') [g_1(z, z') + g_2(z, z')] dz' = \frac{E_z^i(d, 0, z) + E_z^i(0, 0, z)}{2} \quad (161)$$

$$V_a^s(z) + \frac{1}{4\pi\epsilon j\omega} \int_0^L \frac{dI_a(z')}{dz'} [g_1(z, z') + g_2(z, z')] dz' = 0 \quad (162)$$

By the delta-function like property as shown in Figure 2.29, an approximation to Telegrapher's equation in Agrawal's form for antenna-mode current is obtained as:

$$\begin{aligned} \frac{dV_a^s(z)}{dz} + j\omega L_a I_a(z) &= \frac{E_z^i(d, 0, z) + E_z^i(0, 0, z)}{2} \\ \frac{dI_a(z)}{dz} + j\omega C_a V_a^s(z) &= 0 \end{aligned} \quad (163)$$

where

$$L_a = \frac{\mu}{4\pi} \int_0^L [g_1(z, z') + g_2(z, z')] dz' \quad (164)$$

and

$$C_a = \frac{4\pi\epsilon}{\int_0^L [g_1(z, z') + g_2(z, z')] dz'} \quad (165)$$

The antenna-mode per-unit-length inductance and capacitance for a two-wire line is shown in Figure 2.32 and Figure 2.33. The line geometries are the same as before, but we should notice that the imaginary part of L_a and C_a cannot be neglected.

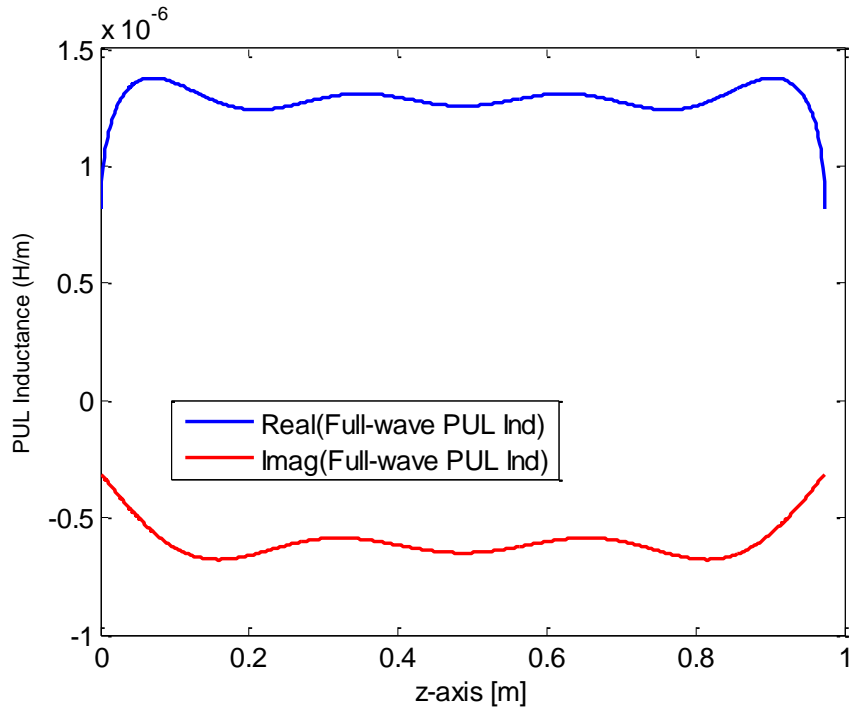


Figure 2.32. Antenna-mode Line Per-Unit-Length Inductance

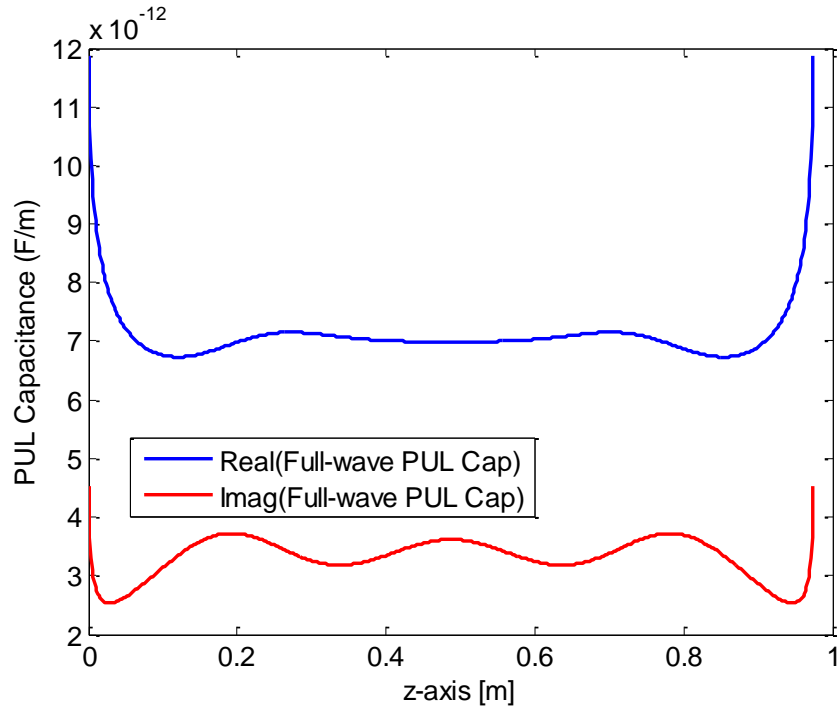


Figure 2.33. Antenna-mode Line Per-Unit-Length Capacitance

The solving of (157) or (163) could take advantage of multiple numerical methods [34], in which a SPICE solver with Modified Nodal Analysis (MNA) is a straightforward way. The transmission line is divided into many segments, and each segment can be represented as lumped elements, in left Γ , right Γ , T, or Π shape [29]. For example, the T-shape lumped circuit with distributed voltage and current source is shown in Figure 2.34.

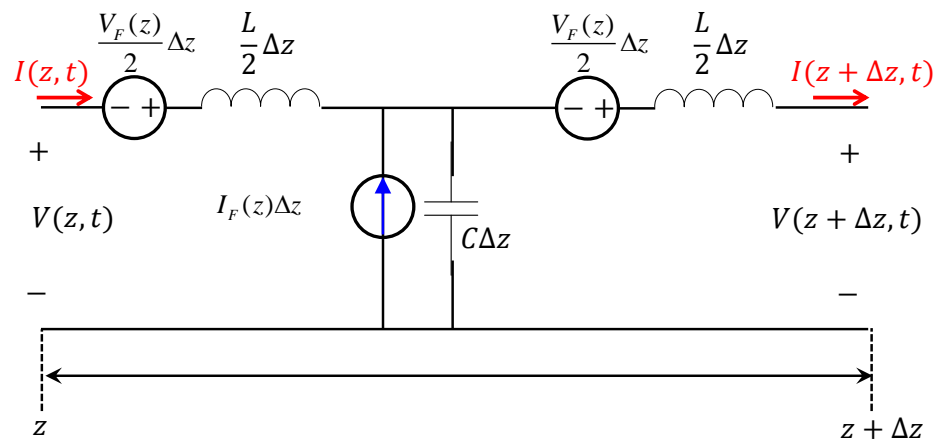


Figure 2.34. T-Shape Lumped Circuit Representation of TL

However, we would rather to know the exact solution to(155),(156) or(161),(162), than (157) or(163). A recursive process similar to [50] can be used here. Adding

$j\omega \left[\frac{\mu}{2\pi} \int_0^L (g_1(z, z') - g_2(z, z')) dz' \right] I_{\text{u}}(z)$ to both side of (155) and with minor

manipulation, one obtain

$$\begin{aligned} & \frac{d}{dz} V^S(z) + j\omega \left[\frac{\mu}{2\pi} \int_0^L (g_1(z, z') - g_2(z, z')) dz' \right] I_{\text{u}}(z) \\ &= E_z^i(d, 0, z) - E_z^i(0, 0, z) \\ &+ j\omega \frac{\mu}{2\pi} \left[I_{\text{u}}(z) \int_0^L (g_1(z, z') - g_2(z, z')) dz' - \int_0^L I_{\text{u}}(z') (g_1(z, z') - g_2(z, z')) dz' \right] \end{aligned} \quad (166)$$

Substitute (158) into(166), we get

$$\frac{d}{dz} V^S(z) + j\omega L_{\text{u}}(z) I_{\text{u}}(z) = E_z^i(d, 0, z) - E_z^i(0, 0, z) + j\omega \frac{\mu}{2\pi} \bar{D}_{\text{u}} \{I_{\text{u}}(z)\} \quad (167)$$

where

$$\bar{D}_{\text{u}} \{I_{\text{u}}(z)\} = \frac{2\pi}{\mu} I_{\text{u}}(z) L_{\text{u}}(z) - \int_0^L I_{\text{u}}(z') (g_1(z, z') - g_2(z, z')) dz' \quad (168)$$

Adding $\frac{dI_{\text{u}}(z)}{dz} \int_0^L (g_1(z, z') - g_2(z, z')) dz'$ to both side of (156), one obtain

$$\begin{aligned} & \frac{dI_{\text{u}}(z)}{dz} + j\omega \frac{2\pi\epsilon}{\int_0^L (g_1(z, z') - g_2(z, z')) dz'} V^S(z) \\ &= \frac{dI_{\text{u}}(z)}{dz} - \frac{\int_0^L \frac{dI_{\text{u}}(z')}{dz'} (g_1(z, z') - g_2(z, z')) dz'}{\int_0^L (g_1(z, z') - g_2(z, z')) dz'} \end{aligned} \quad (169)$$

Substitute (159) into(169), we get

$$\frac{dI_{\text{u}}(z)}{dz} + j\omega C_{\text{u}}(z) V^S(z) = \bar{E}_{\text{u}} \{I_{\text{u}}(z)\} \quad (170)$$

where

$$\bar{E}_{\text{u}} \{I_{\text{u}}(z)\} = \frac{dI_{\text{u}}(z)}{dz} - \frac{\int_0^L \frac{dI_{\text{u}}(z')}{dz'} (g_1(z, z') - g_2(z, z')) dz'}{\frac{2\pi\epsilon}{C_{\text{u}}(z)}} \quad (171)$$

Rewrite (167)and(170),

$$\begin{aligned}\frac{d}{dz}V^S(z) + j\omega L_{\text{tl}}(z)I_{\text{tl}}(z) &= E_z^i(d, 0, z) - E_z^i(0, 0, z) + j\omega \frac{\mu}{2\pi} \bar{D}_{\text{tl}} \{I_{\text{tl}}(z)\} \\ \frac{d}{dz}I_{\text{tl}}(z) + j\omega C_{\text{tl}}(z)V^S(z) &= \bar{E}_{\text{tl}} \{I_{\text{tl}}(z)\}\end{aligned}\quad (172)$$

The solutions to (172) are a series expansion based on perturbation theory [50]

$$\begin{aligned}V^S(z) &= V_{(0)}^S(z) + V_{(1)}^S(z) + V_{(2)}^S(z) + \dots \\ I_{\text{tl}}(z) &= I_{\text{tl}(0)}(z) + I_{\text{tl}(1)}(z) + I_{\text{tl}(2)}(z) + \dots\end{aligned}\quad (173)$$

The initial current and scattered voltage is obtained from the incident field by

(157)

$$\begin{aligned}\frac{d}{dz}V_{(0)}^S(z) + j\omega L_{\text{tl}}(z)I_{\text{tl}(0)}(z) &= E_z^i(d, 0, z) - E_z^i(0, 0, z) \\ \frac{d}{dz}I_{\text{tl}(0)}(z) + j\omega C_{\text{tl}}(z)V_{(0)}^S(z) &= 0\end{aligned}\quad (174)$$

The current and scattered voltage perturbations are then obtained from previous ones by

$$\begin{aligned}\frac{d}{dz}V_{(n)}^S(z) + j\omega L_{\text{tl}}(z)I_{\text{tl}(n)}(z) &= j\omega \frac{\mu}{2\pi} \bar{D}_{\text{tl}} \{I_{\text{tl}(n-1)}(z)\} \\ \frac{d}{dz}I_{\text{tl}(n)}(z) + j\omega C_{\text{tl}}(z)V_{(n)}^S(z) &= \bar{E}_{\text{tl}} \{I_{\text{tl}(n-1)}(z)\}\end{aligned}\quad (175)$$

Similarly for antenna-mode current, the exact solution should be obtained by recursively solving

$$\begin{aligned}\frac{d}{dz}V^S(z) + j\omega L_a(z)I_a(z) &= \frac{E_z^i(d, 0, z) + E_z^i(0, 0, z)}{2} + j\omega \frac{\mu}{4\pi} \bar{D}_a \{I_a(z)\} \\ \frac{d}{dz}I_a(z) + j\omega C_a(z)V^S(z) &= \bar{E}_a \{I_a(z)\}\end{aligned}\quad (176)$$

where

$$\bar{D}_a \{I_a(z)\} = \frac{4\pi}{\mu} I_a(z) L_a(z) - \int_0^L I_a(z') (g_1(z, z') + g_2(z, z')) dz' \quad (177)$$

$$\bar{E}_a \{I_a(z)\} = \frac{dI_a(z)}{dz} - \frac{\int_0^L \frac{dI_a(z')}{dz'} (g_1(z, z') + g_2(z, z')) dz'}{\frac{4\pi\epsilon}{C_a(z)}} \quad (178)$$

The initial current and scattered voltage is obtained from the incident field by
(163)

$$\begin{aligned} \frac{d}{dz} V_{(0)}^S(z) + j\omega L_a(z) I_{a(0)}(z) &= \frac{E_z^i(d, 0, z) + E_z^i(0, 0, z)}{2} \\ \frac{d}{dz} I_{a(0)}(z) + j\omega C_a(z) V_{(0)}^S(z) &= 0 \end{aligned} \quad (179)$$

The current and scattered voltage perturbations are then obtained from previous ones by

$$\begin{aligned} \frac{d}{dz} V_{(n)}^S(z) + j\omega L_a(z) I_{a(n)}(z) &= j\omega \frac{\mu}{2\pi} \bar{D}_a \{ I_{a(n-1)}(z) \} \\ \frac{d}{dz} I_{a(n)}(z) + j\omega C_a(z) V_{(n)}^S(z) &= \bar{E}_a \{ I_{a(n-1)}(z) \} \end{aligned} \quad (180)$$

A test case was used to check the antenna mode current on a two wire TL excited by an external plane wave, as shown in Figure 2.35. The E-field is along x-direction, and therefore, no TL-mode but antenna-mode current shall be illuminated.

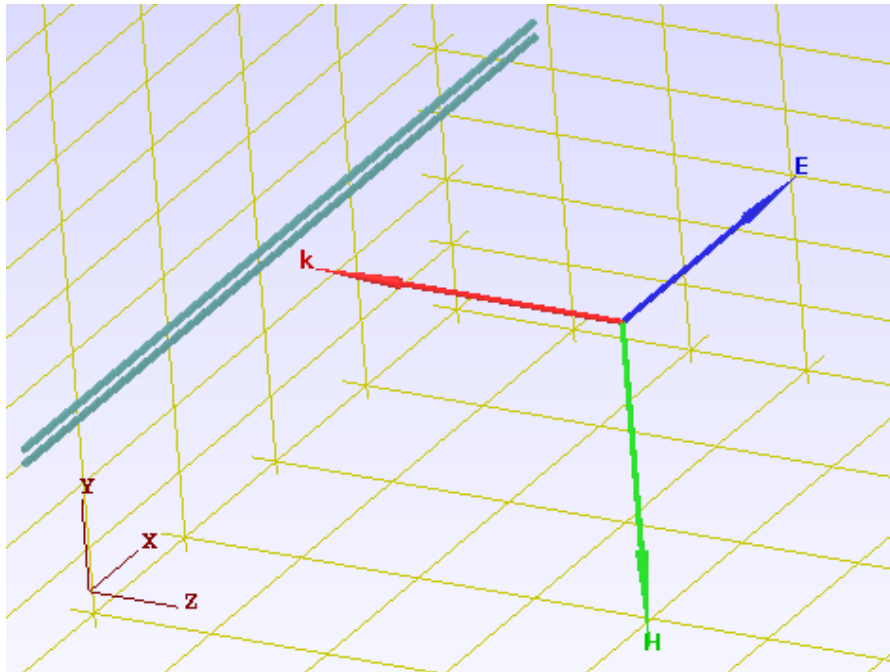


Figure 2.35. Plane Wave Excitation onto an Open Loaded Two-Wire TL

The line parameters in 1st test case are the same as before, with open load on both ends. As in Figure 2.36, the results show that even for transmission line structure with electrically short cross-section, the antenna-mode current could be much larger than TL-mode current (for this special test case, TL-mode current is zero). It took more iteration for antenna-mode current to converge than TL-mode, the reason would be $g_1 - g_2$ is more like a delta function compared to $g_1 + g_2$, as shown in Figure 2.29.

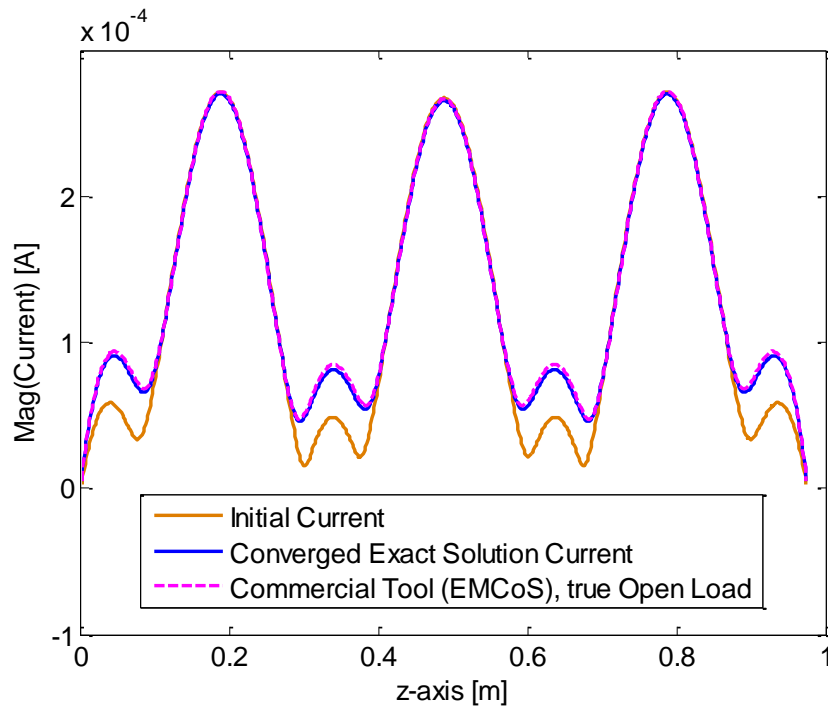


Figure 2.36. Magnitude Comparison of Antenna-mode Current

2.5.3. Dealing with TL Terminations. For TL terminations, the total voltage and total current should satisfy KVL at $z=0$ and $z=L$. With the direction definition in Figure 2.37, we have

$$\begin{aligned} V^T(0) &= -Z_A I(0) \\ V^T(L) &= Z_B I(L) \end{aligned} \quad (181)$$

where $V^T(z)$ is the total voltage at position z , and is defined as

$$\begin{aligned}
V^T(z) &= -\int_0^d E_x^{tot}(x, 0, z) dx \\
&= -\int_0^d (E_x^{sct}(x, 0, z) + E_x^i(x, 0, z)) dx \\
&= V^S(z) - \int_0^d E_x^i(x, 0, z) dx
\end{aligned} \tag{182}$$

where $V^S(z)$ is the scattered voltage defined as

$$V^S(z) = -\int_0^d E_x^{sct}(x, 0, z) dx \tag{183}$$



Figure 2.37. Boundary Conditions in Total Voltage Form

Substitution of (182) into (181) gives the boundary conditions in scattered voltage form (Agrawal's model) as in (184). And the equivalent circuit representation is shown in Figure 2.38.

$$\begin{aligned}
V^S(0) &= -Z_A I(0) + \int_0^d E_x^i(x, 0, 0) dx \\
V^S(L) &= Z_B I(L) + \int_0^d E_x^i(x, 0, L) dx
\end{aligned} \tag{184}$$

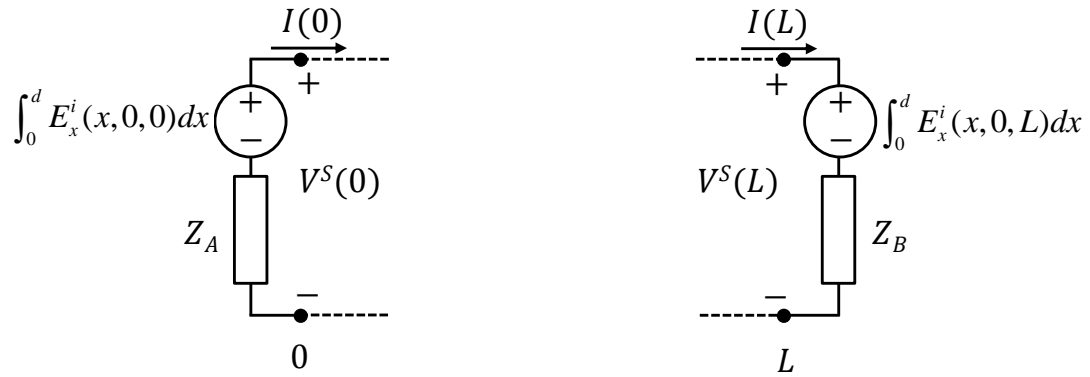


Figure 2.38. Boundary Conditions in Scattered Voltage Form

2.5.4. Antenna-Mode Current on Multi-conductor Transmission Line. For $N+1$ conductor transmission line, the relation between currents can be written as:

$$\begin{aligned}
 I_N(z) &= I_a(z) + I_{\text{d}}^N(z) \\
 &\vdots \\
 I_1(z) &= I_a(z) + I_{\text{d}}^1(z) \\
 I_0(z) &= I_a(z) - [I_{\text{d}}^1(z) + I_{\text{d}}^2(z) + \cdots + I_{\text{d}}^N(z)]
 \end{aligned} \tag{185}$$

where the antenna-mode current is defined as

$$I_a(z) = \frac{I_0(z) + I_1(z) + \cdots + I_N(z)}{N+1} \tag{186}$$

The extension from 2-wire TL to MTL will be future work.

2.6. MULTI-SCATTERING METHOD

When calculating cables with surface environment inside a vehicle by MoM, cables are generally situated very close to metallic surfaces. Therefore, the necessary discretization of the metal ground underneath cables has to be characterized by small surface patches [35], which introduces large computational burden. Combining MTL with MoM is a solution to overcome this difficulty. Many literatures have proposed the hybrid method of MTL with full wave 3D EM solver [35]-[41]. The fields in the vicinity of cables are first calculated in the absence of cables, and then the transmission line theory with incident field is applied to calculate the load response of cables. The transmission line network is either represented as an equivalent lumped circuit for SPICE

analysis, or the load response is analytically calculated by BLT (Baum, Liu, Tesche) equation [42].

The above literatures all uses a one way approach without considering field reflection (scattering) from cable back to the surface environment. Then an iterative approach was proposed to consider the multi-reflection between MTL and MoM region [43]. However, the radiation calculated in that paper didn't include the antenna mode current. To include the antenna mode current (the radiation effect from transmission line), the full-wave transmission line concept was proposed [44]-[49]. These papers derive the complete transmission line Telegrapher's Equation from the thin wire (or thick wire) EFIE formulation, and obtain the equivalent per-unit-length RLGC for antenna mode.

Some iterative approaches then calculate the field coupling to multi-conductor transmission lines in presence of complex structures, without neglecting the antenna mode current [50]-0. The ultimate source in this approach is the external field that illuminates the transmission line. The iteration starts from quasi-static solution with incident field excitation, by neglecting the retardation terms first, and then includes the non-static effect introduced by complex environment iteratively. This approach is based on perturbation theory, provided that the quasi-static current dominates.

2.6.1. Multi-Scattering by Pure MoM. If the ultimate source is the discrete voltage source applied on a transmission line, the problem can be of course solved by full-wave MoM approach. A multi-scattering approach can also be used. First consider the field caused by transmission line in the absence of complex environment as $E_{Wire2Surf}^{(0)}$, and then the scattered field by surface environment ($E_{Surf2Wire}^{(0)}$) can be calculated by MoM in the absence of wire structures. The field $E_{Surf2Wire}^{(0)}$ in turn illuminates the scattered field by wires ($E_{Wire2Surf}^{(1)}$). And the field $E_{Wire2Surf}^{(1)}$ in turn illuminates the surface for scattered field $E_{Surf2Wire}^{(1)}$ back to wires, etc. The flowchart of this multi-scattering method is shown in Figure 2.39, starting with $n=0$.

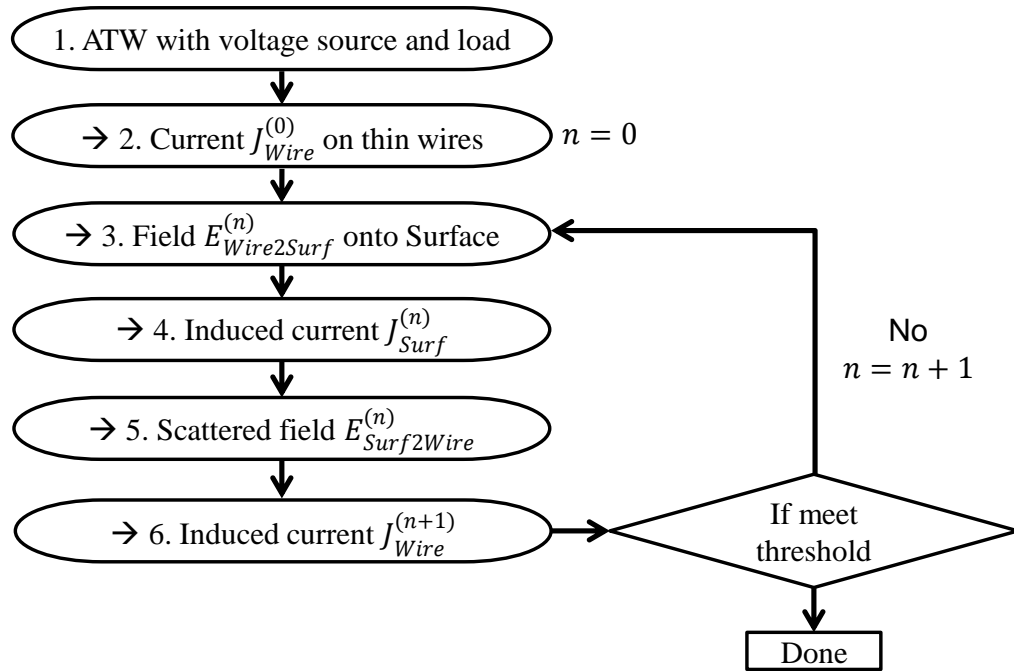


Figure 2.39. Flowchart of Multi-Scattering Method by Pure MoM

While multi-scattering approach represents the physics of field reflection, an alternative way to solve the MoM equations presents its mathematical meaning. The total MoM matrix equation including wire and surface structures is

$$\begin{bmatrix} Z_{ww} & Z_{ws} \\ Z_{sw} & Z_{ss} \end{bmatrix} \begin{bmatrix} I_w \\ I_s \end{bmatrix} = \begin{bmatrix} V_w \\ 0 \end{bmatrix} \quad (187)$$

which is equivalent to

$$Z_{ww}I_w + Z_{ws}I_s = V_w \quad (188)$$

$$Z_{sw}I_w + Z_{ss}I_s = 0 \quad (189)$$

The multi-scattering approach is like iteratively solving (187) for I_w by firstly assuming $I_s^{(0)} = 0$. From (188), with $n = 0$,

$$I_w^{(n)} = Z_{ww}^{-1} (V_w - Z_{ws}I_s^{(n)}) \quad (190)$$

Then, from (189), with $n = 0$,

$$I_s^{(n+1)} = Z_{ss}^{-1} (-Z_{sw}I_w^{(n)}) \quad (191)$$

Then, with $n = n + 1$, the solving process goes back to (190) for iteration. The total current on wires is

$$I_w = I_w^{(0)} + I_w^{(1)} + \dots \quad (192)$$

A two wire transmission line with a slotted plane environment is used as a test case to check the multi-scattering process. It is shown that one iteration is enough to reach a fairly good agreement with full-wave solution by MoM, as shown in Figure 2.40 and Figure 2.41.

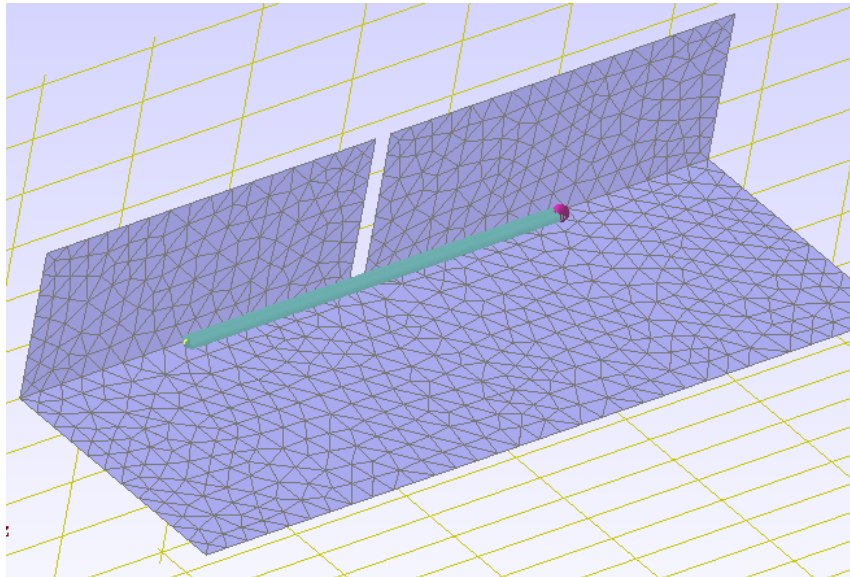


Figure 2.40. Test Structure For Validating Multi-Scattering Approach

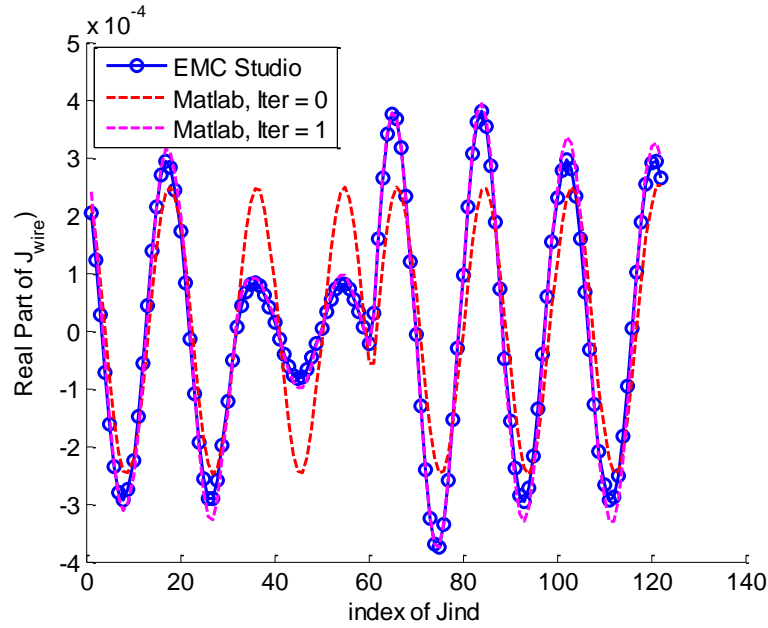


Figure 2.41. Current Comparison of Multi-Scattering And Full-Wave Approach

2.6.2. Multi-Scattering by Hybrid of MTL and MoM. The wire region can be modeled by transmission line theory, if the wires are transmission-line-like structures. In this multi-scattering approach, both the TL- and antenna- mode current on wires illuminated by external (both incident and reflected) fields has to be evaluated properly.

At first, the current on TL due to the discrete voltage source is calculated by conventional TL theory, for example, by a SPICE solver, in the absence of complex environment, and this gives the field $E_{Wire2Surf}^{(0)}$. Then the induced current $J_{Surf}^{(0)}$ on surface structure in the absence of TL is calculated by MoM, and is further used to calculate the scattered field $E_{Surf2Wire}^{(0)}$, by the algorithm in Section 2.3.2. The field $E_{Surf2Wire}^{(0)}$ in turn illuminates both the TL- and antenna-mode currents on the transmission line by TL theory discussed in Section 2.5. These induced TL- and antenna-mode current again gives the field $E_{Wire2Surf}^{(1)}$ back to surface. And the field $E_{Wire2Surf}^{(1)}$ in turn illuminates the surface structure for scattered field $E_{Surf2Wire}^{(1)}$ back to wires, and so on. The flowchart of this hybrid multi-scattering method is shown in Figure 2.42, starting with $n=0$.

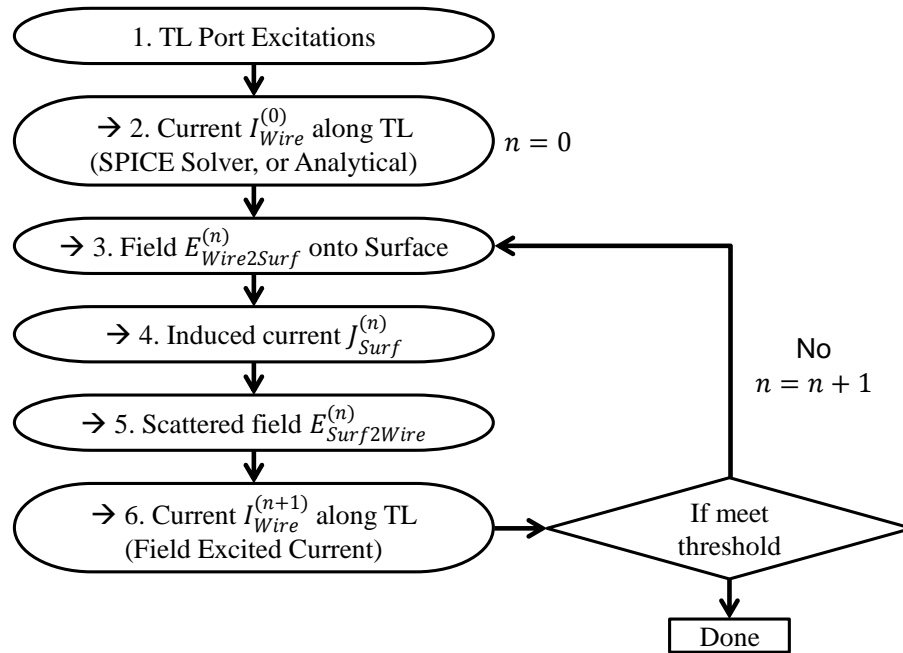


Figure 2.42. Flowchart of Multi-Scattering Method by Hybrid of MTL and MoM

The process can be explained by the example shown in Figure 2.40. The initial current $I_{Wire}^{(0)}$ can be obtained by either T-shape equivalent circuit with MNA, or the analytical equations. A comparison of initial current is shown in Figure 2.43.

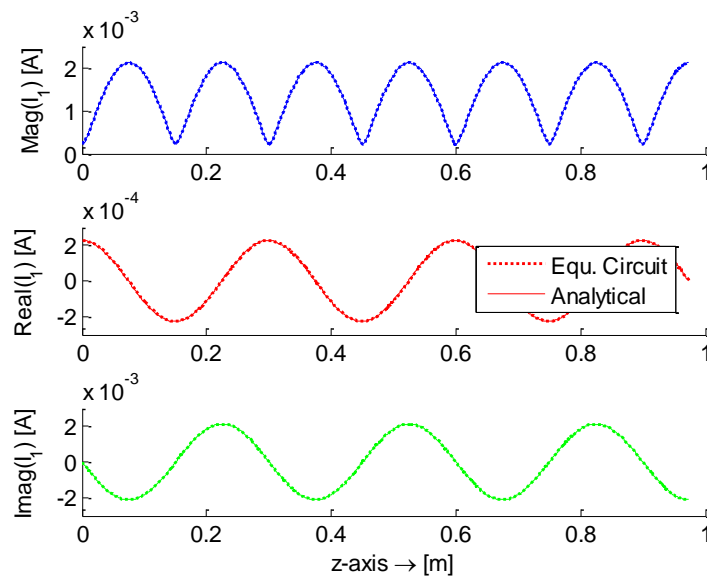


Figure 2.43. Initial Current along Wire-1

The initial current $I_{Wire}^{(0)}$ is then used as an impressed current source to calculate the induced surface current density $J_{Surf}^{(0)}$ on surface, as shown in Figure 2.44, and further scattered field $E_{Surf2Wire}^{(0)}$ at wire surface locations, in the absence of the physical wire structure. A comparison of $E_{Surf2Wire}^{(0)}$ is shown in Figure 2.45.

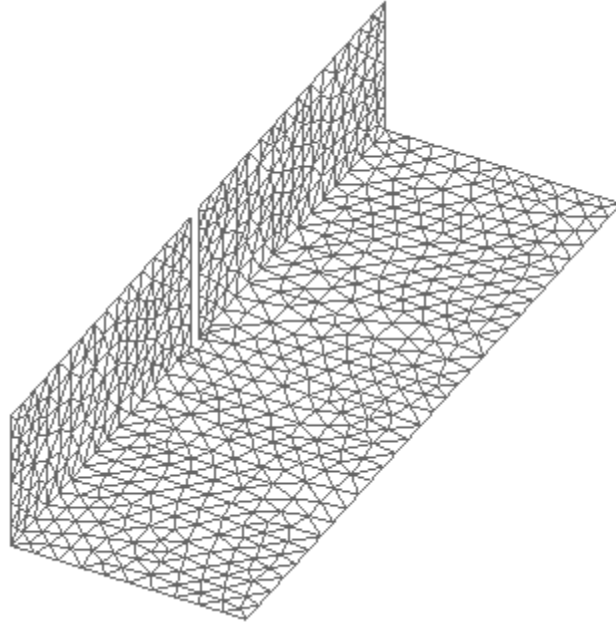


Figure 2.44. Calculate Induced Surface Current in the Absence of Wires

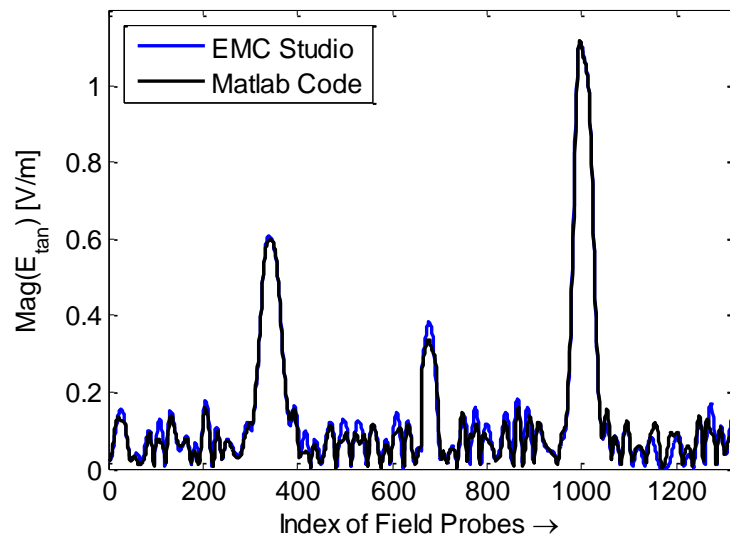


Figure 2.45. The 1st Scattered E-field along Wire Surface

The tangential component of $E_{Surf\ 2Wire}^{(0)}$ will illuminate both TL- and antenna-mode current on wires, which can be evaluated as in Section 2.5. The evaluation of TL-mode current converges very fast. The initial approximation by Equation (174) is already good enough, and after only one correction by Equation (175), the result has converged, as shown in Figure 2.46.

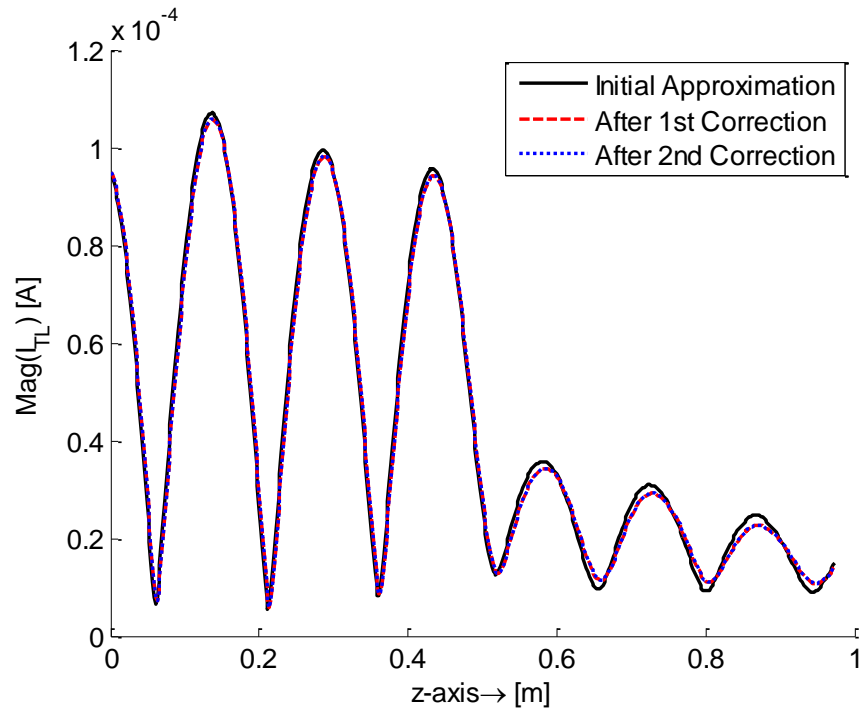


Figure 2.46. Convergence of TL-mode Current due to External Field

The evaluation of antenna-mode current does not converge that fast. After 5 corrections, the result converges, as shown in Figure 2.47. The different convergence speed for TL- and antenna-mode is again because $g_1 - g_2$ is much sharper, and more like a delta function compared to $g_1 + g_2$, as shown in Figure 2.29. The comparison between the induced TL- and antenna-mode current is shown from Figure 2.48 to Figure 2.50. Notice that antenna-mode current is zero at two ends, while TL-mode current is not (because of the 50Ω loads). The current $I_{Wire}^{(1)}$ is just the sum of both TL- and antenna-mode current. After several scattering, the total current on wires is just the sum of all currents.

$$I_{Wire}(z) = I_{Wire}^{(0)}(z) + I_{Wire}^{(1)}(z) + I_{Wire}^{(2)}(z) + \dots \quad (193)$$

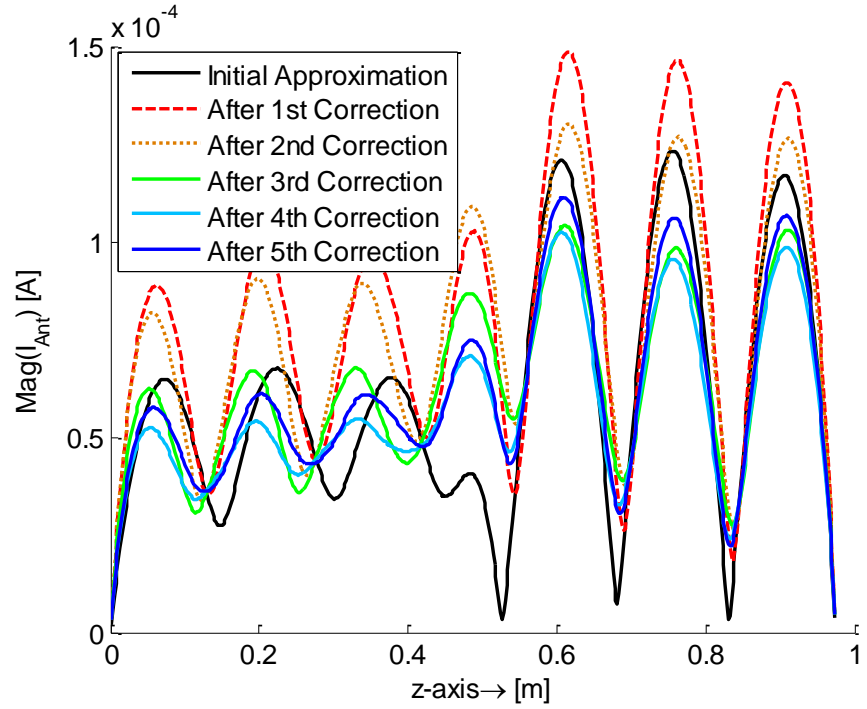


Figure 2.47. Convergence of antenna-mode Current due to External Field

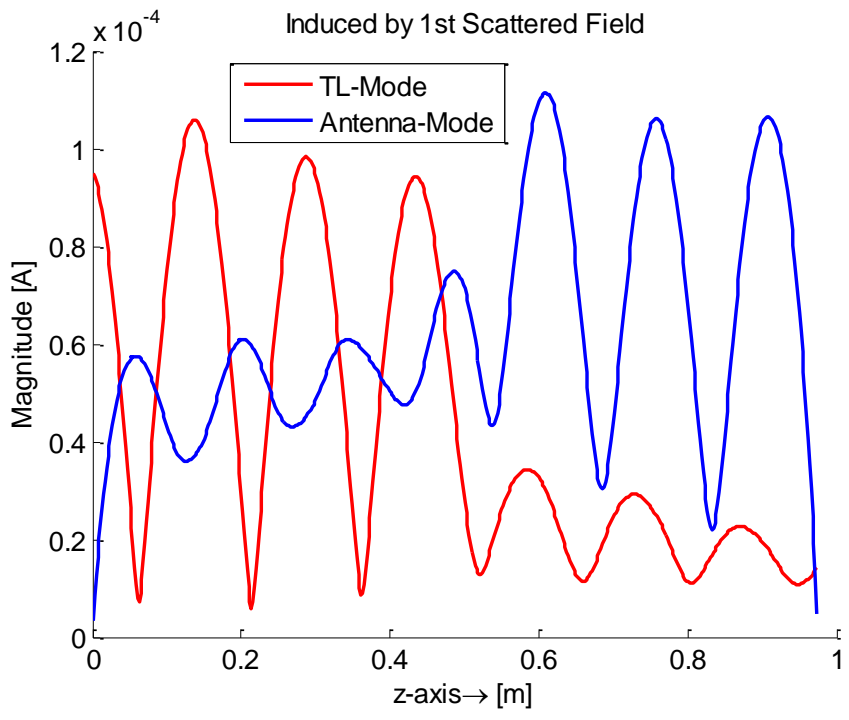


Figure 2.48. Comparison of TL- and Antenna-Mode Current in 1st Scattering

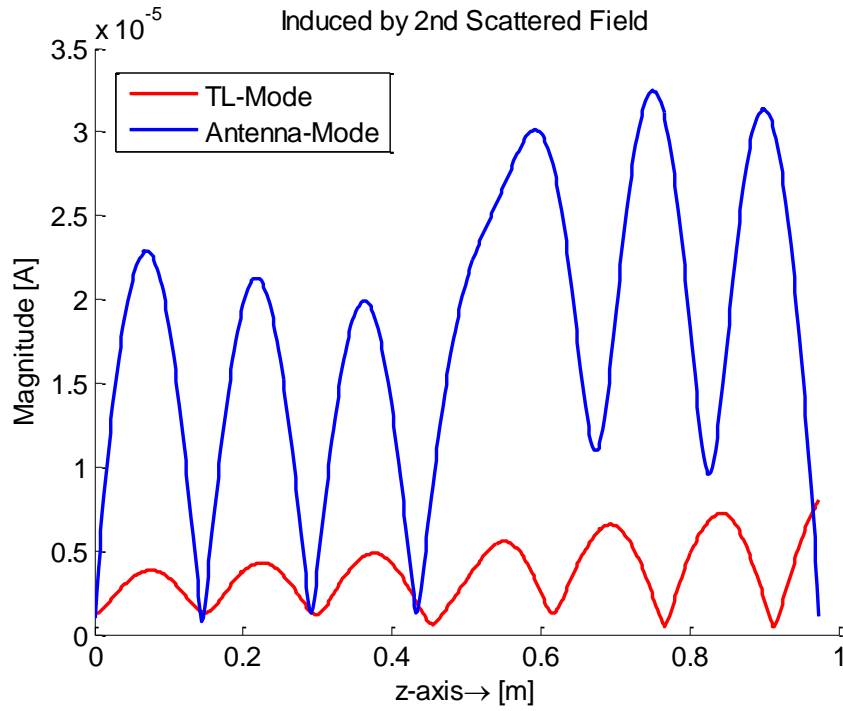


Figure 2.49. Comparison of TL- and Antenna-Mode Current in 2nd Scattering

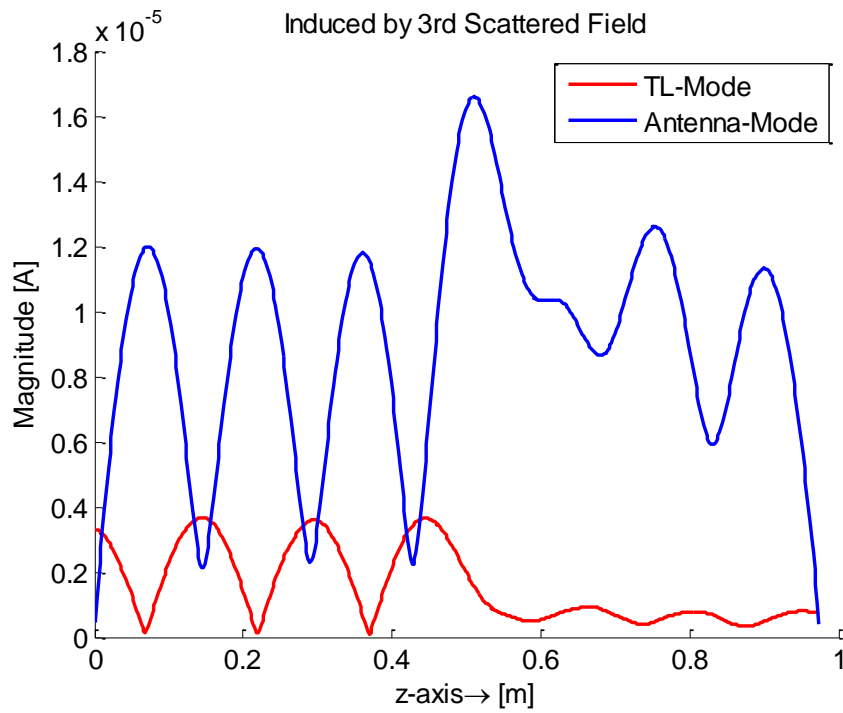


Figure 2.50. Comparison of TL- and Antenna-Mode Current in 3rd Scattering

The total current on wires compared with the Nodal MoM result is shown below from Figure 2.51 to Figure 2.54. After only one scattering, the current value is already close to the “exact” solution.

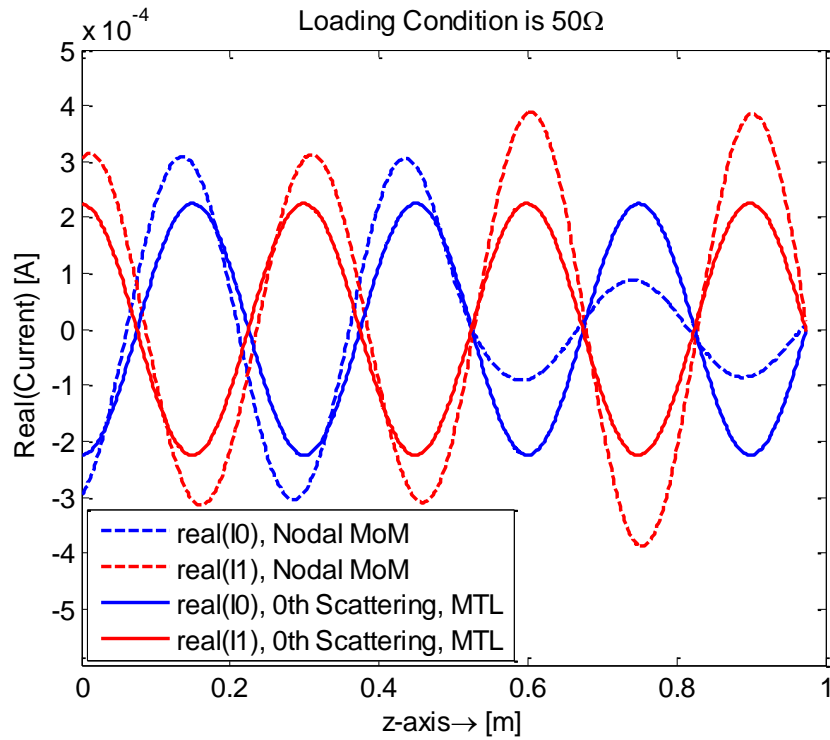


Figure 2.51. Total Current Convergence, 0th Scattering

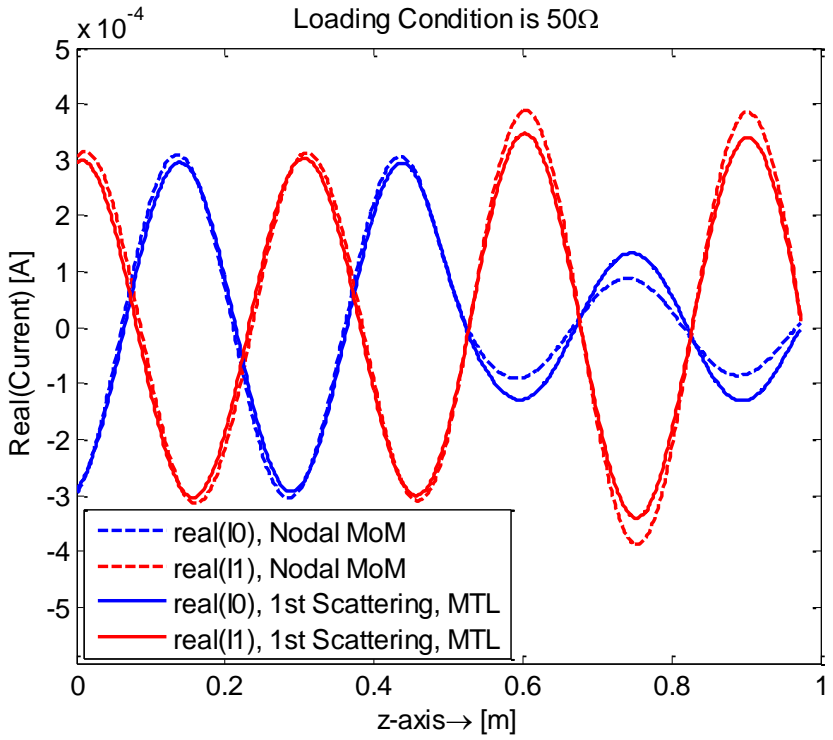


Figure 2.52. Total Current Convergence, 1st Scattering

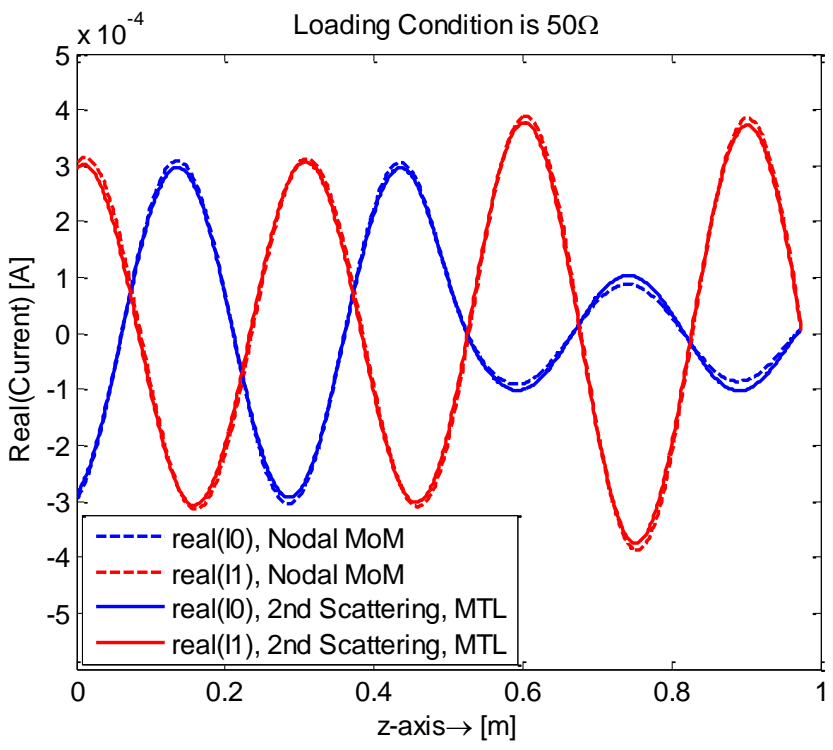


Figure 2.53. Total Current Convergence, 2nd Scattering

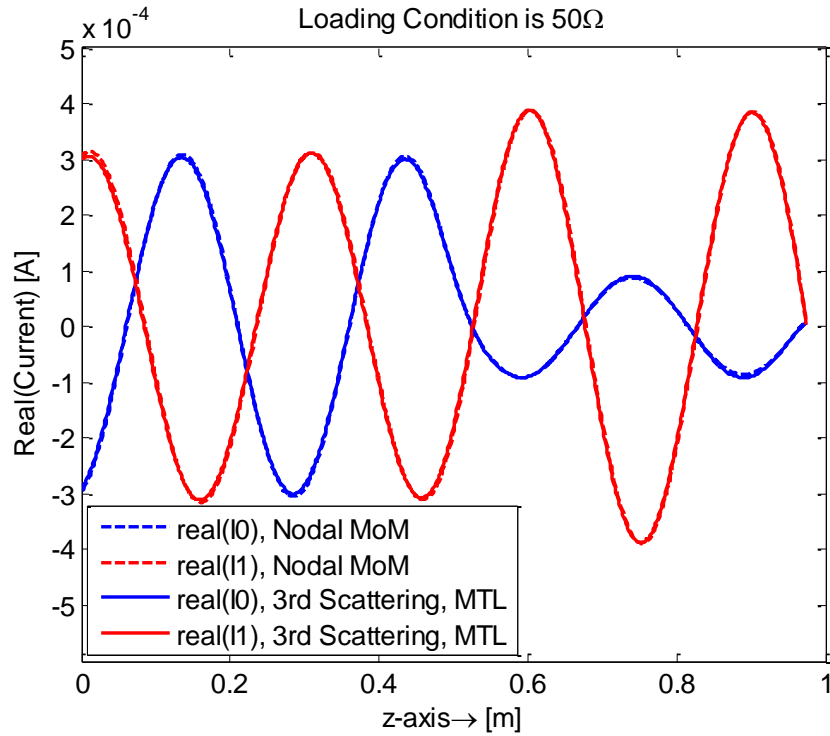


Figure 2.54. Total Current Convergence, 3rd Scattering

2.7. CONCLUSION

A multi-scattering approach by the hybrid of MTL theory and MoM method has been proposed. The current through a two-conductor transmission line can be decomposed into TL- and antenna-mode. Each mode can be evaluated by an equivalent SPICE circuit method recursively. The results show that after a few scattering between the thin wire and surface structures, converge to the “exact” solution can be achieved.

3. TSV MODELING USING MODAL BASIS FUNCTIONS

3.1. INTRODUCTION

To meet the continuously-growing needs for system integration and high density, three-dimensional integration to create multilayer chips (3D ICs) becomes increasingly important, where through-silicon via (TSV) is an enabling technology that provides connectivity between active layers[56], [57]. Understanding the electrical performance of TSVs is critical for addressing the signal/power integrity and interference issues in 3D ICs. Several approaches to model the admittance/impedance of TSVs have been proposed, including full-wave numerical simulations [58], empirical equations [59], and equivalent circuit models [60]-[63]. Ordinary full-wave approaches are accurate, but can be slow and memory-consuming especially when the number of TSVs is large in simulation. Empirical equations can provide good estimations acceptable for engineering applications, but lack of rigorous derivation. Equivalent circuit models can be constructed based on different levels of assumptions and simplifications. Most of the empirical equations and equivalent circuit models only work for a pair of TSVs.

To study a TSV array, an improved full-wave method using the method of moments (MoM) and cylindrical modal basis functions [66]-[69] has been proposed. With the modal basis functions, TSVs do not need to be discretized into mesh cells. In cylindrical coordinate, the integral equations involving the modal basis can be easily calculated analytically. Also, because only a small number of the modal basis functions are needed, the number of unknowns is significantly reduced [65]. Thus the method is very efficient in handling a large number of TSVs.

A similar idea is adopted in this paper to compute the admittance matrix of TSVs, with a different while simpler formulation. The silicon dioxide layers in the geometry are equivalently modeled with bound charge, instead of the polarization current in [66]-[69]. Then, the potentials of TSVs can be simply related to the free charge on the TSV surfaces and the bound charge due to the silicon dioxide layers, through a known Green's function in a homogeneous silicon medium. By further enforcing the boundary condition at the interface surfaces between the silicon dioxide and the silicon regions, a matrix equation is established where the admittance matrix of the TSVs can be extracted.

Due to the high permittivity and resistivity of the doped silicon substrate, a 3D TSV structure, although very short in length, can be simplified as a 2D quasi-static transmission line. Thus, the proposed approach in this work is similar to the capacitance calculation of a dielectric coated transmission line system in [65]. However, Galerkin's method is introduced instead of the simple point-matching scheme used in [65]. As a result, reciprocity is automatically enforced in the extracted admittance matrix. It needs to be pointed out that the MOS effect on the admittance matrix of TSVs is neglected in this work.

3.2. FORMULATION

Consider the problem of N TSVs with silicon dioxide coatings as shown in Figure 3.1. Since the geometry can be approximately modeled as a multi-conductor transmission line as discussed earlier, a 2D problem is formulated herein. The equivalent bound-charge approach as in [65] is adopted. In other words, the silicon dioxide coatings are replaced with the silicon substrate. To make the problem equivalent, bound charge distributions need to be introduced at the SiO₂-Si interface. The same amount of bound charge but in the opposite sign needs to be introduced on the surface of each corresponding TSV, in addition to the free charge there.

The electric potential at an arbitrary point p is contributed by all the free and bound charge distributions. In other words, in the global cylindrical coordinate system,

$$\phi(\vec{\rho}) = \sum_{j=1}^N \int_{S_j^c + S_j^i} \sigma(\vec{\rho}') G^\phi(\vec{\rho}, \vec{\rho}') d\rho' \quad (194)$$

where $\vec{\rho}$ and $\vec{\rho}'$ are the position vectors of the field and source points, respectively; G^ϕ is the Green's function for the scalar potential in the homogeneous silicon medium; and, S_j^c and S_j^i are the conductor and the SiO₂-Si interface surfaces associated with TSV j, respectively. The charge density $\sigma(\vec{\rho}')$ at the source point can be further expanded as

$$\begin{aligned}\sigma(\bar{\rho}^j) &= \sum_{k=1}^M \alpha_k^j f_k^j(\bar{\rho}^j), & \text{if } \bar{\rho}^j \in S_j^c \\ \sigma(\bar{\rho}^j) &= \sum_{k=1}^M \beta_k^j g_k^j(\bar{\rho}^j), & \text{if } \bar{\rho}^j \in S_j^i\end{aligned}\quad (195)$$

where f_k^j and g_k^j are the k^{th} basis functions on the conductor and the SiO₂-Si interface associated with TSV j , respectively; α_k^j and β_k^j are their coefficients. As discussed in [65], the basis functions are chosen to be the axial harmonic expansion functions to reduce the number of unknowns. Specifically, they are

$$\begin{aligned}f_k^j, g_k^j &= 1, & k = 1 \\ f_k^j, g_k^j &= \cos\left(\frac{k\theta_j}{2}\right), & k > 1 \text{ \& even} \\ f_k^j, g_k^j &= \sin\left(\frac{(k-1)\theta_j}{2}\right), & k > 1 \text{ \& odd}\end{aligned}\quad (196)$$

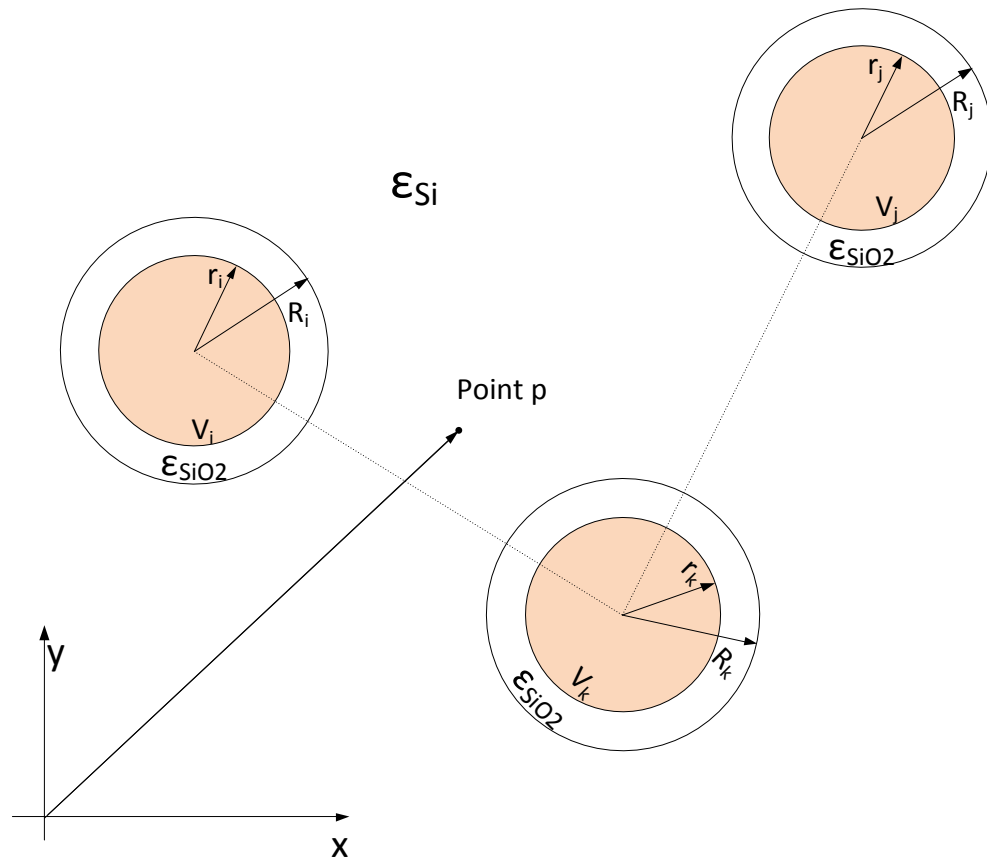


Figure 3.1. A Cross-Sectional View of A TSV Array

The angle θ_j is defined in the local cylindrical coordinate system centered at TSV j as shown in Figure 3.2. Notice that M in (195) is the total number of the basis functions used in the expansions, which is an odd number.

Substituting (195) into (194) results in

$$\begin{aligned}\phi(\vec{\rho}) &= \sum_{j=1}^N \sum_{k=1}^M \alpha_k^j \int_{S_j^c} f_k^j(\vec{\rho}') G^\phi(\vec{\rho}, \vec{\rho}') d\vec{\rho}' + \sum_{j=1}^N \sum_{k=1}^M \beta_k^j \int_{S_j^i} g_k^j(\vec{\rho}') G^\phi(\vec{\rho}, \vec{\rho}') d\vec{\rho}' \\ &= \sum_{n=1}^{M \times N} [a_n \varphi_n(\vec{\rho}) + b_n \varphi_n^*(\vec{\rho})]\end{aligned}\quad (197)$$

where

$$\forall n: \quad j = \text{floor}\left(\frac{n-1}{M}\right) + 1, \quad k = \text{mod}(n-1, M) + 1$$

$$a_n = \alpha_k^j$$

$$b_n = \beta_k^j$$

$$\varphi_n(\vec{\rho}) = \int_{S_j^c} f_k^j(\vec{\rho}') G^\phi(\vec{\rho}, \vec{\rho}') d\vec{\rho}'$$

$$\varphi_n^*(\vec{\rho}) = \int_{S_j^i} g_k^j(\vec{\rho}') G^\phi(\vec{\rho}, \vec{\rho}') d\vec{\rho}'$$

The term $\varphi_n^*(\vec{\rho})$ could be described using two different expressions depending on the location of the field point. Let's define $\varphi_n^*(\vec{\rho}) = \varphi_n^{*+}(\vec{\rho})$, if the field point is outside of the SiO₂-Si interface of TSV j ; and $\varphi_n^*(\vec{\rho}) = \varphi_n^{*-}(\vec{\rho})$, if the field point is inside the SiO₂-Si interface of TSV j .

Galerkin's method is then used to test (197) using the basis functions defined on the conductor surfaces. In other words,

$$\begin{aligned}\langle f_m(\vec{\rho}), \phi(\vec{\rho}) \rangle &= \sum_{n=1}^{M \times N} \left\{ a_n \langle f_m(\vec{\rho}), \varphi_n(\vec{\rho}) \rangle + b_n \langle f_m(\vec{\rho}), \varphi_n^*(\vec{\rho}) \rangle \right\} \\ m &= 1, 2, \dots, M \times N, \vec{\rho} \in S^c\end{aligned}\quad (198)$$

Equation (198) can be further written as

$$V_m = \sum_{n=1}^{M \times N} \{a_n D_{mn} + b_n D_{mn}^*\}, m = 1, 2, \dots, M \times N \quad (199)$$

where

$$\forall m: \quad j = \text{floor}\left(\frac{m-1}{M}\right) + 1, \quad k = \text{mod}(m-1, M) + 1$$

$$f_m(\vec{\rho}) = f_k^j(\vec{\rho})$$

$$\vec{\rho} \in S^c$$

$$V_m = \langle f_m(\vec{\rho}), \phi(\vec{\rho}) \rangle$$

$$D_{mn} = \langle f_m(\vec{\rho}), \varphi_n(\vec{\rho}) \rangle$$

$$D_{mn^*} = \langle f_m(\vec{\rho}), \varphi_n^*(\vec{\rho}) \rangle$$

$$= \begin{cases} \langle f_m(\vec{\rho}), \varphi_n^{*+}(\vec{\rho}) \rangle, & \text{if } \text{floor}\left(\frac{n-1}{M}\right) + 1 \neq j \\ \langle f_m(\vec{\rho}), \varphi_n^{*-}(\vec{\rho}) \rangle, & \text{if } \text{floor}\left(\frac{n-1}{M}\right) + 1 = j \end{cases}$$

The electric field at an arbitrary point p can be further obtained from the scalar potential as

$$\begin{aligned} \vec{E}(\vec{\rho}) &= -\nabla \phi(\vec{\rho}) = -\sum_{j=1}^N \int_{S_j^c + S_j^i} \sigma(\vec{\rho}') \nabla G^\phi(\vec{\rho}, \vec{\rho}') d\vec{\rho}' \\ &= -\sum_{j=1}^N \sum_{k=1}^M \alpha_k^j \int_{S_j^c} f_k^j(\vec{\rho}') \nabla G^\phi(\vec{\rho}, \vec{\rho}') d\vec{\rho}' \\ &\quad - \sum_{j=1}^N \sum_{k=1}^M \beta_k^j \int_{S_j^i} g_k^j(\vec{\rho}') \nabla G^\phi(\vec{\rho}, \vec{\rho}') d\vec{\rho}' \\ &= -\sum_{n=1}^{M \times N} \left[a_n \vec{\psi}_n(\vec{\rho}) + b_n \vec{\psi}_n^*(\vec{\rho}) \right] \end{aligned} \tag{200}$$

where

$$\forall n: \quad j = \text{floor}\left(\frac{n-1}{M}\right) + 1, \quad k = \text{mod}(n-1, M) + 1$$

$$a_n = \alpha_k^j$$

$$b_n = \beta_k^j$$

$$\vec{\psi}_n(\vec{\rho}) = \int_{S_j^c} f_k^j(\vec{\rho}') \nabla G^\phi(\vec{\rho}, \vec{\rho}') d\vec{\rho}'$$

$$\vec{\psi}_n^*(\vec{\rho}) = \int_{S_j^i} g_k^j(\vec{\rho}') \nabla G^\phi(\vec{\rho}, \vec{\rho}') d\vec{\rho}'$$

Similarly, the term $\vec{\psi}_n^*(\vec{\rho})$ could be described using two different expressions depending on the location of the field point. Let's define $\vec{\psi}_n^*(\vec{\rho}) = \vec{\psi}_n^{*+}(\vec{\rho})$, if the field

point is outside of the SiO₂-Si interface of TSV j ; and $\psi_n^*(\rho) = \psi_n^{*-}(\rho)$, if the field point is inside the SiO₂-Si interface of TSV j .

At the SiO₂-Si interface, the normal electric displacement field needs to be continuous. In other words,

$$\begin{aligned}
& \text{At } S_j^i, \\
& \varepsilon_{rb} E_{\rho_j}(\bar{\rho}^+) - \varepsilon_{r1} E_{\rho_j}(\bar{\rho}^-) = 0 \Rightarrow \\
& \sum_{n=1, \text{floor}(\frac{n-1}{M})+1 \neq j}^{M \times N} \left\{ a_n (\varepsilon_{rb} - \varepsilon_{r1}) \bar{\psi}_n(\bar{\rho}) + b_n (\varepsilon_{rb} - \varepsilon_{r1}) \bar{\psi}_n^{*+}(\bar{\rho}) \right\} \cdot \hat{\rho}_j \\
& + \sum_{n=(j-1)M+1}^{(j-1)M+M} \left\{ a_n (\varepsilon_{rb} - \varepsilon_{r1}) \bar{\psi}_n(\bar{\rho}) + b_n \left[\varepsilon_{rb} \bar{\psi}_n^{*-}(\bar{\rho}) - \varepsilon_{r1} \bar{\psi}_n^{*+}(\bar{\rho}) \right] \right\} \cdot \hat{\rho}_j \\
& = 0, \quad j = 1, 2, \dots, N, \bar{\rho} \in S_j^i
\end{aligned} \tag{201}$$

where ε_{rb} and ε_{r1} are the relative permittivity of the silicon substrate and the SiO₂ coating, respectively; $\bar{\rho}^+$ and $\bar{\rho}^-$ are the vector pointing to the outside and inside of the SiO₂-Si interface, respectively; and, $\hat{\rho}_j$ is the unit vector normal to S_j^i . To account for the loss in

the silicon substrate, ε_{rb} needs to be complex. Here, ε_{rb} is set to be $\varepsilon_{rSi} \left(1 - \frac{j\sigma}{\omega \varepsilon_0 \varepsilon_{rSi}} \right)$,

where ε_{rSi} and σ are the real-valued relative permittivity and conductivity of the silicon substrate. By testing (201) using the basis functions defined on the SiO₂-Si interface surfaces, another set of equations are obtained as

$$0 = \sum_{n=1}^{M \times N} \left\{ a_n D_{m^*n} + b_n D_{m^*n^*} \right\}, m^* = 1, 2, \dots, M \times N \tag{202}$$

where

$$\forall m: \quad j = \text{floor}\left(\frac{m-1}{M}\right) + 1, \quad k = \text{mod}(m-1, M) + 1$$

$$g_m(\vec{\rho}) = g_k^j(\vec{\rho})$$

$$\vec{\rho} \in S^i$$

$$D_{m^*n} = \left\langle g_m(\vec{\rho}), (\varepsilon_{rb} - \varepsilon_{r1}) \overrightarrow{\psi}_n(\vec{\rho}) \cdot \hat{\rho}_j \right\rangle$$

$$D_{m^*n^*} = \begin{cases} \left\langle g_m(\vec{\rho}), (\varepsilon_{rb} - \varepsilon_{r1}) \overrightarrow{\psi}_n^{*+}(\vec{\rho}) \cdot \hat{\rho}_j \right\rangle, & \text{floor}\left(\frac{n-1}{M}\right) + 1 \neq j \\ \left\langle g_m(\vec{\rho}), \varepsilon_{rb} \overrightarrow{\psi}_n^{*-}(\vec{\rho}) \cdot \rho_j - \varepsilon_{r1} \overrightarrow{\psi}_n^{*+}(\vec{\rho}) \cdot \hat{\rho}_j \right\rangle, & \text{floor}\left(\frac{n-1}{M}\right) + 1 = j \end{cases}$$

Combining (199) and (202) results in the following system matrix equation as

$$\begin{bmatrix} \overline{\mathbf{V}}_m \\ \overline{\mathbf{0}} \end{bmatrix} = \begin{bmatrix} \overline{\mathbf{D}}_{mn} & \overline{\mathbf{D}}_{mn^*} \\ \overline{\mathbf{D}}_{m^*n} & \overline{\mathbf{D}}_{m^*n^*} \end{bmatrix} \begin{bmatrix} \overline{\mathbf{a}}_n \\ \overline{\mathbf{b}}_n \end{bmatrix} = \begin{bmatrix} \overline{\mathbf{D}} \\ \overline{\mathbf{D}} \end{bmatrix} \begin{bmatrix} \overline{\mathbf{a}}_n \\ \overline{\mathbf{b}}_n \end{bmatrix} \quad (203)$$

where

$$\begin{bmatrix} \overline{\mathbf{V}}_m \\ \overline{\mathbf{0}} \end{bmatrix} = \begin{bmatrix} V_1 \\ V_2 \\ \vdots \\ \vdots \\ V_{M \times N} \end{bmatrix}, \quad \begin{bmatrix} \overline{\mathbf{0}} \end{bmatrix} = \begin{bmatrix} 0 \\ 0 \\ \vdots \\ \vdots \\ 0 \end{bmatrix}, \quad \begin{bmatrix} \overline{\mathbf{a}}_n \\ \overline{\mathbf{b}}_n \end{bmatrix} = \begin{bmatrix} a_1 \\ a_2 \\ \vdots \\ \vdots \\ a_{M \times N} \end{bmatrix}, \quad \begin{bmatrix} \overline{\mathbf{b}}_n \end{bmatrix} = \begin{bmatrix} b_1 \\ b_2 \\ \vdots \\ \vdots \\ b_{M \times N} \end{bmatrix}.$$

Specifically, when the basis functions defined in (196) are used, only the zero-order mode ($k = 1$, representing the axially uniform distribution of charge densities) contributes to the electric potentials. In other words,

$$V_m = \begin{cases} 0, & \text{if } \text{mod}(m-1, M) \neq 0 \\ 2\pi r_j \phi_j, & \text{if } \text{mod}(m-1, M) = 0, \end{cases}$$

where $j = \text{floor}\left(\frac{(m-1)}{M}\right) + 1$; ϕ_j is the potential of TSV j ; and, r_j is the radius of TSV j .

From (203), the coefficients of the charge densities can be obtained as

$$\begin{bmatrix} \overline{\mathbf{a}}_n \\ \overline{\mathbf{b}}_n \end{bmatrix} = \begin{bmatrix} \overline{\mathbf{D}}_{mn} & \overline{\mathbf{D}}_{mn^*} \\ \overline{\mathbf{D}}_{m^*n} & \overline{\mathbf{D}}_{m^*n^*} \end{bmatrix}^{-1} \begin{bmatrix} \overline{\mathbf{V}}_m \\ \overline{\mathbf{0}} \end{bmatrix} = \begin{bmatrix} \overline{\mathbf{B}}_{mn} & \overline{\mathbf{B}}_{mn^*} \\ \overline{\mathbf{B}}_{m^*n} & \overline{\mathbf{B}}_{m^*n^*} \end{bmatrix} \begin{bmatrix} \overline{\mathbf{V}}_m \\ \overline{\mathbf{0}} \end{bmatrix} \quad (204)$$

It can be easily found out that the total free charge on each TSV surface is only related to the zero-order modes as

$$\begin{aligned}
q_{if} &= \int_{S_i^c} \sum_{k=1}^M \alpha_k^i f_k^i(\vec{\rho}') d\vec{\rho}' + \int_{S_i^i} \sum_{k=1}^M \beta_k^i g_k^i(\vec{\rho}') d\vec{\rho}' \\
&= 2\pi r_i \alpha_1^i + 2\pi R_i \beta_1^i, \quad \forall i
\end{aligned} \tag{205}$$

where $2\pi r_i \alpha_1^i$ is the sum of the free and the negative bound charge on the conductor surface of TSV i ; $2\pi R_i \beta_1^i$ is the bound charge at the SiO₂-Si interface of TSV i ; and R_i is the radius of the SiO₂-Si interface of TSV i . Further combining (204) and (205) results in

$$q_{if} = (2\pi)^2 \sum_{j=1}^N \phi_j \left\{ r_i r_j \left[\overline{\overline{\mathbf{B}_{mn}}} \right]_{(i-1)M+1, (j-1)M+1} + R_i r_j \left[\overline{\overline{\mathbf{B}_{m^*n}}} \right]_{(i-1)M+1, (j-1)M+1} \right\}$$

Then, based on the charge and potential relationship, we have

$$\begin{aligned}
C_{ij} - j \frac{G_{ij}}{\omega} &= \frac{q_{if}}{\phi_j} \Big|_{\phi_k=0 \text{ if } k \neq j} \\
&= 4\pi^2 r_i r_j \left[\overline{\overline{\mathbf{B}_{mn}}} \right]_{(i-1)M+1, (j-1)M+1} + 4\pi^2 R_i r_j \left[\overline{\overline{\mathbf{B}_{m^*n}}} \right]_{(i-1)M+1, (j-1)M+1}
\end{aligned} \tag{206}$$

3.3. CALCULATION OF SYSTEM MATRIX

In the 2D case studied in this paper, the Green's function for the scalar potential in the homogenous silicon medium in (194) is [79].

$$G^\phi(\vec{\rho}, \vec{\rho}') = \frac{\ln |\vec{\rho} - \vec{\rho}'|^2}{-4\pi\epsilon_0\epsilon_{rb}} \tag{207}$$

Using the basis functions defined in (196), the electric potential terms, $\varphi_n(\vec{\rho})$ and $\varphi_n^*(\vec{\rho})$ in (197), and the electric field terms, $\vec{\psi}_n(\vec{\rho})$ and $\vec{\psi}_n^*(\vec{\rho})$ in (200), can be analytically calculated as in [65]. The closed-form expressions are listed in Table 3.1 for reference, where (ρ, θ) are the coordinates of the field point p in the local coordinate system centered at TSV j ; $j = \text{floor}(\frac{n-1}{M}) + 1$; and, $k = \text{mod}(n-1, M) + 1$.

Table 3.1. Closed-Form Expressions for Calculating Electric Field and Potential

| | $k = 1$ | $k > 1$ & even | $k > 1$ & odd |
|---------------------|---|--|--|
| φ_n | $\frac{-r_j \ln(\rho)}{\varepsilon_0 \varepsilon_{rb}}$ | $\frac{(r_j)^{\frac{k+1}{2}} \cos\left(\frac{k\theta}{2}\right)}{k \varepsilon_0 \varepsilon_{rb} (\rho)^{\frac{k}{2}}}$ | $\frac{(r_j)^{\frac{k-1}{2}+1} \sin\left(\frac{(k-1)\theta}{2}\right)}{(k-1) \varepsilon_0 \varepsilon_{rb} (\rho)^{\frac{k-1}{2}}}$ |
| φ_n^{*+} | $\frac{-R_j \ln(\rho)}{\varepsilon_0 \varepsilon_{rb}}$ | $\frac{(R_j)^{\frac{k+1}{2}} \cos\left(\frac{k\theta}{2}\right)}{k \varepsilon_0 \varepsilon_{rb} (\rho)^{\frac{k}{2}}}$ | $\frac{(R_j)^{\frac{k-1}{2}+1} \sin\left(\frac{(k-1)\theta}{2}\right)}{(k-1) \varepsilon_0 \varepsilon_{rb} (\rho)^{\frac{k-1}{2}}}$ |
| φ_n^{*-} | $\frac{-R_j \ln(R_j)}{\varepsilon_0 \varepsilon_{rb}}$ | $\frac{(\rho)^{\frac{k}{2}} \cos\left(\frac{k\theta}{2}\right)}{k \varepsilon_0 \varepsilon_{rb} (R_j)^{\frac{k-1}{2}}}$ | $\frac{(\rho)^{\frac{k-1}{2}} \sin\left(\frac{(k-1)\theta}{2}\right)}{(k-1) \varepsilon_0 \varepsilon_{rb} (R_j)^{\frac{k-1}{2}-1}}$ |
| $\vec{\psi}_n$ | $\frac{r_j}{\varepsilon_0 \varepsilon_{rb} \rho}$ | $\frac{\left(\frac{r_j}{\rho}\right)^{\frac{k+1}{2}}}{2 \varepsilon_0 \varepsilon_{rb}} \left\{ \cos\left(\frac{k\theta}{2}\right) \hat{\rho} + \sin\left(\frac{k\theta}{2}\right) \hat{\theta} \right\}$ | $\frac{\left(\frac{r_j}{\rho}\right)^{\frac{k-1}{2}+1}}{2 \varepsilon_0 \varepsilon_{rb}} \left\{ \sin\left(\frac{(k-1)\theta}{2}\right) \hat{\rho} - \cos\left(\frac{(k-1)\theta}{2}\right) \hat{\theta} \right\}$ |
| $\vec{\psi}_n^{*+}$ | $\frac{R_j}{\varepsilon_0 \varepsilon_{rb} \rho}$ | $\frac{\left(\frac{R_j}{\rho}\right)^{\frac{k+1}{2}}}{2 \varepsilon_0 \varepsilon_{rb}} \left\{ \cos\left(\frac{k\theta}{2}\right) \hat{\rho} + \sin\left(\frac{k\theta}{2}\right) \hat{\theta} \right\}$ | $\frac{\left(\frac{R_j}{\rho}\right)^{\frac{k-1}{2}+1}}{2 \varepsilon_0 \varepsilon_{rb}} \left\{ \sin\left(\frac{(k-1)\theta}{2}\right) \hat{\rho} - \cos\left(\frac{(k-1)\theta}{2}\right) \hat{\theta} \right\}$ |
| $\vec{\psi}_n^{*-}$ | 0 | $-\frac{\left(\frac{\rho}{R_j}\right)^{\frac{k-1}{2}}}{2 \varepsilon_0 \varepsilon_{rb}} \left\{ \cos\left(\frac{k\theta}{2}\right) \hat{\rho} - \sin\left(\frac{k\theta}{2}\right) \hat{\theta} \right\}$ | $-\frac{\left(\frac{\rho}{R_j}\right)^{\frac{k-1}{2}-1}}{2 \varepsilon_0 \varepsilon_{rb}} \left\{ \sin\left(\frac{(k-1)\theta}{2}\right) \hat{\rho} + \cos\left(\frac{(k-1)\theta}{2}\right) \hat{\theta} \right\}$ |

To further calculate the elements in $[\bar{\mathbf{D}}]$, the related inner products need to be evaluated in the local coordinate systems where the testing functions are defined. There are two possible cases. The testing and the basis functions involved in an element can be located in the same local coordinate system as shown in Figure 3.2, or in two different

local coordinate systems as shown in Figure 3.3. In the latter case, coordinates in one local cylindrical coordinate system need to be converted to those in another local cylindrical coordinate system. As illustrated in Figure 3.3, the coordinates (x_i, y_i) of Point p in the coordinate system centered at TSV i are related to the corresponding coordinates (ρ, θ) in the coordinate system centered at TSV j as

$$\begin{aligned}\rho &= \text{abs}\{(x_i, y_i) - (d, 0)\} \\ \theta &= \text{angle}\{(x_i, y_i) - (d, 0)\}\end{aligned}\quad (208)$$

where d is the center-to-center distance between the two TSVs.

Then, the inner products are calculated using the 1D Gaussian quadrature numerically. In other words, certain points are selected along the integration path of each 1D integral, and the weighted average value of the integrand among these points is used as the approximate result of the inner product.

After the system matrix $[\bar{\mathbf{D}}]$ is calculated, the admittance matrix of multiple TSVs, including capacitances and conductances, can be obtained from(206).

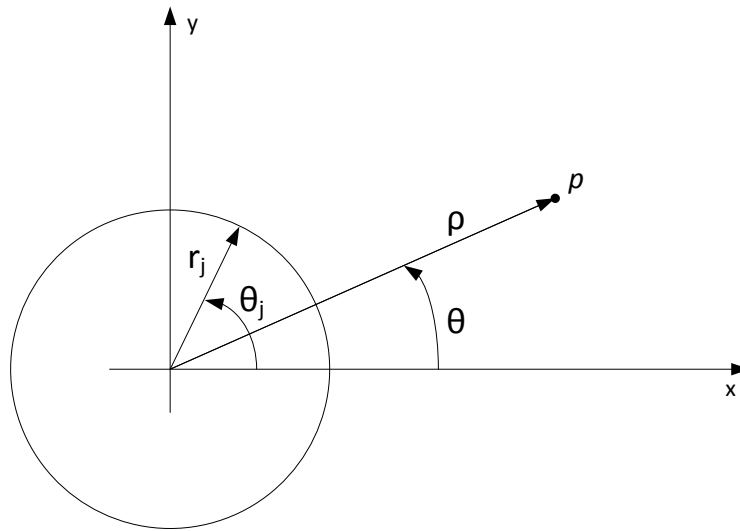


Figure 3.2. Evaluating the Matrix Element $\text{In}[\bar{\mathbf{D}}]$: Testing and Basis Functions are Located in the Same Local Coordinate System

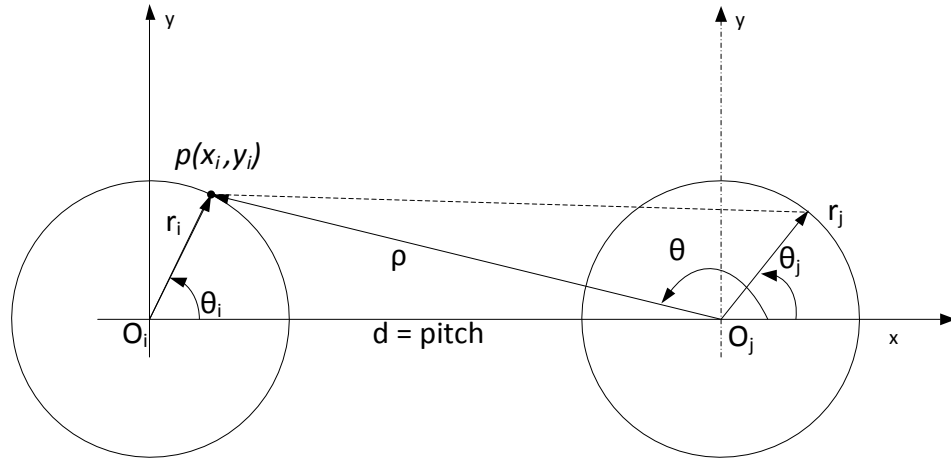


Figure 3.3. Evaluating the Matrix Element in $\overline{[\mathbf{D}]}$: Testing and Basis Functions are Located in Different Local Coordinate Systems

3.4. A TSV PAIR

A typical TSV pair is used to validate the proposed approach. The radius of each TSV is $r_{TSV} = 2.5 \mu\text{m}$, and the thickness of the silicon dioxide coating is $t_{ox} = 0.5 \mu\text{m}$. The relative permittivity of SiO_2 is $\epsilon_{r1} = 3.9$. The silicon substrate has a real relative permittivity of $\epsilon_{rSi} = 11.9$ and a resistivity of $\rho_{rSi} = 10 \Omega \cdot \text{cm}$. The total capacitance between the two TSVs is calculated from the matrix elements obtained using (206) as

$$\mathbb{C} = -C_{12} + \frac{(C_{11} + C_{12})(C_{22} + C_{12})}{C_{11} + C_{22} + 2C_{12}}, \quad (209)$$

and the total conductance is similarly determined.

First, a pitch size of $d = 15 \mu\text{m}$ was studied. The calculated capacitance and conductance values between the two TSVs agree well with the calculated values using the published equations in [56], as well as those from a commercial 2D Finite Element Method (FEM) tool (Q2D from Ansys [80]), as shown in Figure 3.4. It can be shown that the proximity effect between the two TSVs can be neglected in this case because the pitch size is relatively large, which was the assumption used in the published equations in [56].

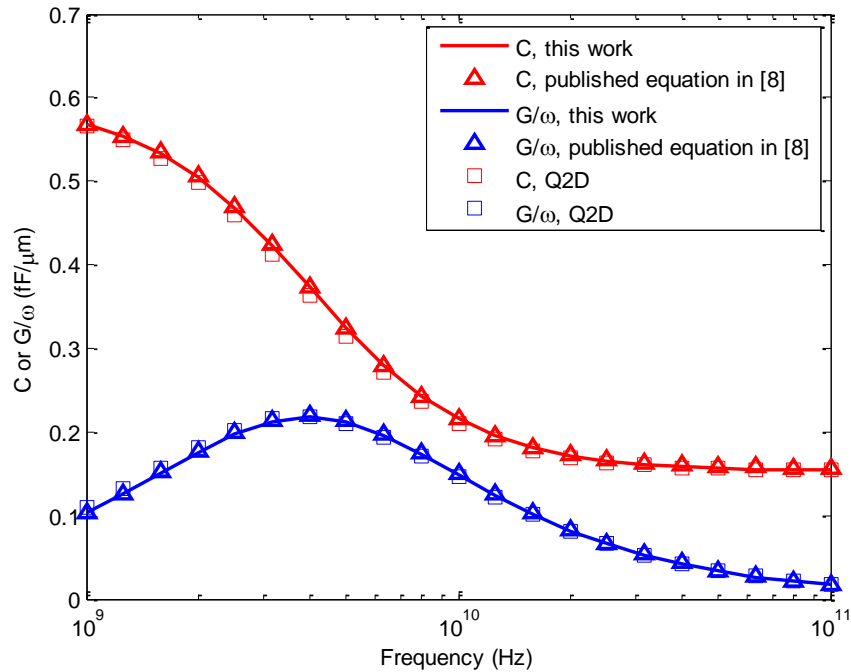


Figure 3.4. Admittance Results for a Typical TSV Pair: $d = 15\mu\text{m}$;
 $r_{\text{TSV}} = 2.5\mu\text{m}$; $t_{\text{ox}} = 0.5\mu\text{m}$; $\rho_{\text{Si}} = 10\Omega\text{-cm}$

In the second case where the pitch size was reduced to $d = 7\mu\text{m}$, the calculated results using the proposed approach in this paper still agree well with the results from the 2D finite-element-method tool, as demonstrated in Figure 3.5. However, the calculated values using the published equations in [56] show obvious deviations. This is because the proximity effect between the two TSVs cannot be neglected in this case anymore when the pitch size is small. The published equations in [56] are not suitable to deal with tightly coupled TSVs.

The proposed method converges rapidly. In the extreme case of $d = 7\mu\text{m}$, good convergence has reached by including only the 1st-order harmonic expansion functions ($k = 3$) as shown in Figure 3.6. Thus, the proposed approach is very effective and efficient in computing the admittance matrix for a large amount of TSVs.

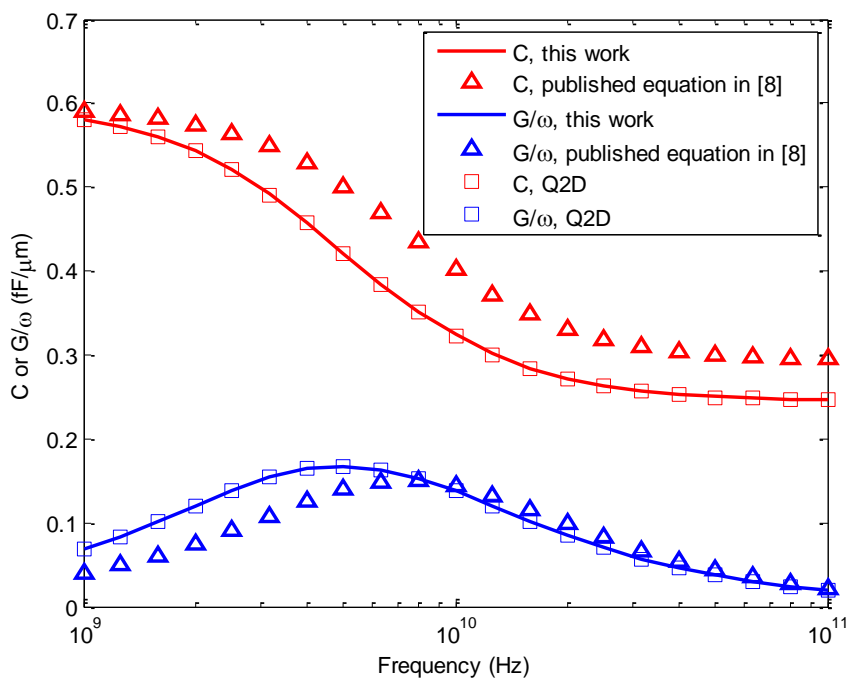


Figure 3.5. Admittance Results for a Typical TSV Pair: $d = 7\mu\text{m}$;
 $r_{\text{TSV}} = 2.5\mu\text{m}$; $t_{\text{ox}} = 0.5\mu\text{m}$; $\rho_{\text{Si}} = 10\Omega\text{-cm}$

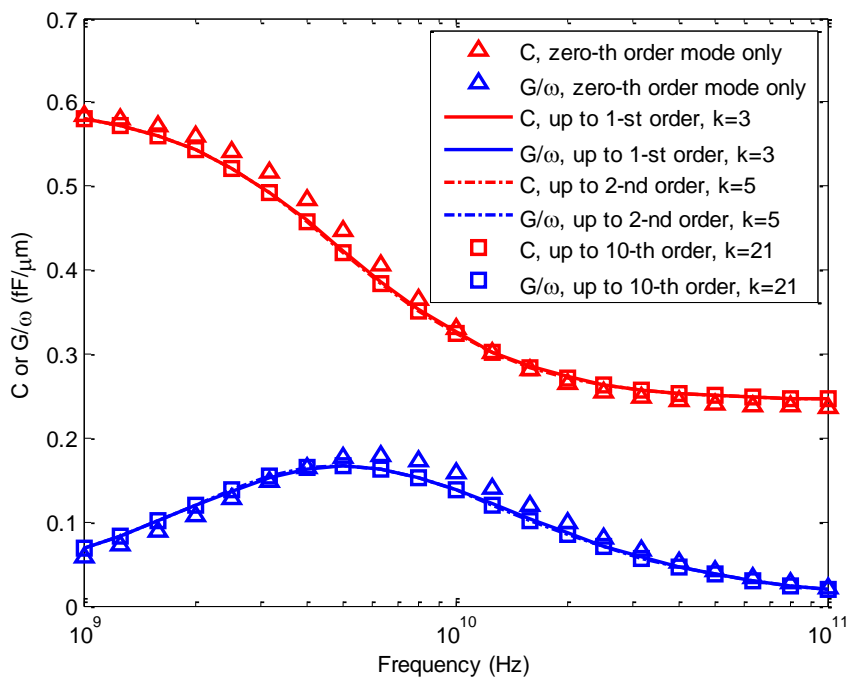


Figure 3.6. Convergence of the Proposed Approach: $d = 7\mu\text{m}$; $r_{\text{TSV}} = 2.5\mu\text{m}$;
 $t_{\text{ox}} = 0.5\mu\text{m}$; $\rho_{\text{Si}} = 10\Omega\text{-cm}$.

3.5. A TSV ARRAY

A 5-by-5 TSV array structure is shown in Figure 3.7. These TSVs are closely coupled, with following parameters: pitch = $7\mu\text{m}$; $r_{\text{TSV}} = 2.5\mu\text{m}$; $t_{\text{ox}} = 0.5\mu\text{m}$; $\rho_{\text{Si}} = 10\Omega\text{-cm}$. TSV #1 is set as reference ground in a commercial 2D cross-section analysis tool (Q2D[80]).

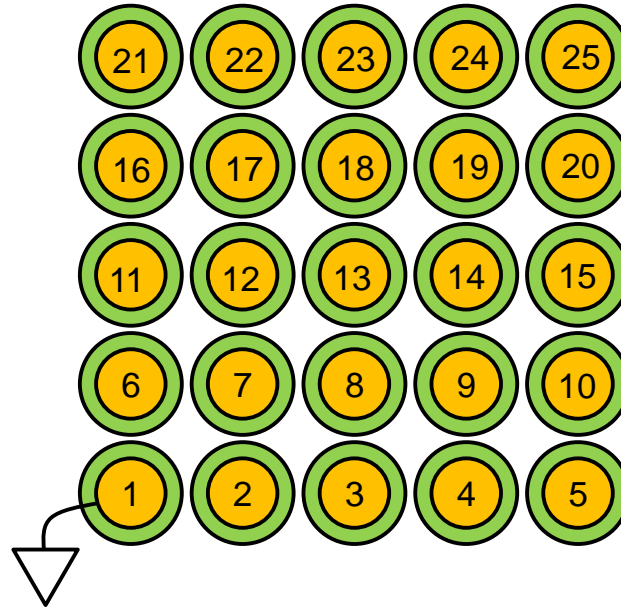


Figure 3.7. A 5-by-5 TSV Array

The capacitance matrix obtained by the proposed method is the so-called “Short Circuit Capacitances” in [81] or “Generalized Capacitance Matrix” in [82], which is the inverse of P , “Coefficients of Potential”. The capacitance matrix obtained in Q2D is equivalent to the “Per-unit-length Transmission-Line Capacitance Matrix” in [82], when one of the $N+1$ conductors is grounded. Or its absolute value can be obtained by the “Node Pair Capacitances” in [81].

After proper conversion, the admittance comparison between node-pair 2&7 is shown in Figure 3.8. Due to the close coupling, only 0^{th} order basis is not enough to properly capture the charge distribution, and therefore inaccurate admittance value is obtained. From the convergence study in Figure 3.9, even only one higher order mode is enough to get a good agreement with Q2D.

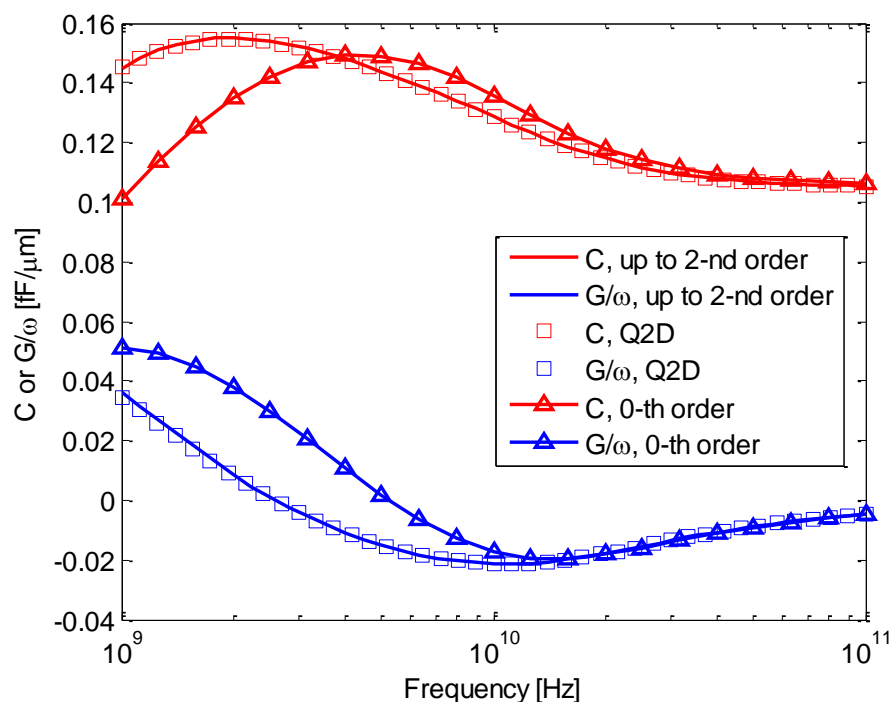


Figure 3.8. Node Pair C_{27} and G_{27}/ω for the 25-via TSV Array: pitch = $7\mu\text{m}$;

$$r_{\text{TSV}} = 2.5\mu\text{m}; t_{\text{ox}} = 0.5\mu\text{m}; \rho_{\text{Si}} = 10\Omega\text{-cm}$$

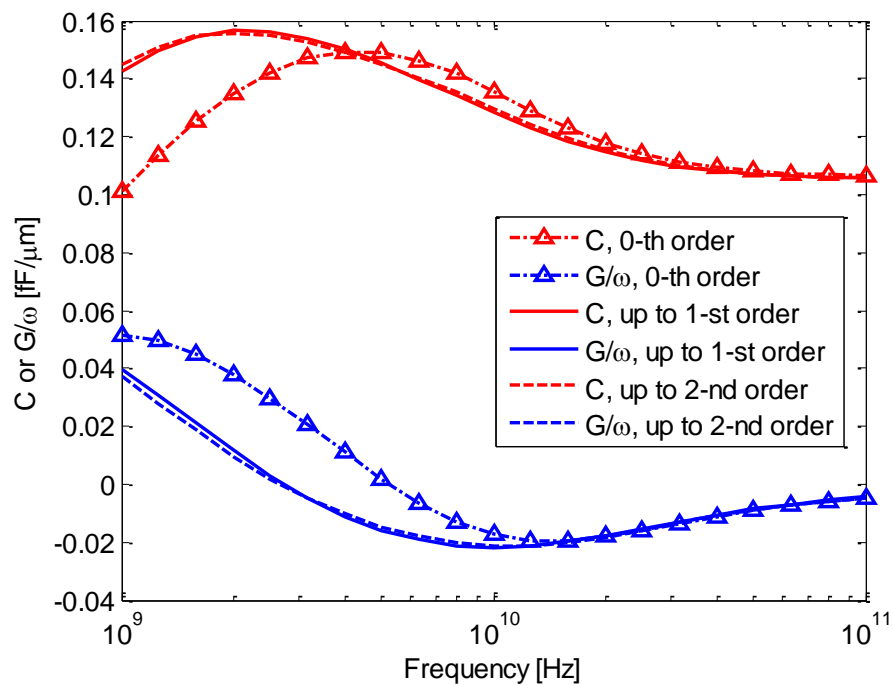


Figure 3.9. Convergence Study for Node Pair C_{27} and G_{27}/ω

The time consumption is compared between Q2D and proposed method in Table 3.2. Due to the tiny geometry, the finite element mesh in Q2D has to be very fine to achieve a convergence. The proposed method shows great advantage since no geometric mesh is required. The comparison was performed on a PC with Windows 7 OS, 4.00 GB RAM, 2.66GHz 2-Core CPU. The proposed method is programmed in MATLAB, with variable of frequency vectorized. And therefore, the number of frequency samples doesn't play a significant role in the time consumption.

Table 3.2. Time Consumption of Proposed Method

| TSV# | 0 th order | Up to 1 st order | Up to 2 nd order | Q3D |
|------|-----------------------|-----------------------------|-----------------------------|----------|
| 9 | 0.5 sec | 4 sec | 11 sec | 35 min |
| 25 | 4 sec | 33 sec | 90 sec | > 2.5 hr |

3.6. CONCLUSION

An accurate approach to calculate the quasi-static admittance matrix for TSV arrays is developed in this paper. It uses the concept of bound charge to change the original problem with inhomogeneous media into an equivalent but simpler problem with a homogeneous medium. Using the axial harmonic basis functions further reduces the number of unknowns significantly. Galerkin's method is used to enforce the reciprocity in the numerical formulation. The approach is validated with published work as well as full-wave simulations. It is demonstrated that the proposed method can deal with the cases with small pitch sizes where the proximity effect may have to be considered, while the added computational cost is minimal. Only a few higher-order modes are needed to achieve convergence.

BIBLIOGRAPHY

- [1] S. Caniggia, F. Maradei, "Circuit and numerical modeling of electrostatic discharge generators," *Industry Applications, IEEE Transactions on*, vol. 42, Issue 6, Nov.-Dec. 2006. pp:1350 -1357.
- [2] G. Cerri, R. De Leo, and V. M. Primiani, "ESD indirect coupling modeling," *IEEE Trans. Electromagn. Compat.*, vol. 38, no. 3, pp. 274–281, Aug. 1996.
- [3] IEC 61000-4-2 Ed. 2.0, Electromagnetic compatibility (EMC) - Part 4-2: Testing and measurement techniques - Electrostatic discharge immunity test 2008-12-09.
- [4] J. Koo, Q. Cai, G. Muchaidze, A. Martwick, K. Wang, and D. Pommerenke, "Frequency-domain measurement method for the analysis of esd generators and coupling," *IEEE Trans, Electromagn. Compat.*, vol. 49, no. 3, pp.504-511, Aug. 2007.
- [5] H. Tanaka, O. Fujiwara, and Y. Yamanaka, "A circuit approach to simulate discharge current injected in contact with an ESD-gun," in *Proc. 3rd Int. Symp. Electromagn. Compat.* May 21–24, 2002, pp. 486–489.
- [6] K. Wang, D. Pommerenke, R. Chundru, T. V. Doren, J. L. Drewniak, and A. Shashindranath, "Numerical modeling of electrostatic discharge generators," *IEEE Trans. Electromagn. Compat.*, vol. 45, no. 2, pp. 258–271, May 2003.
- [7] F. Centola, D. Pommerenke, K. Wang, T. V. Doren, and S. Caniggia, "ESD excitation model for susceptibility study," in *Proc. IEEE Int. Symp. Electromagn. Compat.* Aug. 18–22, 2003, vol. 1, pp. 58–63.
- [8] R. Jobava, D. Pommerenke, D. Karkashadze, P. Shubitidze, R. Zaridze, S. Frei, and M. Aidam, "Computer Simulation of ESD from Voluminous Objects Compared to Transient Fields of Humans," *IEEE Trans. Electromagn. Compat.*, vol. 42, no. 1, pp. 54–65, February 2000.
- [9] Y. Taka, O. Fujiwara, "Verification of spark resistance formula for human ESD," 2008 Asia-Pacific Symposium on Electromagnetic Compatibility & 19th International Zurich Symposium on Electromagnetic Compatibility, pp. 152-155, May 2008.
- [10] R. Jobava, D. Pommerenke, D. Karkashadze, P. Shubitidze, R. Zaridze, S. Frei, R. Beria, and A. Gheonjian, "Computer simulation of ESD from cone," *DIPED-98. Proceedings of III International Seminar/Workshop on*, pp. 111-113, 1998.

- [11] R. Zaridze, D. Karkashadze, R. G. Djobava, D. Pommerenke, and M. Aidam, "Numerical calculation and measurement of transient fields from electrostatic discharges," *IEEE Trans. Components, packaging, and manufacturing technology*. Part C, vol. 19, no. 3, pp. 178-183, July 1996.
- [12] D. Pommerenke, M. Aidam, "To what extent do contact-mode and indirect ESD test methods reproduce reality," *Electrical Overstress/Electrostatic Discharge Symposium Proceedings*, 1995. 12-14 Sept. 1995, pp. 101-109.
- [13] D. Pommerenke, "ESD: transient field, arc simulation and rise time limit," *Journal of electrostatics*, ISSN 0304-3886, vol. 36, no. 1, pp. 31-54, 1995
- [14] O. Fujiwara, H. Seko, "FDTD computation modeling based on spark-resistance formula for electromagnetic fields due to electrostatic discharge", *Proc. International Wroclaw Symposium and Exhibition on Electromagnetic Compatibility*, pp.421-424, 2002.
- [15] N. Orhanovic, R. Raghuram, N. Matsui, "Full wave Analysis of planar interconnect structures using FDTD-SPICE," *Electronic Components and Technology Conference, 2001. Proceedings., 51st*, pp. 489-494, 2001.
- [16] N. Orhanovic, R. Raghuram, N. Matsui, "Nonlinear full wave time domain solutions using FDTD_SPICE for high speed digital and RF," *Wireless and Optical Broadband Conference, 2001*.
- [17] Microwave Studio, Computer Simulation Technology, [Online]. Available: <http://www.cst.com/>
- [18] Meek and Craggs, "Electrical Break down of Gases," Oxford Univ. Press, Oxford, 1953 and Wiley, New York, 1978.
- [19] G. A. Mesyats, V. V. Kremnev, G. S. Korshunov and Yu. B. Yankelevich, "Spark current and voltage in nanosecond breakdown of a gas gap, *Sov. Phys. Tech. Phys.*, 14(1) (1969) 49-53.
- [20] M. Bandinu, F. Canavero, S. Grivet-Talocia, I. S. Stievano, "IdEM & M π LOG: macromodeling tools for system-level signal integrity and EMC assessment", European IBIS Summit Meeting, Apr. 19, 2007.
- [21] Broadband SPICE, Sigrity, [Online]. Available: <http://www.sigrity.com/products/bds/bds.htm>

- [22] D. L. Lin and T. L. Welsher, "From lightning to charged-device model electrostatic discharges," *ESO/ESD Symp.* (1992) 68-75.
- [23] S. Atsushi, Y. Takahiro, M. Noriaki, "Effects of the relative humidity on ESD from the charged metal," *Seidenki Gakkai Koen Ronbunshu*, vol.2006, no., pp.43-44, 2006.
- [24] Q. Cai, J. Koo, A. Nandy, D. Pommerenke, Jong Sung Lee, Byong Su Seol, "Advanced full wave ESD generator model for system level coupling simulation", *Electromagnetic Compatibility, 2008. EMC 2008. IEEE International Symposium on*, 18-22 Aug. 2008, pp. 1-6.
- [25] EMCoS: EMC Studio, Version 7.0. [Online]. Available: <http://www.emcos.com>
- [26] FEKO, EM Software & Systems
- [27] C. S. Technology, "CST CABLE STUDIO," in *CST STUDIO SUITE* vol. 2011, www.cst.com, Ed., ed, 2011.
- [28] Taylor, C.; Satterwhite, R.; Harrison, C., Jr., "The response of a terminated two-wire transmission line excited by a nonuniform electromagnetic field," *Antennas and Propagation, IEEE Transactions on* , vol.13, no.6, pp.987,989, Nov 1965
- [29] Paul, Clayton R. *Analysis of multiconductor transmission lines*. Wiley-IEEE Press, 2007.
- [30] Paul, Clayton R. "A SPICE model for multiconductor transmission lines excited by an incident electromagnetic field." *Electromagnetic Compatibility, IEEE Transactions on* 36.4 (1994): 342-354.
- [31] Agrawal, A.K.; Price, H.J.; Gurbaxani, S.H.; , "Transient Response of Multiconductor Transmission Lines Excited by a Nonuniform Electromagnetic Field," *Electromagnetic Compatibility, IEEE Transactions on* , vol.EMC-22, no.2, pp.119-129, May 1980
- [32] F. Rachidi, "Formulation of the field-to-transmission line coupling equations in terms of magnetic excitation fields," *IEEE Trans. Electromagn.Compat.*, vol. 35, no. 3, pp. 404-407, Aug. 1993.

- [33] Rachidi, F., "A Review of Field-to-Transmission Line Coupling Models With Special Emphasis to Lightning-Induced Voltages on Overhead Lines," *Electromagnetic Compatibility, IEEE Transactions on* , vol.54, no.4, pp.898,911, Aug. 2012
- [34] F. M. Tesche, M. Ianoz, and T. Karlsson, *EMC Analysis Methods and Computational Models*. New York: Wiley-Interscience, 1997.
- [35] Bruns, H.-D.; Singer, H.; , "Computation of interference in cables close to metal surfaces," *Electromagnetic Compatibility, 1998. 1998 IEEE International Symposium on* , vol.2, no., pp.981-986 vol.2, 24-28 Aug 1998
- [36] Paletta, L.; Parmantier, J.-P.; Issac, F.; Dumas, P.; Alliot, J.-C.; , "Susceptibility analysis of wiring in a complex system combining a 3-D solver and a transmission-line network simulation," *Electromagnetic Compatibility, IEEE Transactions on* , vol.44, no.2, pp.309-317, May 2002
- [37] X. Ferrieres, J.-P. Paramantier, S. Bertuol, and A. R. Ruddle, "Application of a hybrid finite difference/finite volume method to solve an automotive EMC problem," *IEEE Trans. Electromagn. Compat.*, vol. 46, no. 4, pp. 624–634, Nov. 2004.
- [38] Topchishvili, D.; Jobava, R.; Bogdanov, F.; Chikhradze, B.; Frei, S.; , "A hybrid MTL/MoM approach for investigation of radiation problems in EMC," *Direct and Inverse Problems of Electromagnetic and Acoustic Wave Theory, 2004. DIPED 2004. Proceedings of the 9th International Seminar/Workshop on* , vol., no., pp. 65- 68, 11-14 Oct. 2004
- [39] Chobanyan, H.; Badzagua, I.; Injgia, T.; Gheonjian, A.; Jobava, R.; , "Application of hybrid MOM/MTL method to simulation of interaction between cable harness and antennas," *Direct and Inverse Problems of Electromagnetic and Acoustic Wave Theory, 2009. DIPED 2009. International Seminar/Workshop on* , vol., no., pp.33-38, 21-24 Sept. 2009
- [40] Badzagua, I.; Chobanyan, H.; Chikovani, G.; Oganezova, I.; Yavolovskaya, E.; Injgia, T.; Gheonjian, A.; Jobava, R., "Effective computational techniques for EMC analysis of cable harness," *Direct and Inverse Problems of Electromagnetic and Acoustic Wave Theory (DIPED), 2010 Xvth International Seminar/Workshop on* , vol., no., pp.96,102, 27-30 Sept. 2010
- [41] Frei, S., and R. Jobava. "Coupling of inhomogeneous fields into an automotive cable harness with arbitrary terminations." *Proc. of EMC Zurich*. Vol. 1. 2001.

- [42] C. E. Baum, T. K. Liu, and F. M. Tesche, "On the analysis of general multiconductor transmission line networks," *Interaction Notes*, vol. 350, pp. 467–547, 1978
- [43] Sabath, F.; Garbe, H., "Radiation analysis of PCB layout using a hybrid MoM-MTL method," *Electromagnetic Compatibility, IEEE Transactions on* , vol.45, no.2, pp.424,435, May 2003
- [44] Nitsch, J.B.; Tkachenko, S.V., "Complex-valued transmission-line parameters and their relation to the radiation resistance," *Electromagnetic Compatibility, IEEE Transactions on* , vol.46, no.3, pp.477,487, Aug. 2004
- [45] Maffucci, A.; Miano, G.; Villone, F., "An enhanced transmission line model for conducting wires," *Electromagnetic Compatibility, IEEE Transactions on* , vol.46, no.4, pp.512,528, Nov. 2004
- [46] Maffucci, A.; Miano, G.; Villone, F., "An enhanced transmission line model for conductors with arbitrary cross sections," *Advanced Packaging, IEEE Transactions on* , vol.28, no.2, pp.174,188, May 2005
- [47] Chiariello, A.G.; Maffucci, A.; Miano, G.; Villone, F.; Zamboni, W., "A Transmission-Line Model for Full-Wave Analysis of Mixed-Mode Propagation," *Advanced Packaging, IEEE Transactions on* , vol.31, no.2, pp.275,284, May 2008
- [48] Nitsch, Jürgen, and Sergey Tkachenko. "High-frequency multiconductor transmission-line theory." *Foundations of Physics* 40.9-10 (2010): 1231-1252.
- [49] Toki, Hiroshi, and Kenji Sato. "Electrodynamics of Multiconductor Transmission-line Theory with Antenna Mode."
- [50] Tkatchenko, S.; Rachidi, F.; Ianoz, M.; , "Electromagnetic field coupling to a line of finite length: theory and fast iterative solutions in frequency and time domains," *Electromagnetic Compatibility, IEEE Transactions on* , vol.37, no.4, pp.509-518, Nov 1995
- [51] Bayram, Y.; Volakis, J.L.; , "A generalized MoM-SPICE iterative technique for field coupling to multiconductor transmission lines in presence of complex structures," *Electromagnetic Compatibility, IEEE Transactions on* , vol.47, no.2, pp. 234- 246, May 2005

- [52] Bayram, Y.; Volakis, J.L.; , "A hybrid MoM-SPICE technique for field coupling analysis of transmission lines in presence of complex structures," *Electromagnetic Compatibility*, 2005. EMC 2005. 2005 International Symposium on , vol.2, no., pp.590-595, 12-12 Aug. 2005
- [53] Shinh, Gurpreet S., et al. "Fast transient analysis of incident field coupling to multiconductor transmission lines." *Electromagnetic Compatibility, IEEE Transactions on* 48.1 (2006): 57-73.
- [54] Sun, S., Liu, G., Pommerenke, D. J., Drewniak, J. L., Kautz, R. W., & Chen, C. (2004, August). Anticipating EMI and on-board interference in automotive platforms. In *Electromagnetic Compatibility, 2004. EMC 2004. 2004 International Symposium on* (Vol. 3, pp. 792-797). IEEE.
- [55] Vukicevic, A.; Rachidi, F.; Rubinstein, M.; Tkachenko, S.V., "On the Evaluation of Antenna-Mode Currents Along Transmission Lines," *Electromagnetic Compatibility, IEEE Transactions on* , vol.48, no.4, pp.693,700, Nov. 2006
- [56] Chuan Xu; Hong Li; Suaya, R.; Banerjee, K.; , "Compact AC modeling and analysis of Cu, W, and CNT based through-silicon vias (TSVs) in 3-D ICs," *Electron Devices Meeting (IEDM), 2009 IEEE International* , vol., no., pp.1-4, 7-9 Dec. 2009
- [57] Ramm, P.; Wolf, M.J.; Klumpp, A.; Wieland, R.; Wunderle, B.; Michel, B.; Reichl, H.; , "Through silicon via technology — processes and reliability for wafer-level 3D system integration," *Electronic Components and Technology Conference, 2008. ECTC 2008. 58th* , vol., no., pp.841-846, 27-30 May 2008
- [58] Zheng Xu; Beece, A.; Rose, K.; Tong Zhang; Jian-Qiang Lu; , "Modeling and evaluation for electrical characteristics of through-strata-vias (TSVs) in three-dimensional integration," *3D System Integration, 2009. 3DIC 2009. IEEE International Conference on* , vol., no., pp.1-9, 28-30 Sept. 2009
- [59] Weerasekera, R.; Grange, M.; Pamunuwa, D.; Tenhunen, H.; Li-Rong Zheng; , "Compact modelling of Through-Silicon Vias (TSVs) in three-dimensional (3-D) integrated circuits," *3D System Integration, 2009. 3DIC 2009. IEEE International Conference on* , vol., no., pp.1-8, 28-30 Sept. 2009
- [60] Bandyopadhyay, T.; Chatterjee, R.; Daehyun Chung; Swaminathan, M.; Tummala, R.; "Electrical modeling of Through Silicon and Package Vias," *3D System Integration, 2009. 3DIC 2009. IEEE International Conference on* , vol., no., pp.1-8, 28-30 Sept. 2009

- [61] Kannan, S.; Evana, S.S.; Gupta, A.; Kim, B.; Li Li; , "3-D Copper based TSV for 60-GHz applications," Electronic Components and Technology Conference (ECTC), 2011 IEEE 61st , vol., no., pp.1168-1175, May 31 2011-June 3 2011
- [62] Katti, G.; Stucchi, M.; De Meyer, K.; Dehaene, W.; , "Electrical Modeling and Characterization of Through Silicon via for Three-Dimensional ICs," Electron Devices, IEEE Transactions on , vol.57, no.1, pp.256-262, Jan. 2010
- [63] Chuan Xu; Hong Li; Suaya, R.; Banerjee, K.; , "Compact AC Modeling and Performance Analysis of Through-Silicon Vias in 3-D ICs," Electron Devices, IEEE Transactions on , vol.57, no.12, pp.3405-3417, Dec. 2010
- [64] D. Liu, S. Pan, B. Achkir, J. Fan, "Fast Admittance Computation for TSV Arrays", Electromagnetic Compatibility (EMC), 2011 IEEE International Symposium on.
- [65] Clements, J.C.; Paul, C.R.; Adams, A.T.; , "Computation of the Capacitance Matrix for Systems of Dielectric-Coated Cylindrical Conductors," Electromagnetic Compatibility, IEEE Transactions on , vol.EMC-17, no.4, pp.238-248, Nov. 1975
- [66] Ki Jin Han; Swaminathan, M.; Ege Engin; , "Electric field integral equation combined with cylindrical conduction mode basis functions for electrical modeling of three-dimensional interconnects," Design Automation Conference, 2008. DAC 2008. 45th ACM/IEEE , vol., no., pp.421-424, 8-13 June 2008
- [67] Ki Jin Han; Swaminathan, M.; , "Inductance and Resistance Calculations in Three-Dimensional Packaging Using Cylindrical Conduction-Mode Basis Functions," Computer-Aided Design of Integrated Circuits and Systems, IEEE Transactions on , vol.28, no.6, pp.846-859, June 2009
- [68] Ki Jin Han; Swaminathan, M.; , "Polarization mode basis functions for modeling insulator-coated through-silicon via (TSV) interconnections," Signal Propagation on Interconnects, 2009. SPI '09. IEEE Workshop on , vol., no., pp.1-4, 12-15 May 2009
- [69] Ki Jin Han; Swaminathan, M.; Bandyopadhyay, T.; , "Electromagnetic Modeling of Through-Silicon Via (TSV) Interconnections Using Cylindrical Modal Basis Functions," Advanced Packaging, IEEE Transactions on , vol.33, no.4, pp.804-817, Nov. 2010

- [70] Bandyopadhyay, T.; Ki Jin Han; Daehyun Chung; Chatterjee, R.; Swaminathan, M.; Tummala, R.; , "Rigorous Electrical Modeling of Through Silicon Vias (TSVs) With MOS Capacitance Effects," *Components, Packaging and Manufacturing Technology, IEEE Transactions on* , vol.1, no.6, pp.893-903, June 2011
- [71] A. E. Ruehli, "Equivalent Circuit Models for Three-Dimensional Multiconductor Systems," *IEEE Trans. Microwave Theory and Techniques*, vol. 22, no. 3, pp. 216-221, Mar. 1974.
- [72] Jun Fan; Hao Shi; Orlandi, A.; Knighten, J.L.; Drewniak, J.L.; , "Modeling DC power-bus structures with vertical discontinuities using a circuit extraction approach based on a mixed-potential integral equation," *Advanced Packaging, IEEE Transactions on* , vol.24, no.2, pp.143-157, May 2001
- [73] Gibson, Walton C. *The method of moments in electromagnetics*. Chapman & Hall/CRC, 2007.
- [74] W. Wang, "The exact kernel for cylindrical antenna," *IEEE Trans. Antennas Propagat.*, vol. 39, 434–435, April 1991.
- [75] P. Silvester, "Modal Network Theory of Skin Effect in Flat Conductors," *Proc. IEEE* , vol. 54, no. 9, pp. 1147-1151, Sep. 1966.
- [76] D. K. Cheng, "*Field and Wave Electromagnetics*", Addison-Wesley, 1989.
- [77] Tsang, Leung, Jin Au Kong, and Kung-Hau Ding. *Scattering of Electromagnetic Waves, Theories and Applications*. Vol. 27. Wiley-Interscience, 2004.
- [78] *Equation 5.54*, IS Gradshteyn and IM Ryzhik, "*Table Of Integrals, Series And Products*", Academic Press, Elsevier Inc. 7ed., 2007.
- [79] A. T. Adams, *Electromagnetics for Engineers*, Ronald Press Co., N. Y., 1972, Chapters 8, 9.
- [80] ANSYS Q3D Extractor. [Online]. Available: http://www.ansoft.com/products/si/q3d_extractor/
- [81] Ruehli, Albert E.; Brennan, Pierce A., "Capacitance models for integrated circuit metallization wires," *Solid-State Circuits, IEEE Journal of* , vol.10, no.6, pp.530,536, Dec 1975

- [82] Paul, Clayton R.; Feather, A.E., "Computation of the Transmission Line Inductance and Capacitance Matrices from the Generalized Capacitance Matrix," *Electromagnetic Compatibility, IEEE Transactions on* , vol.EMC-18, no.4, pp.175,183, Nov. 1976

VITA

Dazhao Liu was born in 1986, in Qingyang City, Gansu Province, P.R. China. In May 2008, he received his Bachelor's Degree of Science, Electrical Engineering in Electrical Engineering Department of Tsinghua University, Beijing, P. R. China.

In August 2008, he enrolled at the Missouri University of Science and Technology to pursue his Master's Degree in Electrical Engineering, since when, he was a graduate research assistant in Electromagnetic Compatibility Laboratory.

After finishing his Master's Degree in October 2010, he continued Ph.D. Electrical Engineering in the same lab, and received his Ph.D. degree in December 2013.

